THREE HINGE BUCKLING LABORATORY EXPERIMENT AND MODELLING SIMULATION

by

Mehdi Ghasemi Ghodrat

Submitted in partial fulfillment of the requirements
for the degree of Doctor of Philosophy

at

Dalhousie University
Halifax, Nova Scotia
November 2020

This thesis is dedicated to my best friend, my love, and my wife

ASAL,

for her unconditional love and support

and to my parents,

MANSOUREH and ALI,

who had given me dreams to look forward to

and my brother,

ALIREZA,

for his encouragement.

Table of Contents

iii

List of Tables

List of Figures

Abstract

Near-surface buckling failure typically occurs in horizontally bedded sedimentary rocks in the presence of high horizontal in situ stresses and it is a concern for quarries and open-pit mining operations. Usually, sudden energy release, similar to rock bursting, is the consequence of this failure. Buckling failure causes many economic and environmental problems. Even though some research has been carried out on the topic, many limitations still exist to develop a suitable buckling stability analysis procedure. The most important limitation is the lack of a specific, accurate and cost-effective method to analyze this mechanism; therefore, presenting a quantitative way to assess buckling stability is necessary. This research's primary objective was to identify the limitations and develop a proper buckling stability analysis procedure. Therefore, an extensive literature review was carried out, and a comprehensive buckling database, including all available geological, geometrical, and mechanical parameters, was collected. This phase also was included a statistical analysis of the collected buckling data to complete the first phase in understanding the problem more quantifiably. In the second phase, experimental studies were conducted that included a methodology and the invention of a novel apparatus that can reproduce a simple three hinge buckling (THB) at the laboratory scale. In the third phase, several THB experiments were conducted using the newly introduced THB test. Digital image correlation (DIC) methods and acoustic emission (AE) technology were utilized along with conventional recording methods to monitor the new THB experiment. These tests' experimental results provided quantifiable data and demonstrated that THB failure depends on the thickness/length ratio and axial confinement. Finally, in the fourth phase, a numerical model, based on the two-dimensional discrete element method (DEM), was used to simulate the THB experiment. The recently developed *UDEC* Voronoi tessellation micromechanical modelling technique was used to reproduce and validate the experimental data. The results represented a good agreement between the experimental and numerical results. Overall, this study improved the understanding of buckling failure behaviour by developing appropriate applicable experimental tests and numerical modelling. This technique can lead to reproducing more complex field-scale models to conduct comprehensive buckling stability analysis in future.

Keywords: Buckling, THB experimental test, digital image correlation, pop ups, acoustic emission, *UDEC*.

List of Abbreviations and Symbols Used

BSLB   Blocky single layer buckling

EUB   Euler buckling

EXB   Exfoliation buckling

MRB   Massive rock buckling

MLB   Multi-layer buckling

SLB   Single layer buckling

THB   Three hinge buckling

MIRARCO2005   In situ stress database, Ontario

WSM2016   World Stress Map database, 2016 version

AE   Acoustic emission

DAQ   Data acquisition system

DCV   Directional control valve

DIC   Digital image correlation

LP   Linear potentiometer

LVDT   Linear variable differential transducer

UCS   Unconfined Compressive Strength (test name)

THC   Trigger-Hit-Count

PAS   Pulser Amplifier System

MS   microseismic

PAD   Pulser Amplifier Desktop

PIU   Pulser Interface Unit

σ_c Unconfined compressive strength (peak stress)

σ_{ci} Crack initiation threshold

s_v Vertical in situ stress

s_H Horizontal in situ stress, maximum

s_h Horizontal in situ stress, minimum

s_{cr} Critical s_H at onset of potential buckling (Roorda method)

E Young's modulus

k In situ stress ratio (Horizontal to vertical)

ρ Density

g Gravitational acceleration constant

z Depth below ground surface

T_b Thickness of buckling layer(s)

L_b Length of buckling layer(s)

W_b Width of buckling layer(s)

H_b Height of buckling layer(s)

α_b Orientation (azimuth) of buckling direction

β_H Orientation (azimuth) of maximum horizontal stress

β_b Dominant orientation (azimuth) of maximum horizontal stress

P_{cr} Critical load in flexural buckling

K_e	End condition constant
I	Moment of inertia
b	Slope width
d	Slab thickness
l_b	Buckled slope length
l	Total slope length
c_j	Interface (joint) cohesion
δ_a	Axial displacement of upper load platen
δ_l	Lateral displacement measured from the reference tab
δ_{ly}	Lateral displacement at yield measured from the reference tab
δ_{lp}	Lateral displacement at peak measured from the reference tab
δ_{lr}	Lateral displacement at rupture measured from the reference tab
δ_{la}	Apex lateral displacement measured using DIC method
ϕ_j	Interface (joint) friction angle
K_n	Interface normal stiffness
K_s	Interface shear stiffness
L	Length (vertical) of test block specimen
ν	Poisson's ratio
P_a	Axial load on THB block specimens
P_l	Lateral load on THB block specimens
P_{lp}	Peak lateral load

P_{lr}	Lateral load at rupture
$\bar{\sigma}_H$	Maximum horizontal in situ stress
σ_a	Axial stress on block specimens ('clamping stress') and the UCS test
σ_t	Tensile strength
σ_y	Stress component in y direction
σ_c	Peak stress from the UCS test
σ_{ci}	Crack initiation stress from the UCS test
t_j	Interface (joint) tensile strength
T	Thickness of test block specimen in buckling direction
W	Width of test block specimen perpendicular to buckling
γ	Thickness of the blocks' interface that is not in contact at failure
Δ_{lp}	Apex displacement at the peak
Φ_m	Resistance factor of the specimen
C	Compression force per unit length at crushing zones

Acknowledgements

First and foremost, I would like to express my sincere gratitude to my supervisor, Dr. Andrew Corkum, for his vision, enthusiasm, motivation, and intellectual and scientific support, and for providing me with the opportunity to carry out this unique research. He greatly supported and encouraged me through all the challenging steps and helped me to expand and hone my abilities. My discussions with Dr. Corkum deeply broadened my vision towards my research goals and provided me with numerous innovative ideas to explore. I appreciate all his contributions of time, ideas and energy to make my PhD experience productive and stimulating.

I would like to acknowledge my committee members, Dr. Yi Liu, and Dr. Dmitry Garagash, and my external examiner Dr. Davide Elmo for their contribution of reviewing my PhD thesis and providing technical feedback.

Additionally, I would like to thank the civil engineering department laboratory technicians Mr. Brian Kennedy, Mr. Jordan Maerz, and Mr. Jesse Keane for their assistance with my project, as well as department staff, Mrs. June Ferguson and Mrs. Shelley Parker for their help throughout my studies.

I would like to thank my fellow colleagues, Brock Jeans, Ryan Ziebarth and Farzaneh Hamediazad for their helpful collaboration in completing the experiments.

I wish to express my sincere thanks to my parents Mansoureh and Ali, and my brother Alireza for their moral support, their love, and inspiration they have given me to pursue my PhD degree. Also, I am very thankful to my mother and brother in-laws Farah and Arash for being such a caring and loving family, and all my amazing friends who made this journey unforgettable.

Finally, I am in debated to my kind-hearted wife, Asal, who has been always the best friend to me. Her patience, endless sacrifices and love helped me with overcoming all the obstacles throughout my work.

Chapter 1

Introduction

1.1   General

Near-surface buckling failure typically occurs in horizontally bedded sedimentary rocks in quarry floors and natural sites with the presence of high horizontal in situ stresses. In North America, numerous buckling failure have been observed in Ontario, Quebec and New York state, along with a few cases in Manitoba, New Brunswick, and Kentucky. Due to the presence of high horizontal stresses, this failure mechanism occurs rapidly, with little warning. Sometimes buckling failure is referred to as a 'pop up' because of a sudden energy release similar to rock bursting. It is also believed that initiation of the buckling failure is caused by some type of 'trigger' mechanisms, such as blast vibrations or water pressure. There are examples of buckling failure reported in North America by Saull and Williams (1974); Lo (1978); Adams (1982); White and Russell (1982); Williams et al. (1985); Crossley (1991); Karrow (1993); Wallach et al. (1993, 1994); Thomas et al. (1993); Wallach and Chagnon (1990), and Everitt (2009). Despite all buckling cases reported, buckling failure mechanisms were not the focus of authors' studies, and there are many neglects in collecting all field data. Hence, having a database including all buckling cases with the geological, geometrical, and

mechanical information of buckling failures may lead to a better understanding and development of a suitable analysis method.

Recently, instability due to buckling failure has turned into a concern for quarries and the surface mining industry. For instance, if the 'rock buffer' that prevents hydraulic connectivity is not thick enough, it may begin flooding; thus, impacting nearby wells and causing many damages in quarries due to buckling failure. An example of this event occurred in the Ottawa region of Ontario (Crossley, 1991), and the environmental bureau in Ontario, Canada, showed considerable interest in understanding this buckling instabilies. Many researchers have been studied on buckling instability analysis, such as Adams (1982); Roorda et al. (1982); White and Russell (1982); Roorda (1995) in quarries, Sofianos (1996); Diederichs and Kaiser (1999); Boon (2019); Hu and Cruden (1993) in underground excavations, Cavers (1981); Martin et al. (1997); Tommasi et al. (2009) for slopes, and McDowell et al. (1956) and Dawe and Seah (1989) for masonry structures. Despite these past studies, there is no well-developed analysis methodology to predict buckling failure mechanisms in quarry floors.

Buckling failure may occur in different modes and mode combinations, such as exfoliation and brittle fracture, rock softening, or occur in multiple rock layers. Due to the fact that buckling failure is infrequent to observe and occurs rapidly without any warning, a simple laboratory experiment with the aid of analytical or numerical method may explain all of these complex modes and provide an insight to develop

a suitable stability analysis method. In recent years, with the increase in computational power, numerical modelling has become more commonly-used in solving rock engineering problems. In such cases, commercial codes like *PFC* (Itasca, 2018) and *UDEC* (Itasca, 2014) using Voronoi tessellation technique, and *3DEC* (Itasca, 2016) could help to capture many complex behaviours.

Three hinge buckling (THB) is a simple buckling failure mode that Cavers (1981) described for rock slopes, and this mode is often observed in quarry floors. This failure mode includes two-rock block rotation at their central hinge, and two lateral hinges at the outside of the blocks interface, which cause fracturing at hinge locations, called 'crushing zone'. THB is a simplified and specific type of buckling, and before studying the complex and multi-blocks modes, it is crucial to fully understand the simple THB failure as a first stage. A clear understating of simple THB failure will lead us to a better understanding of the critical parameters that mostly involves buckling failure such as geometry effects, the impact of in situ horizontal stresses ($\bar{\sigma}_H$) and trigger mechanisms. Therefore, in this thesis understanding of the simple THB failure were aimed to achieve by studying of all reported buckling failure in the field, design and reproducing a new laboratory experiment and apparatus that can simulate the simple THB at laboratory scale, followed by numerical modelling to study the validity of the experiment and explore the feasibility of modelling the complex modes of THB failure.

1.2 Background

The thesis is comprised of several journal articles each presented as a chapter (Chapters 2 - 4) which each contain some form of literature review. This material is not repeated within a literature review chapter; however, some additional necessary background on buckling behaviour is presented here to complement the background materials in the following chapters.

The buckling behaviour of slopes has been a focus of many researchers. Concerning the slope cases, buckling occurs in slopes that have nearly parallel discontinuities to the slope face. Buckling failure in rock slopes is common in sedimentary laminated rocks. External forces like water pressure, stress concentration in the slab plane and the slab weight induce a tendency for buckling failure in slopes (Giani, 1992). Cavers (1981) presented an analytical buckling analysis method for slopes and declared that, generally, buckling failure occurs when the slope dip is steeper than the angle of internal friction parallel to the discontinuities direction of the slab. Occasionally, buckling may happen in the separated slabs in sedimentary rocks. It may also occur in other types of rock where the discontinuities are parallel to the slope face. Cavers (1981) divided the buckling analysis in three categories (Figure 1.1):

- Flexural buckling of a plane slope

- THB of the plane slope

- THB of curved slope

Tommasi et al. (2009) worked on buckling of slopes using the DEM (distinct
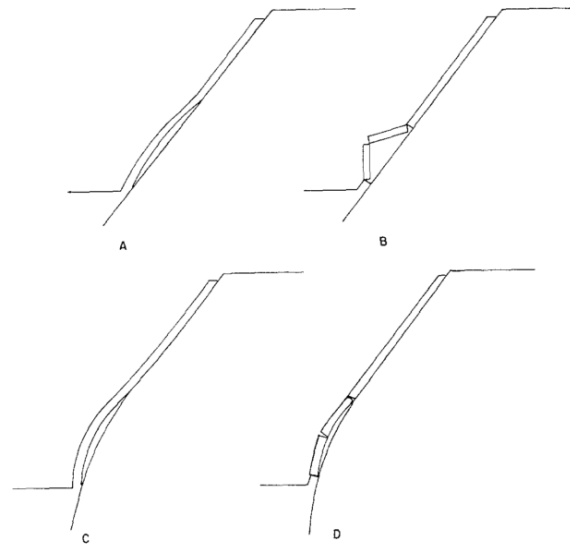
Figure 1.1: Possible type of buckling failure. a) Flexural buckling of plane slope; b) Three hinge buckling of plane slope; c) Flexural buckling of curved slope; d) Three hinge buckling of curved slope (Cavers, 1981)

element method) and DDA (discontinuous deformation analysis) back-analysis of a high-dip slope in northern Italy. They concluded that even in mild natural slopes with deficient discontinuities shear strength, and persistent bedding joints and layers, buckling failure might occur. Back-analysis is useful if the factors causing a change in stress distribution are adequately considered, such as minor flexures, water pressure in bedding joints, and failure of rock material. Using a numerical modelling study, they found that instabilities without significant water pressure along bedding joints or very weak parts of rock mass near the buckle axis may occur by minor local variation of geometry, which is usually hidden by buckling deformation. Therefore, rock avalanches may occur due to the evolution of buckling deformations.

Another type of buckling failure is the occurrence of THB in horizontally bedded rocks. In the areas with high in situ stresses, quarrying causes the redistribution

of stresses and increases horizontal stresses. As a result, there is a severe upheaval of a quarry floor. For example, in 1969 in Missouri, a 1.2 m thick bed of Salem limestone buckled, and rose almost 0.6 m and cracked for 90 m length. In Figure 1.2, a detailed cross-section of a multi-layered 'pop up' which occurred in a dolomitic limestone quarry is shown (Roorda, 1995).
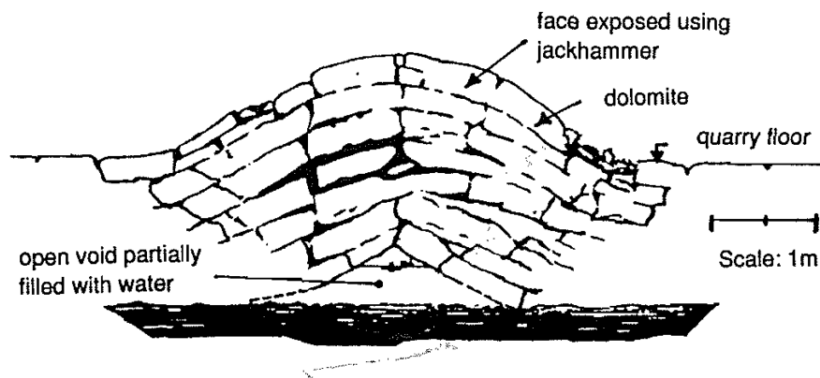
Figure 1.2: Section through a multilayered pop up in a quarry floor (Roorda, 1995).

Figure 1.3 illustrates the initiation and progression of buckling as a simplified basis, considering it as a continuous and jointed stratum. This formed the basis for the development of an analytical solution by Roorda (1995). In state A, the stratum is stable. As it is visible in state A-B, a finite disturbance, called a 'trigger', is required to initiate buckling. When stresses developed enough to initiate buckling, State B in the diagram occurs. Therefore, the stratum is moved explosively from state B to C in a dynamic fashion. In this state, a substantial reduction of strain in the heaved part can be seen.

Frequently, horizontally bedded near-surface rock strata also contain many vertical joints (cross joints). Since in situ compressive stresses exist, joints are tightly closed,

and this stratum is like a continuous unjointed plate, as visible in Figure 1.3. On the other hand, after bending the stratum, the stresses in some points are zero. As a result, it causes joints to open, as shown in Figure 1.2, thereby changing the buckling mode. Two approaches were presented to assess this problem. Nusayr and Paslay (1972); Roorda et al. (1982); Wang (1984); Roorda (1988) used a two-dimensional analysis, and Hobbs (1989, 1990) used the three-dimensional view of buckling, considering the axis-symmetry basis for the solution.
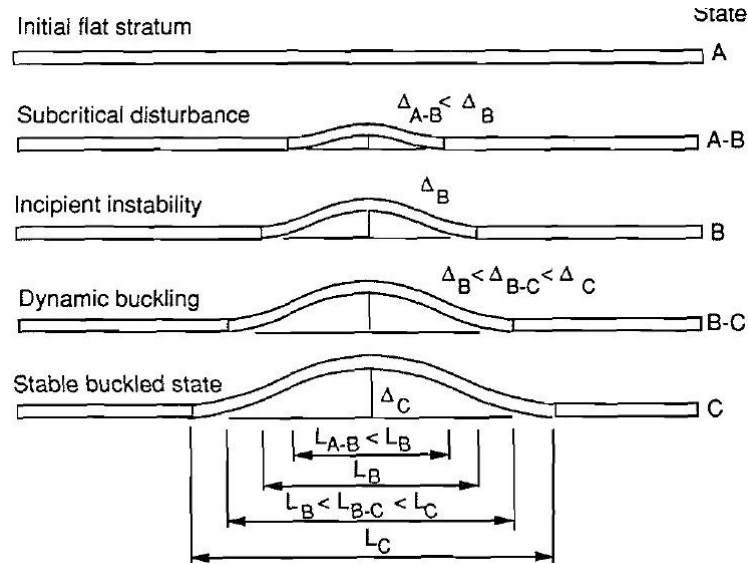
Figure 1.3: The growth of a pop-up as theoretical basis for analytical method developed by Roorda (1995).

Roorda (1995) considered an infinite elastic plate lying on a horizontal substrate with the axisymmetrical behaviour that uniformly compressed in all directions in order to investigate the fundamental features of 3D buckling mechanics. Under the axisymmetric assumption, horizontal in situ stresses were considered equal in all directions, although it is physically unrealistic. Based on this analysis, a minimum

initial in-plane compressive stress exists in each buckling process. Moreover, a small trigger disturbance is always required for the plane and heavy plates.

Diederichs and Kaiser (1999) worked to advance the Voussoir beam theory for rock buckling failure. They worked on beam snap-through failure, which is common in large spans of hard rocks. They have presented a simple and effective iterative algorithm for the stability analysis of laminated ground, and proposed a design chart based on linearity limitation (yield limit) for jointed rock beams, including the summarized relationship between span, thickness and modulus. Some improvement in assumptions were made, including lateral stress distribution and arch compression, the application of support pressure, and surcharge loading. Moreover, the linearity limit of midspan displacement was identified at around 10 percent of the lamination thickness. This displacement limit was used for a stability design chart because it is independent of rock mass modulus. Also, the authors normalized the design chart respect to:

- Effective specific gravity which is a function of rock density

- Excavation dip angle

- Surcharge loading or support pressure

They presented two modes of failure for thin lamination: 1. Snap-through failure and 2. Crushing failure. Also, they concluded that critical failure mode, the mode that presents a minimum critical span, determines the critical span of the beam. The authors suggested more work was needed to account for the parallel boundary

component of weight in steeply dipping Voussoir beams. While neglecting this component has a small effect on geomechanical limits for stability, equilibrium displacement predictions may be significantly in error for steeply dipping beams.

Handin and Pattison (1976) studied experimental folding of rock under confining pressure, including the buckling of multilayered rock beams. They highlighted some principal factors affecting the buckling failure of multilayered rocks, such as the mechanical effect of layers, factors controlling fold shape, superposition of stresses. For instance, they found that the critical buckling stress is higher for a thin-beam fold in single layers of limestone or sandstone than one with a three-layer specimen with the same thickness. Also, Lin et al. (1984) used physical modelling to create the failure of the opening in steeply foliated rock masses, and Kazakidis (2002) used an analytical method to quantify the unusual loading exist in a slab under buckling loading.

Similar work on buckling failure has been done by McDowell et al. (1956) using the Arching Action theory on masonry walls to generate static load-deformation curves for masonry beams having a solid cross-section. They considered a beam clamped at both ends. Figure 1.4 shows the deformed shape of the beam. They highlighted that the mode of response would be in the following order. First, cracks grew on the tension sides at the ends and center of the span when the loading starts. Then, cracks extension to the centerline of the beam observed. They assumed that each half of the beam stays rigid and rotates at the end and center in further motion. A couple force comes from resistance to this motion due to the crushing of the masonry materials at these positions established at the end and center. The rotation stops if either the

couple forces disappear, or the load is removed. The wall is destroyed in both cases. Their study is a suitable reference to compare with buckling failure in rocks.
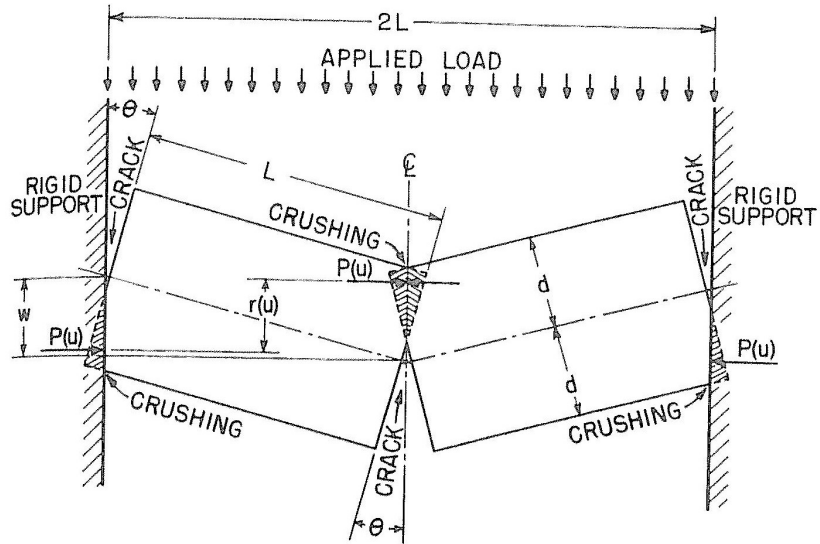
(a) Wall in Deflected Position
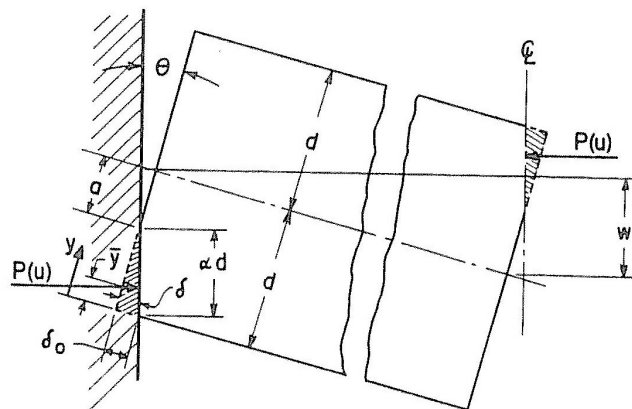
(b) Geometry at Support

Figure 1.4: Idealized Masonry Wall (McDowell et al., 1956).

Dawe and Seah (1989) experimentally studied the effects of some parameters such as boundary support effects, reinforcement of joint, and thickness of the panel for masonry infilled panels. The authors concluded that there is a transition at the first

fracture initiation from flexural mode to arching action mode in masonry infilled panels. They analyzed post-cracking behaviour, which is very similar to rock three hinge buckling. Figure 1.5 shows one type of strips in a deformed configuration.
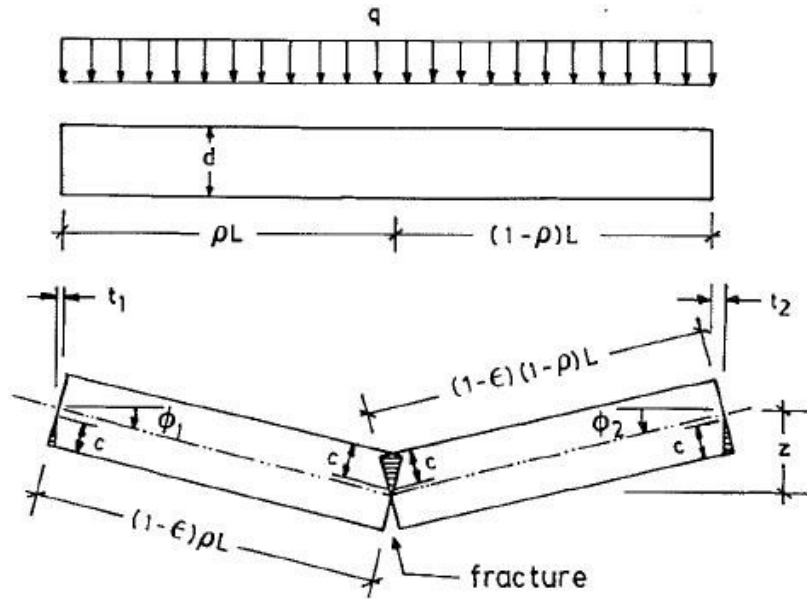
Figure 1.5: Type I strip in a deformed configuration (Dawe and Seah, 1989).

Given the complexity of buckling behaviour in rock, numerical modelling is a suitable analysis method. These methods can address complexities such as non-uniform and three-dimensional geometry, non-linear (inelastic) behaviour, block interaction, variable boundary conditions, etc. Conventionally, continuum methods were used to study rock mass behaviour around underground excavations especially involving buckling failure because of their computational efficiency; however, these methods have many limitations and they are not able to simulate buckling failure observed in the field (Karampinos et al., 2015).

In contrast, discontinuum numerical methods may be more convenient to use for buckling failure. The ability to model the complex behaviour of rock, especially rock

block deformations, rotation and movements, is the primary features of discontinuum methods. Although these methods are useful, long computer run-times and some other limitations of computation are challenging (Karampinos et al., 2015). Karampinos et al. (2015) used the distinct element method to simulate the buckling mechanism in foliated ground under high-stress conditions. Their model focused on the failure mechanism of hard rock in underground mining, considering the effect of geological structures which can not be suitably addressed with continuum methods.

Hsu et al. (2004) simulated the squeezing condition of a tunnel using the *UDEC* code, and they were successful in distinguishing the flexural tensile buckling of the rock mass. Vakili et al. (2012) back analyzed failures mechanism, specifically the buckling failure using *3DEC*.

Gao et al. (2016) used discrete element grain-based method to simulate the micro-structure of brittle rock. They used the recently developed *UDEC* Voronoi tessellation approach to simulate the brittle rock failure (Figure 1.6). Voronoi tessellation was used because of its ability to simulate the micro-structures of rock including fracture formation and propagation. Observing the complex macroscopic behaviour of intact rock could be achieved since micro-structures of grains control the micro-mechanical behaviour of rock. Hence, these features allow simulating both geometric and mechanical heterogeneity of brittle rock at the grain scale.

Mayer and Stead (2017) studied the limitation of using GBM for brittle fracture mechanisms. They found that mesh-geometry dependencies results in some uncertainties in calibration of the models. Although the limitation of kinematic freedom,
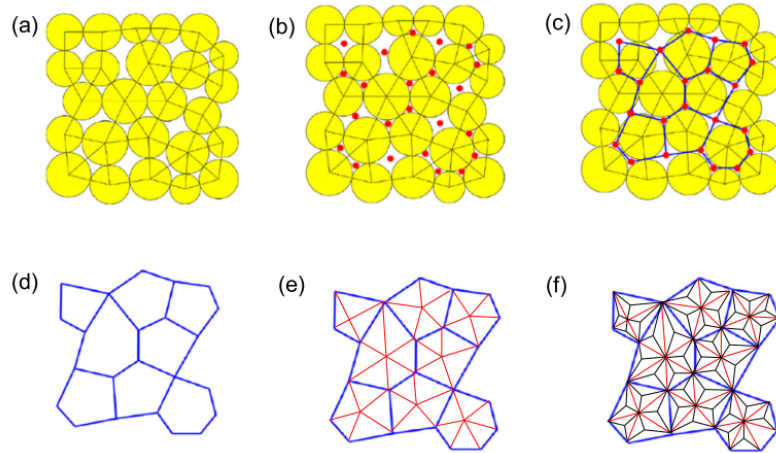
Figure 1.6: Grain structure generation. (a) Initial disk packing; (b) void centroids (red dots); (c) polygonal network; (d) grain structure; (e) intra-grain bonds (red lines) and (f) further discretization (Gao et al., 2016).

increasing the degree of interlocking and localizing the tensile failure developed by Voronoi meshing routines, an opposite effect can happen by the triangular mesh geometries. That is, it increases the kinematic freedom, and increases the potential for shear failure mechanism in models. They suggested doing some realistic simulation of intact rock samples to verify reproducing of the natural grain shapes and textures, due to the uncertainties that exist in GBM modelling.

1.3 Research Motivation, Objectives and Methodology

The existing studies showed that there is insufficient knowledge about the THB failure, and the frequent occurrence of THB failure in the field, especially in quarries, is a concern for the mining industry and society. Therefore, presenting a methodology that includes reproducing the THB failure in a controlled environment to improve the THB mechanism's understanding and quantify the THB instability is invaluable.

This methodology may also lead to a better understanding of buckling for other situations, like slopes and underground mining and gain some useful insights into brittle rock failure and numerical modelling of these things. This research aims to develop a methodology that predicts and quantifies the THB instability in quarry floors and open fields.

The The objectives of this research include: first, documenting and understanding field buckling observations, second, focusing on a simple THB buckling mechanism that occurs in the field, slopes and underground mining by presenting a new THB laboratory experiment. Third, conduct the THB experiment using the new THB experiment and carrying a parametric study on the rock. Finally, in the fourth step, capturing the THB failure with computer simulations for further parametric studies and feasibility of modelling the complex modes of buckling failure.

In the first step, an extensive study literature review was carried out on all previous works related buckling failure in rock, especially those whose focus was THB failure on quarry floors or similar conditions. Available documented and reported buckling cases across North America, including all available geological, geometrical and mechanical parameters recorded from buckling incidents, were obtained, where possible. Also, spatial and statistical analyses were carried out on the collected buckling data. This step's main purpose was to provide a comprehensive study of all possible buckling modes and a database that includes all past observed buckling events that had occurred in the field. This database is published in an open-source repository (Ghasemi and Corkum, 2020a) which can be continually updated by other

researchers when there are new documented cases.

Since THB is a relatively simply, but common type of buckling mode observed in the field, reproducing the simple THB is an important step to better understand more complex THB failures. Therefore, in the second step, a new laboratory experiment was developed to simulate a simple THB failure. This unique and new experiment was presented with a recommended standard procedure that could be followed by other researchers to simulate THB failure with different rock types and parameters.

The third step was conducting the THB test using the newly-developed experimental analysis on rock specimens. Seven THB tests were carried out on Wallace sandstone: a well-known and understood, homogeneous rock type that was available commercially here in Nova Scotia. These tests revealed meaningful results about THB failure, which led to a better understanding of the failure mode and to identify the critical parameters in THB instability. In this experiment, the acoustic emission (AE) system and digital image correlation (DIC) method were also used to capture parameters such as the fracture initiation and propagation that cannot be practically captured using conventional measurement instruments.

The fourth step was development of a numerical simulation of the THB experiment that was carried out using the commercial code *UDEC* utilizing Voronoi tessellation and calibration of this model with laboratory data. This model can capture internal fracturing with the rock blocks and the complete buckling process. This calibrated model provided insight into the test and allow for exploration of the impact of various critical parameters that were not practical to explore in the lab.

1.4 Document Overview

This document is organized following the 'paper format' specified in the Faculty of Graduate Studies of Dalhousie University's thesis guidelines. Chapter 1 provides an introduction to the subject and objectives of this research. Chapter 2 presents a review paper submitted to the journal Rock Mechanics and Rock Engineering (currently under review) and provides a detailed literature review of the field cases and buckling modes, including a buckling events database and spatial and statistical analysis of buckling events. Chapter 3 presents a published paper in the journal Rock Mechanics and Rock Engineering, introducing a novel THB laboratory test developed for this research study. Chapter 4 includes a paper submitted to the journal Rock Mechanics and Rock Engineering and presents THB experiments carried on Wallace sandstone, followed by the numerical modelling developed using the *UDEC-GBM*. Finally, Chapter 5 provides a summary of the research findings and conclusions, and recommendations for future work. Also, the preliminary works of this study related to development of the THB experimental design, prepared as a conference paper in ARMA 52nd US Rock Mechanics / Geomechanics Symposium (Ghasemi and Corkum, 2018), is included in Appendix A.

Chapter 2

Ground surface rock buckling: analysis of collected cases and failure mechanisms

M. Ghasemi, A.G. Corkum, G.A. Gorrell

2.1 Abstract

The potential for spontaneous failure of quarry pit floors by various buckling modes has increasingly become a concern because of the potential impacts on safety, the environment and mining operations. The most notable and concerning form of buckling failure is referred to as a 'pop up' which is a nearly-instantaneous and violent event similar to a rock burst. A means to evaluate potential risk to this hazard from a rational engineering framework is required to aid with licensing and operations decisions. As a first step understanding the likelihood of buckling event occurrence under various conditions requires a thorough compilation of past observed in situ events. In this study a database of observed cases has been collected and presented to provide insight into the various buckling failure modes and associated geotechnical conditions. Although documented case study details vary significantly, the collected

data is of value. When available, the database includes information on the geological environment, rock type, mechanical properties, in situ stresses, and buckle dimensions. Following presentation and analysis of the collected cases database, a review is presented of the main buckling-related failure modes and a summary of associated typical analysis methods.

Keywords: buckling, pop up, exfoliation, in situ stress, quarry

2.2 Introduction

Spontaneous buckling of near-surface rock formations has been observed as a geological phenomenon for many decades now. These events have been documented in Canada, Australia, the United States and elsewhere: some examples are provided by Adams (1982); White and Russell (1982); Everitt (2009); Twidale and Bourne (2009). Sometimes referred to as 'pop ups' or 'A-tents', these buckling events often occur rapidly and without warning. These 'failure' events have been observed in various rock types and formations: sedimentary, metamorphic and igneous. Several buckling modes have been observed, some with geological structural controls and some have also occurred in relatively intact rock (e.g., exfoliation). Often these events occur in stiff rock units under high horizontal stress, but have also been observed to occur in relatively weak and soft rocks, such as shales. Buckling sometimes involves unbedded, massive rock, single near-surface beds or multiple beds in a complex failure mode. In North America these buckling events seem to occur predominantly in stiff, bedded limestone/dolomite formations of Ontario and the Upper Midwestern U.S. and have been observed in quarry floors. Various examples of buckling failures are shown in Figure 2.1.

Recently, environmental regulators in Ontario, Canada, have shown significant interest in understanding the potential for spontaneous buckling events following a significant quarry floor buckling event in the Ottawa region of Ontario. This buckling event resulted in development of a hydraulic connection between the quarry floor and its underlying aquifer, with detrimental environmental and mine operational
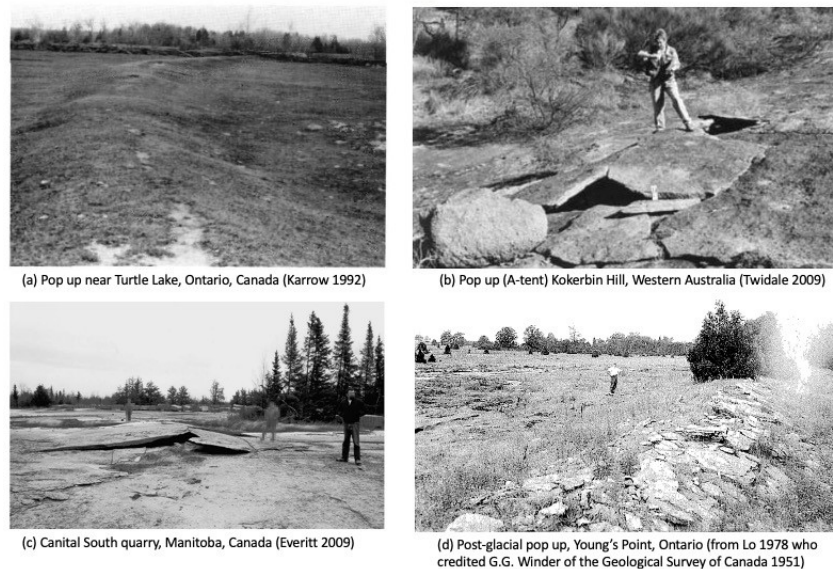
Figure 2.1: Examples of pop ups observed at various locations and conditions. (Photos from: Karrow (1993); Twidale and Bourne (2009); Lo (1978); Everitt (2009))

implications (Crossley, 1991). As a result, the regulator and quarry operators have expressed interest in quantifying the risk of spontaneous buckling events related to their operations. This could also have implications for other near-surface engineering structures, such as building foundations, dam foundations and abutments, and rock slopes and mine pit floor failure (Brawner, 2003).

Spontaneous buckling events should be considered as a geohazard with a rational means of analysis and evaluation, and an appropriate risk assessment methodology. Some analysis methods have been developed for buckling under specific circumstances and failure modes (e.g., Roorda et al. (1982); Diederichs and Kaiser (1999); Tommasi et al. (2009)), but in general, there is currently no clear means of quantifiable stability evaluation. A first step of understanding the mechanisms of buckling events is to

document observed events and associated geological conditions. Given the recent relevance of buckling of quarry floors and the need for development of a rational basis for analysis and evaluation of geohazard assessment, the purpose of this paper is to present a review of spontaneous buckling events and to present a database of case histories in North America. In addition, the various modes of buckling failure and analysis approaches in the existing literature are presented.

Within a geological context, buckling and folding of rock stratum is commonly observed as a result of metamorphic processes. Typically, such folding and distortion occur at depth under high pressure and temperature conditions, and as a result of large-scale geological processes. These processes typically occur over relatively long time-scales. In contrast, the focus of this study is on relatively short-term buckling occurrences in the near-surface environment. These events typically occur relatively rapidly, or even nearly instantaneously; however, some cases may involve a component of time-dependent processes, such as weathering or erosion. It can be sometimes difficult to clearly differentiate between the long-term geological folding and buckling of metamorphic processes, and the relatively rapid, spontaneous buckling events that are the focus of this study.

2.3 Regional Geology and Stress Regime

An extensive literature review was carried out to develop a database from literature sources of spontaneous buckling events across wide ranging conditions. Although such events have been observed internationally, the focus of this study is North American

events primarily within Ontario, Quebec and the Upper Midwestern U.S. The geological setting and in situ stress conditions in this region are first described to provide context for the collected cases.

2.3.1 Geological Setting

The region of interest in this study is the central portion of the North American Craton (Laurentia). In particular the provinces of Ontario and Quebec, Canada, and the upper Midwestern U.S. and New York state. The summary is focused on geological units of Cambrian–Ordovician age in the region that are of particular interest to the quarry operations and the aggregate industry where buckling failure has typically been observed. The Northern portion of this region is characterized by igneous and metamorphic rocks in the Superior Province ('Shield'). In the southern portion, the metamorphic and igneous basement rock has been overlain by deposits of sedimentary rock, such as shales, and carbonate deposits (dolomite and limestone). The northeast-southwest trending Algonquin Arch separates the Michigan and Appalachian Basins in Southern Ontario.

Thirteen sedimentary formations described in the literature and geological mapping are listed as they are found within the Ottawa Basin, and eight are found within the Central Basin. Within the context of this paper, Central Ontario extends from the base of the Niagara escarpment in the west, to the Frontenac Axis in the east. The Axis extends northwestward from the Gananoque area to Sharbot Lake. Lake

Ontario forms the southern margin, and the Central Ontario sequence extends northward to the Marmora, Madoc, Tweed and Verona areas. The Ottawa Basin Paleozoic sequence extends from the Frontenac Axis to the Quebec Border. The St. Lawrence River is the southern margin and the Ottawa River is the northern. These stratigraphic basins are shown on Figure 2.2 and Figure 2.3.
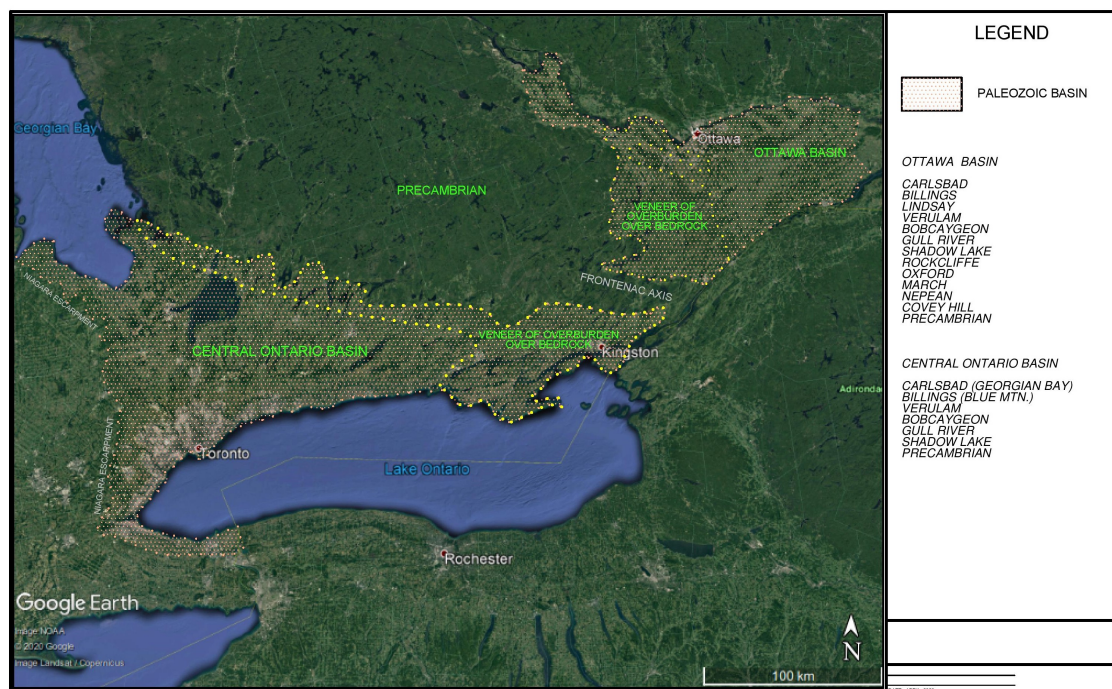
Figure 2.2: Paleozoic Basins of Ontario. (Satellite image modified from Google Earth)

Information about these formations can be found in Armstrong (2000); Wilson (1964); Liberty (1969, 1971); Williams and Telford (1986); GRI (1993). The formations that may be present in central and eastern Ontario, Quebec and American northeast are listed in Table 2.1 from youngest to oldest along with a generalized lithographic description. Precambrian-aged bedrock is found along the northern margin of the area, centrally as the Frontenac Arch and in inliers scattered throughout.
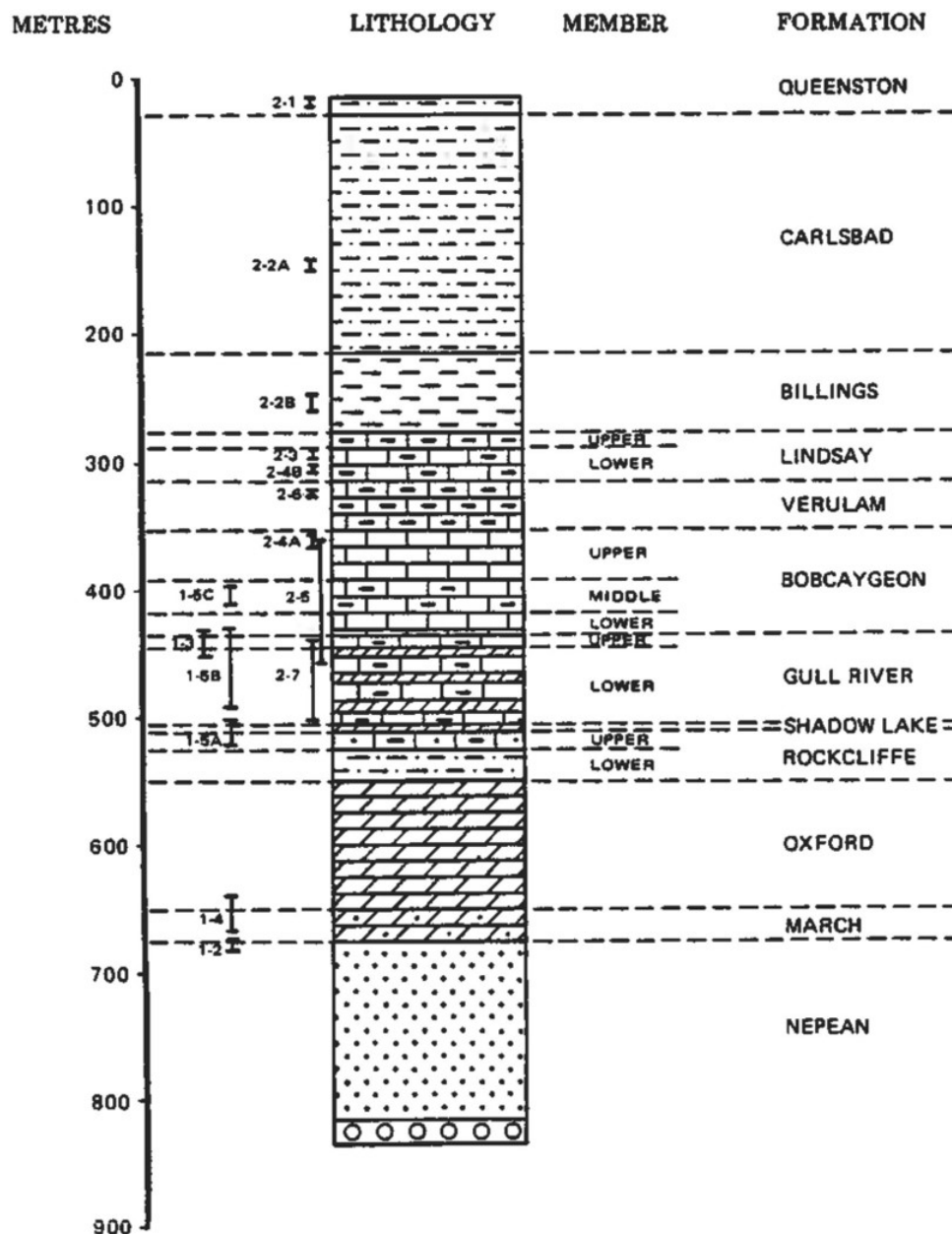
Figure 2.3: Stratigraphy of the Ottawa area (Williams and Telford, 1986)

Table 2.1: Bedrock Formations within Eastern Ontario

Formation	Alternate Name	Lithology	Environment	Construction Aggregate Ranking
Formations in Central and Ottawa Basins				
Carlsbad	Georgian Bay	Interbedded shale, siltstone and silty limestone	Intracontinental shelf	Not Suitable
Billings	Blue Mountain	Dark brown to black shale	Intracontinental shelf below wave base	Not Suitable
Lindsay		Limestone with shale interbeds	Intracontinental shelf but above wave base	5
Verulam		Limestone with shale interbeds	Intracontinental shelf but above wave base	5
Bobcaygeon		Limestone with planer to wispy shale beds	Intracontinental shelf but above wave base	3
Gull River		Interbedded limestone silty dolostone, quartz sandstone and shale	Supratidal to intertidal intracontinental with terrigenous influence	4
Shadow Lake		Silty to sandy dolostone with shaly partings and interbeds of quartz sandstone	Supratidal to intertidal intracontinental with terrigenous influence	Not Suitable
Formations in Ottawa Basin only				
Rockcliffe		Interbedded quartz sandstone and shale	Supratidal to intertidal intracontinental with terrigenous influence	7
Oxford		Dolostone with subordinate shale and sandy beds	Supratidal to intertidal hypersaline	1
March		Interbedded quartz sandstone, dolomitic quartz sandstone, sandy dolostone and dolostone	Supratidal to subtidal	2
Nepean		Interbedded quartz sandstone and conglomerate	Marine lower intertidal to subtidal to terrestrial braided river	Not Suitable
Covey Hill		Conglomerate and sandstone	Terrestrial	Not Suitable

The bedrock formations in Table 2.1 range in age from Cambrian through the Ordovician-aged Formations (*ca.* 488.3 to 443.7 million years ago). Seven of these formations are ranked as construction aggregate based on the usability of the stone that is derived from them. The ranking is provided with the lithology because some floor buckles or pop ups in the literature are described or characterized as having developed and deepened within a formation (White et al., 1973; White and Russell, 1982; Adams, 1982; GRI, 2017). In other cases, pop ups have been observed in open, undisturbed fields (Gorrell, 1988; Rutty and Cruden, 1993). The ranking of the formation as a construction aggregate is rated since the excavation of the bedrock may cause a pop up and consequently identifying which formations are more likely to be excavated will also provide information on the likelihood of pop up occurrence.

Separate Paleozoic stratigraphic sequences are present in Central and Eastern Ontario. Not every formation is present within a given area in either basin because of faulting and/or erosion.

The bedrock is relatively flat lying locally in each Basin. However, on a regional scale, there is significant change because of steeply dipping faults and fault zones. Williams and Telford (1986) indicated that the faults in the Ottawa Basin have displacements up to 1,200 m. In the Central Basin there is a thin veneer of sediment overlying the bedrock from the Frontenac Axis, west to approximately Trenton where the thickness of the overburden increases to more than 100 m. East of Trenton the bedrock is generally on, or near the surface on the northern periphery adjacent to where the Precambrian bedrock is exposed. The unconsolidated sediment in this area

were deposited during and after the last ice age.

The Queenston is the youngest formation in the Central and Ottawa Basins. It consists of interbedded siltstone and shale. In the Ottawa area it is up to 50 m thick. The siltstone and shale are thinly to thickly bedded and are red to greenish grey (Williams and Telford, 1986). The two formations that underlie the Queenston consist mainly of shale. Underlying the Queenston is the Carlsbad Formation. The Carlsbad consists of interbedded shale, siltstone and silty limestone (Wilson, 1964). The siltstone and limestone are thinly to medium bedded and medium to dark grey. In the Ottawa Basin the Formation is up to 187 m thick (Williams and Telford, 1986). Beneath the Carlsbad Formation is the Billings Formation. The Billings consists mainly of dark brown shale. The shale is dark brown to black. In the Ottawa area the formation is up to 62 m thick (Williams and Telford, 1986).

The Lindsay Formation underlies the Carlsbad. It consists of limestone with shale interbeds. The limestone is sublithographic to coarsely crystalline, very thinly to thickly bedded, light to dark grey to brownish grey in colour, and bluish grey to brown when weathered (Williams and Telford, 1986). Burrows, feeding trails and intraclasts are common. Abundant undulating shaley partings occur and a nodular structure is characteristic of the whole formation (Carson, 1981). Shale beds are commonly 5 cm thick or less throughout the lower portion.

The Verulam Formation underlies the Lindsay Formation. This formation consists of limestone with shale interbeds. The limestone is sublithographic to coarsely crystalline, very thinly to medium bedded, light to dark grey to brownish grey and brown

when weathered. Burrows and intraclasts are common and ripple marks are present in some beds. Interbeds of dark grey calcareous shale are up to 15 cm thick (Williams and Telford, 1986). The conformable upper contact with the Lindsay Formation is the upper limit of shale interbeds greater than 5 cm. Armstrong (2000) indicates that the thickness of the formation ranges from 45 to 60 m and Williams and Telford (1986) indicated that the formation ranges in thickness from 32 to 40 m. Due to the low strength (i.e., load-bearing capacity) of the shale in the two formations, their use in construction aggregate production is limited, and the formations generally only meet the requirements for granular aggregates (Gorrell and Fletcher, 1987; Gorrell, 1988).

In terms of usability as a construction aggregate, the Bobcaygeon Formation is the preferred bedrock formation in the Central Basin, and it is ranked 3rd in the Ottawa Basin. The formation consists of interbedded calcarenite and very fine-grained to crystalline limestone. The calcarenite is light to medium gray, weathering to bluish to brownish grey. The geological boundary of this formation with the underlying Gull River Formation is gradational, which in section represents a gradual change in characteristics (Williams et al., 1984; Gorrell, 2012).

Potassium-rich bentonite clay layers (K-bentonite) are often observed near the contact of the Bobcaygeon and Gull River Formations. These layers are altered volcanic ash that has been correlated to a major volcanic eruption during the Middle Ordovician Period (Mitchell et al., 2004; Armstrong and Dodge, 2007). The layer thickness ranges from less than 2 cm to greater than 50 cm.

The Gull River Formation, which is up to 55 m thick in the Central Basin and ranges in thickness from 50 to 71 m in the Ottawa Basin consists of interbedded silty dolostone and very fine-grained to crystalline limestone, with less frequent beds of shale and fine-grained calcareous quartz sandstone. The silty dolostone is pale greenish grey to medium grey and weathers buff to reddish brown. It is thinly to thickly bedded, calcitic to non-calcitic, with conchoidal fractures, and common calcite-filled vugs. The very fine-grained to crystalline limestone is tan to dark grey and weathers white to bluish grey. It is medium to thickly bedded, commonly with intraclasts, oolites, and calcite 'eyes' (Williams and Telford, 1986; Armstrong, 2000).

The Rockcliffe Formation, which underlies the Gull River Formation, consists of interbedded quartz sandstone and shale. Williams and Telford (1986) indicated that the Formation ranges from 48 to 52 m in the Ottawa Basin.

The Oxford Formation consists of dolomite with subordinate shale and sandy beds. The dolomite is medium brown to grey in colour. Calcite-filled vugs, and fine to coarse grained sand is common. The sand content increased with depth. The thickness of the Oxford Formation in the Ottawa Basin ranges in thickness from 62 to 102 m (Williams and Telford, 1986).

The March Formation consists of interbedded quartz sandstone, sandy dolomite, dolomitic sandstone and dolomite. The dolomite is medium brown to grey and the sandstone is white to grey. The sandstone beds often have green tinges. Cross-bedding and cross-lamination (ripples) are common. The sand content increases substantially downward through the formation. The thickness of the March Formation ranges from

18 to 20 m (Williams and Telford, 1986).

The Nepean Formation consists of interbedded sandstone. The sandstone consists of fine to coarse quartz grains that are white to light grey to brown in colour, with some green tinges. Cross-bedding, cross-laminations and other sedimentary bedforms are common. The thickness of the Nepean Formation ranges from 60 to 159 m.

The Covey Hill Formation consists of interbedded feldspathic conglomerate and sandstone, and unconformably overlies the Precambrian bedrock (Williams and Telford, 1986). The formations are differentiated by their composition. The sandstone and the matrix of the conglomerate consist of fine to coarse quartz sand with angular pink feldspar grains. The conglomerate consists of pebble to boulder sized sub-angular to well-rounded clasts. The formation has limited uses. It has been quarried for aggregate locally and has been used as a source or silica for ceramics.

2.3.2 Regional In Situ Stresses

The majority of surface buckling cases are stress-driven phenomenon largely driven by the in situ maximum horizontal stress (s_H) often combined with a failure triggering mechanism. In excavation environments (e.g., quarries), the stress can also be influenced by excavation-induced stress conditions. In addition, most of the documented violent buckling events have been observed in relatively stiff, good quality rock under high s_H conditions. Therefore, it is important to understand the in situ stress regime in the North American Craton as context to the buckling case study database. The focus of this summary is the in situ stress regime in Ontario which is the location

of the largest number of pop ups and is also the most well studied and quantified in terms of situ stress conditions, with somewhat similar conditions throughout much of the North American Craton.

Without the effects of tectonics, according to elastic theory, the magnitude of s_H due to lithostatic stress can be determined based on Eq. 2.1 for maximum (s_H) and minimum (s_h) horizontal stress. Where ν is the Poisson's ratio, ρ is the average rock density, g is the gravitional constant, and z is depth below ground surface.

$$s_H = s_h = \frac{\nu}{1 - \nu}\rho g z \tag{2.1}$$

However, this simplified condition rarely occurs in nature. According to Zoback et al. (1989) there are two primary categories of stress that contribute to the in situ stress regime. One is related to tectonic processes and is relatively similar over large spatial extents, and the second relates to topography, stiffness of rock units, and weathering / alteration, etc., which are more spatially localized. The tectonic component is largely similar throughout the North American Craton; however, local influences, such as topography of the Niagara Escarpment and the difference in near-surface rock types from the igneous rocks of Northern Ontario to the sedimentary rocks in Southern Ontario. The presence of faults and inclusions can also be a significant influence.

The in situ stress regime in Ontario has been studied by numerous researchers for critical infrastructure, nuclear power and nuclear waste isolation and the mining industry; an important component of the Ontario economy. One of the earliest studies

on compiled in situ stress data in Ontario was conduced by Adams and Bell (1991) who proposed Eq. 2.2.

$$s_H = 0.027z \ (\text{MPa}) \tag{2.2}$$

More recently, Kaiser and Maloney (2005) compiled a large database of in situ stresses in Ontario. The database included data compiled by Arjang (2001) and was later updated by Yong and Maloney (2015). Based on analysis of the collected data, they suggested that the in situ stress state in Ontario can be divided into three separate 'stress domains' defined by depth. They proposed Eq. 2.3 for the upper 300 m which is the domain of interest for this study on near-surface buckling. The equation included a plus / minus range.

$$s_H = 5.768 \left(\pm 3.358 \right) + 0.071 \left(\pm 0.019 \right) z \ (\text{MPa}) \tag{2.3}$$

Lam et al. (2007) proposed a range of in situ stress gradients shown in Eq. 2.4 as part of a study for a proposed nuclear waste storage project in Ontario.

$$s_H = 0.051z \ \text{to} \ 0.064z \ (\text{MPa}) \tag{2.4}$$

Amadei et al. (1988) and Esterhuizen et al. (2010) have stated that the stiffness of various rock units can have a significant impact on s_H, with stiffer units 'attracting' stress and softer rocks 'shedding' stress. This was also explored by LeRiche et al. (2017) using borehole breakout observations. Corkum et al. (2018a) investigated

the in situ stress state at the Bruce nuclear site utilizing site-specific geotechnical conditions and borehole breakout observations to develop an in situ stress model that accounts for stiffness of the various geological units at the site. The model includes vastly contrasting magnitudes of s_H with depth through geological units of variable stiffness.

Although horizontal in situ stresses are typically represented using the k ratio (s_H/s_v), this approach implies that $s_H = 0$ immediately at the ground surface where $s_v = 0$. In contrast to this, the observed pop up buckles indicated the presence of significant magnitudes of s_H at the ground surface. Given that horizontal in situ stresses in Ontario are dominated by the tectonic component, it seems likely that horizontal stresses at the ground surface are often significant. Lo (1978) described the high stress state in Fenoscandia and Ontario and concluded that high horizontal stress are likely a global phenomenon with the presence of significant horizontal stresses even at ground surface. Moreover, stresses at, or near the surface can be elevated, particularly within stiff units that are interspersed with softer layers. However, the near-surface environment is also heavily influenced by topography and weathering – often a moderating influence on stresses. The in situ stress models of Adams and Bell (1991) and Lam et al. (2007) result in $s_H = 0$ at ground surface, while the models of Kaiser and Maloney (2005) and Corkum et al. (2018a) both indicate significant s_H at or near the ground surface. The Kaiser and Maloney (2005) model suggests $s_H = 2.4$ to 9.1 MPa at ground surface for the Ontario-wide database. The site-specific model of Corkum et al. (2018a) suggests $s_H = 12$ MPa at ground surface at the Bruce

nuclear site near Kincardine, Ontario.

In addition to the magnitude of near-surface stress, the orientations relative to buckling is important. The symbol β_H denotes the orientation of s_H. The orientations of β_H from 2016 World Stress Map database version (Heidbach et al., 2018) (referred to as WSM2016) and from the Kaiser and Maloney (2005) study (referred to as MIRARCO2005) were collected. The orientation of β_H are presented in Table 2.2 and in the rosette plots in Figs 2.4 and 2.5. From WSM2016 the dominant trend is a northnorthwest–southsoutheast orientation for s_H in the North American Craton, while the data from MIRARCO2005 is slightly different with a dominant northwest-southeast trend in Ontario alone. In both datasets there is local variability due, predominantly, to geological and topographical conditions. In Section 3 these in situ stress orientation will be compared to buckling orientations.

Table 2.2: Summary of β_H from Rosette plot with 10° groupings

Geographic jurisdiction	Predominant β_H (number of data points)	
	WSM2016	MIRARCO2005
Ontario	$330 - 340°$ (16)	$300 - 310°$ (52)
Quebec	$310 - 330°$ (31)	
New York	$320 - 350°$ (8)	
North America	$330 - 340°$ (55)	
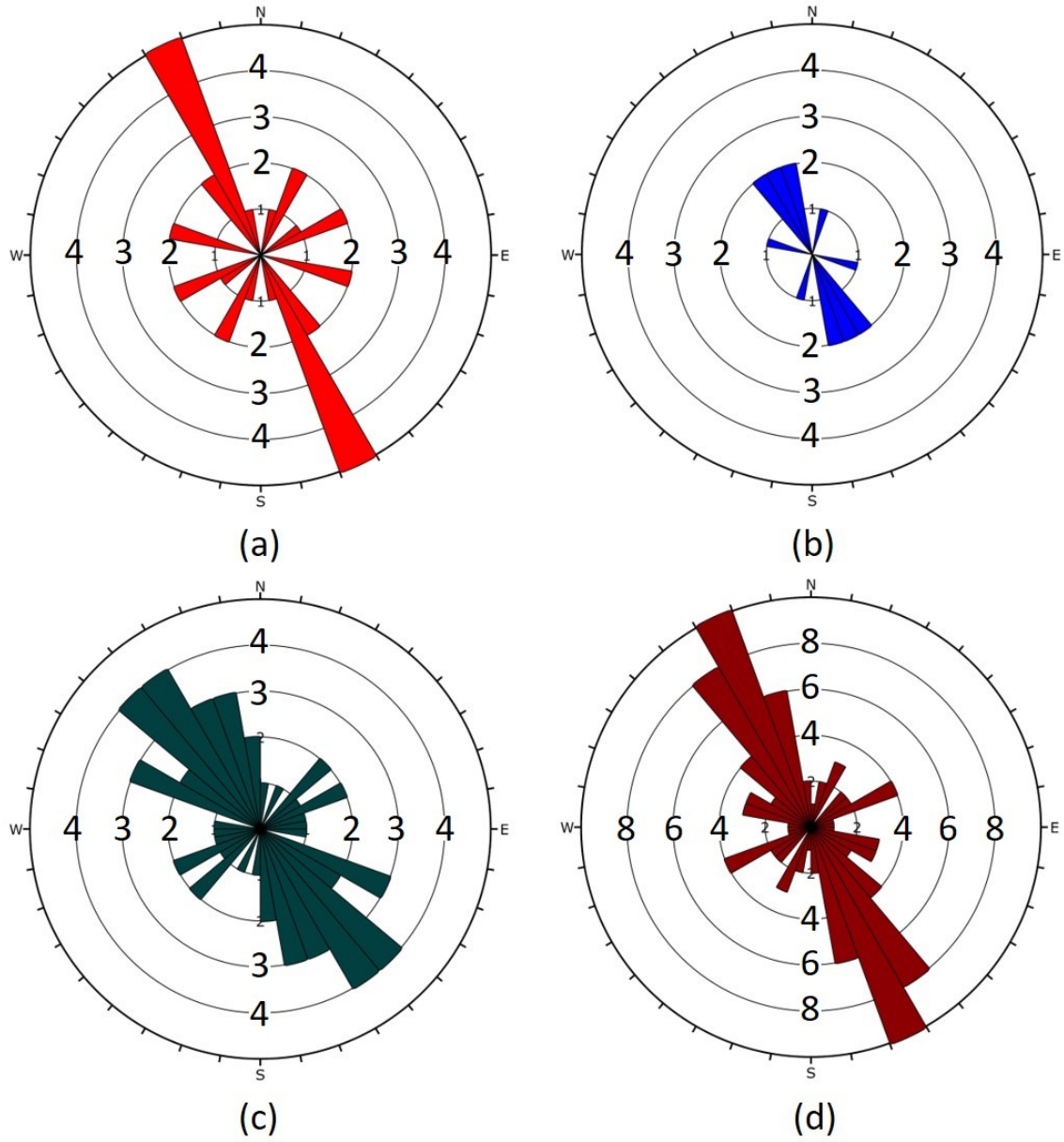
Figure 2.4: Rosette plots of β_H from WSM2016 (for different geographic jurisdictions (number of data points in brackets): (a) Ontario (16); (b) New York (8); (c) Quebec (31); (d) North America (55)
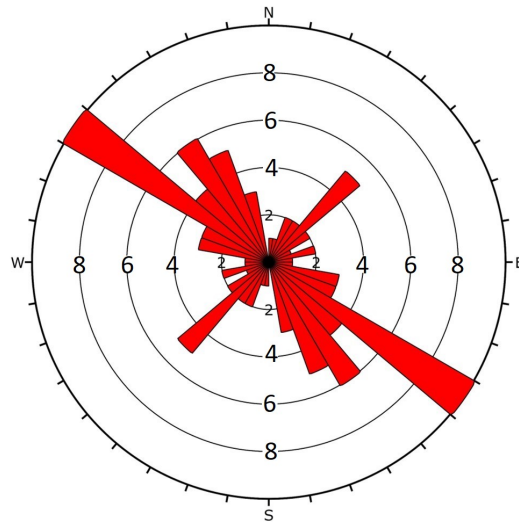
Figure 2.5: Rosette plots of β_H in Ontario for the upper 300 m domain from MI-RARCO2005 (52 data points)

2.4 Collected Surface Buckling Cases

As a key step in understanding surface buckling failures, an extensive literature review was conducted to compile observed case history information and to conduct some basic analyses on the documented, associated parameters. The focus of the case studies are spontaneous near-surface buckling events; however, in some cases it was difficult to differentiate events that may have occurred over longer time-frames from the fairly rapid events of interest in this study. In the majority of documented cases the buckling mode (e.g., THB) is not reported.

2.4.1 Sources of Case Study Data

In this study, a literature review was conducted on past buckling cases in North America with a focus on the North American Craton regions of Ontario, Quebec,

the Upper Midwest U.S. and New York state. Occasional documented cases in North America outside of the focus region are also mentioned for completeness. The available details of the case studies varied; however, often various dimension, rock type and orientation data were available for quantification. In total, 401 reported cases in the focus region documented by various authors were collected in this study and used to create a case study database that has been submitted to an online dataset repository for archiving (Ghasemi and Corkum, 2020a).

In this study the following dimensions will be used to describe the buckling events: length (L_b) is the length along strike of the bucking axis; width (W_b) is the width of the buckling perpendicular to the buckling axis; thickness (T_b) is the vertical thickness of the buckled material; and height (H_b) is the height of the buckle above original ground surface. Both T_b and H_b can include both single and multiple rock layers. In addition, α_b is the orientation (azimuth) of the buckling direction in the direction perpendicular to the buckling axis. These dimensions can be shown in Figure 2.6. It should be noted that some events, particularly those with a long buckling axis, include multiple measurements and changes in orientation along the buckling axis. As a result, the number of measured data points sometimes exceeds the number of total cases with multiple measurements associated with some single buckling events. The major buckling events and literature sources are summarized in the remainder of this section.

Saull and Williams (1974) mentioned four buckling events at St. Eustache and Terrebonne in the Montreal area. Two buckling events occurred in a dolomite quarry
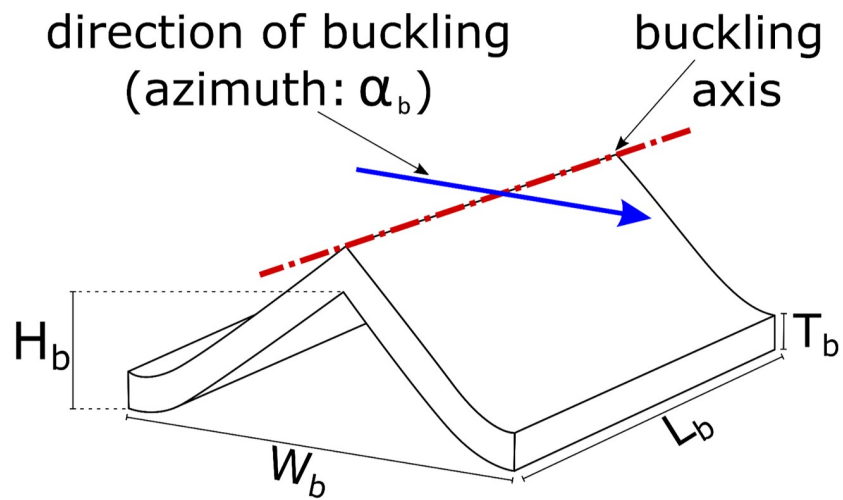
Figure 2.6: Schematic sketch showing parameters used in this study

at St. Eustache, and the other two occurred in limestone and carbonate quarries at Terrebonne. Buckling orientations at Terrebonne site were southeast, with L_b of 100 and 40 m. The maximum H_b at this location was 1.5 m with W_b of 18 m. The other two bucklings that occurred in St. Eustache were oriented southeast and east-west. For the southeast pop up L_b was 30 m, and the east-west L_b was 45 m. Both pop ups at this location were heaved about 1 m with W_b of 10 m.

Lo (1978) reported five buckling failures at the bottom of open excavations, only two of which occurred in quarries. The buckling in Dufferin Quarry, Ontario occurred in dolomite heaved (H_b) between 0.6 to 0.9 m. The buckling length varied between 15 to 76 m with seven ridges of heaves observed in this quarry. Marmora quarry in Ontario is another quarry where buckling has been reported. The pop up was oriented northwest and had occurred in the limestone bedrock. The reported buckling had a

H_b of about 2.4 m with an approximate L_b of 150 m. The author reported two more buckling failures occurred on canal floors: one in Queenston-Chippawa canal at Ontario and one in Barge Canal in Lockport, NY. Although Lo mentioned several buckling incidents at Queenston-Chippawa canal, only one case has been reported. The Queenston-Chippawa canal buckling occurred in limestone and heaved about 0.9 m over a length less than 1 km. The buckling case of Barge Canal in Lockport occurred in shale with L_b greater than 90 m and H_b about 0.6 m. Lo reported another pop up at Young's Point in Ontario. This failure has occurred in an open field with the southeast direction in the limestone bedrock.

Adams (1982) reported the occurrence of 12 buckling events at McFarland quarry in Ottawa. The buckling incidents reported by the author have occurred in six structures. The well expanded buckling structure in this area has occurred in three segments with an overall northwest-southeast orientation. The maximum L_b for this structure was 180 m, and the maximum H_b was between 1 and 1.5 m. The shortest buckling event reported in this quarry had L_b of 20 m and H_b about 0.5 m in a northwest-southeast direction. The author reported a 'z-shaped' buckling structure, which includes three segments. Two of these segments were heaved 0.1 m with a L_b of 55 and 25 m, with an northeast orientation. The other segment with the 20 m L_b was heaved about 0.5 m in the southeast direction. Three remaining buckling structures, two of which occurred in the direction of northwest-southeast heaved for 0.4 and 0.25 m with a L_b of 70 and 55 m respectively, and the other one has occurred with the northwest-southeast orientation and which was heaved 0.3 m with the L_b of

55 m.

White and Russell (1982) recorded 33 buckling incidents over an aerial extent covering approximately 400 km extending from Hamilton to Ottawa, Ontario. There are 27 pop ups recorded in open fields, and there is no record of the bedrock type for these locations. Four of these incidents were reported in Oakville. Two of which have oriented to northeast, and the other two directed to southeast. Also, the orientation of five pop ups at Tullamore, Woodbridge, Wellman, and two cases in Toronto reported as northeast. Wallach et al. (1993) reported that the bedrock at the Wellman location is limestone. The nine pop ups reported in Fenelon Falls have southeast orientation in the range between 100° to 128°. Pop ups occurred at Clairvile, Zimmerman, and Menie had oriented north-south, and the pop ups reported at Lorne Park, Burlington, Scarborough, Woodview, Hoard, and Pte. St. Anne were oriented southwest. Unfortunately, there is no record of buckling dimensions from these reported events.

White and Russell (1982) reported six bucklings in quarry floors in addition to the pop ups reported in open fields. Two buckling incidents reported in Milton, Ontario with the orientation of 45° and 141°. The two bucklings in Ottawa were oriented northeast, and another one oriented southeast. The last incident reported by authors has occurred at Roblindale, Ontario, with an orientation of 135°. Based on the cases that White and Russell (1982) reported in this area, the dominant orientation of these failures was northwest-southeast, with a median of 120°. However, there were 12 pop ups with the orientation of northeast-southwest.

Williams et al. (1985) described three buckling events with the limestone bedrock

at Port Colborne quarry in Ontario. The orientation of these failures reported as northwest-southeast except for one, which was northeast-southwest direction. The northwest-southeast oriented failures heaved 0.5 and 0.3 m with a L_b of 1.5 and 100 m, respectively. The northeast-southwest oriented failure was heaved about 0.15 m for 20 m in length.

Crossley (1991) reported a pop up in limestone bedrock at Wood's Sand and Gravel quarry in Kingston, Ontario. The buckling failure was oriented 135° with H_b about 1.5 m and L_b of 35 m. This particular event was noteworthy because of the observed hydraulic connection between quarry floor and the underlying aquifer caused by the buckling event.

Karrow (1993) noted nine open field buckling events at Manitoulin Island in Ontario. Three pop ups were recorded in dolomite bedrock. Two of these pop ups with the orientation of northwest and L_b of 200 and 3000 m heaved 1 and 2 m, respectively. There is no information regarding other pop ups occurring within this bedrock type. There is one pop up that occurred in limestone with L_b of 750 m and H_b about 1 m. This pop up is directed north-south and bent slightly in its southern portion to the southeast. The smallest recorded pop up in this area occurred in carbonate bedrock with a strike of 140° and L_b of 30 m. Four more pop ups noted in the carbonate bedrock, two of which had strikes of 30°, and the third one oriented in north-northwest. The fourth pop up reported in carbonate bedrock was directed southeast with a L_b of 800 m.

Wallach et al. (1993) studied pop ups as an indicator of locations that are likely

to experience an earthquake. They published a significant number of buckling failures across North America, including 230 cases in New York, Quebec, Ontario, New Brunswick, and Kentucky. The pop ups in these areas occurred dominantly in open fields, with maximum H_b about 2 m, and in quarry floors, with H_b up to 1.5 m. Also, some of the reported cases had occurred in stream valleys or lake bottoms. Within these 230 cases, 66 cases occurred in quarries, 42 cases in open fields, and 85 cases reported that they occurred in open fields and quarries. The bedrock of 35 stream cases in east-central Kentucky was limestone and shale with the dominant buckling orientation of northeast and a median of 50°. Also, 14 cases in this area have a southeast direction, and two cases have north and east orientation. Within these cases, only two stream pop up cases observed at Letchworth Park in New York with a strike of 108°. Among the 66 cases that Wallach et al. (1993) reported in quarries, 51 events were observed in limestone. The dominant strike of seven cases that occurred in Alden, NY, was southeast. The primary orientation of 19 cases has occurred at Aylmer, Beauport, and St-Marc des Carrières in Quebec was southeast. However, the trend of six cases was northeast. Buckling failure in Ontario has occurred at Bells Corners, Coldwater, Cornwall, Milton, Roblin, Roblindale, and Uhtoff. The predominant strike for these quarries directed to the southeast. The buckling failure in dolomite quarries was reported at Hallville and Mt. Nemo in Ontario as well as Gasport and Niagara Falls in New York. The pop ups' trend for eight cases in these areas was southeast, and the rest were oriented to the northeast.

In Balsam Lake area of Ontario, 20 pop ups were reported in carbonate bedrock in

open fields. The predominant trend of buckling ranged from southeast to northwest. The buckling failures in limestone bedrock were reported in Prince Edward County, Belleville, Kingston, and Young's Point in Ontario and Alexandria Bay in New York. The buckling orientation of these 12 open field cases were from southeast to northwest. Also, Wallach et al. (1993) reported three dolomite cases at Burleigh Falls, Charles Lake, and Malcolm Bluff in Ontario with the orientation of 30°, 135°, and 0°, respectively. Three more open field cases occurred at Benjamin's Point, Oakville, and Toronto in Ontario. The first case had occurred in siltstone with the direction of 154°, and the second case which oriented 160° was reported in siltstone and shale. The third case's trend was reported as 63°. The open field pop ups at Chippewa Bay, Oak Point, and Omar in New York occurred in sandstone bedrock and oriented 153°, 140°, and 42°. The only open field case from Miramichi area in New Brunswick occurred in diorite and was oriented at 8°.

Wallach et al. (1993) also reported 85 pop up cases in Western New York State that occurred in quarries and open fields. The bedrock of 50 cases were observed in sandstone and shale, and the dominant pop ups orientation in this bedrock was southeast. However, the buckling trend for 22 cases was northeast. Four cases occurred in sandstone bedrock, three of which were oriented northeast, and one case was oriented southeast. All three cases that occurred in dolomite were directed to the southeast. In this area, two pop ups were observed in limestone: one case in limestone and shale, and one in siltstone which their trends were northeast. The orientation of 15 cases were reported to the southeast. Also, bedrocks of nine cases that trended to

the northeast was not reported. The buckling orientation was mainly southeast with a median of 128°, while 36 cases reported in the northeast direction had a median of 42.5°. The pop ups orientation for the other 16 cases in New York state also was southeast with a median of 140°.

The buckling orientations of all 19 cases in Quebec were mostly southeast, with a median of 110°. However, there were six cases with an orientation to the northeast. In Ontario, buckling trends were predominantly southeast, with a median of 119°. Overall, the predominant buckling orientation of these 230 cases is east-southeast, with a median of 114.5°. Regrettably, there is no record of the buckling dimension for these cases.

Wallach et al. (1994) also reported 13 pop up segments at Deschenes quarry in Ottawa. These segments occurred in six different structures in limestone. Three structures with single segments were reported in the direction of the northeast, with a maximum L_b of 17 m. The other three structures contained two or more segments in a different direction. These segments were oriented southeast within the range of 98° to 172°, and a median of 104°, except two cases with northeast direction. The longest pop up in these three structures was 19 m, and the smallest one was about 3 m.

Thomas et al. (1993) reported 60 buckling cases at the bottom of Western Lake Ontario. All these cases have occurred in a carbonated bedrock. Although the primary orientation of the buckling failure in this area is southeast, there are 22 cases with the direction of northeast. The median orientation in this area is about 103.5°.

Twenty-eight pop up segments that occurred in Quebec were reported by Wallach and Chagnon (1990). Twenty-six of these segments occurred in seventeen buckling structures at Ciment St-Laurent quarry in Beauport. All pop ups occurred in limestone bedrock and heaved between 1 to 2.5 cm, and the median length of the failures was about 20 m. The primary orientation of buckling in this area was northwest, with a median of 325°. However, there are eight cases with northeast orientation.

The latest reported buckling failure was reported by Everitt (2009). Four buckling failures at the Medika Pluton granite quarry in Manitoba occurred in the direction of southeast. The longest pop up was 60 m in length and raised about 1.5 m, and the shortest failure was 1.5 m long and raise less than 0.15 m.

2.4.2 Summary and Analysis of Collected Case Database

The database of buckling event cases collected in this study is published in an online repository (Ghasemi and Corkum, 2020a). An analysis was conducted on the quantitative information available within the database to gain a better understanding of the importance and characteristics of buckling failure events in North America. Overall, 401 reported cases by various authors have been collected in this study, which occurred in 57 areas across North America. These 57 areas were distinguished by their postal code or geographical coordinates obtained using available information in the literature. Among these areas, western New York State and southwestern Ontario host the highest number of pop ups with 85 (21.2% of database entries) and 60 (15%) incidents, respectively. Also, 54 buckling cases (about 13.5%) were pop up segments

that occurred within the same general buckling structures (i.e., multiple measurements per buckling structure/event). The maximum number of segments observed in one structure was five measured segments. Because 90% of buckling incidents reported in the literature occurred in Ontario, Quebec, and New York, these regions are the focus of this study. An overview summary of the database cases is provided in Table 2.3. An important piece of information that was typically unavailable in the collected cases is the mode of failure, or buckling mode associated with each occurrence.

Table 2.3: Buckling cases database summary

Geographic jurisdiction	Number of cases	Number of measurement segments[*]	Case sources
Ontario	208	205	Wallach et al. (1993), White and Russell (1982) Karrow (1993), Lo (1978), Adams (1982), Thomas et al. (1993), Wallach et al. (1994), Crossley (1991), Williams et al. (1985)
Quebec	51	51	Wallach et al. (1993), Wallach and Chagnon (1990), Saull and Williams (1974)
New York	102	101	Wallach et al. (1993), Lo (1978), Wallach et al. (1994)
Manitoba	4	4	Everitt (2009)
Kentucky	35	35	Wallach et al. (1993)
New Brunswick	1	1	Wallach et al. (1993)
Total	401	397	

*Multiple orientation measurements were recorded for some cases where orientation changes along length of buckle.

The location (longitude and latitude) of buckling incidents collected in this study where determined approximately based on the available information. In the literature, the location of the buckling event area was often described approximately, and no report exists to identify the exact location of buckling incidents. Therefore, using

the existing information of these areas, the postal code corresponding to the locations were obtained and/or estimated. The obtained postal code was used to find out the approximate longitude and latitude of the buckling event. The information obtained to locate the buckling incidents from literature included some degree of uncertainty with respect to location data. Therefore, a parameter was created to categorically represent the location data's estimated accuracy and was recorded in the database. These locations were categorized based on the estimated associated uncertainty and were divided into four categories based on the author's judgement: (A) highly accurate, (B) good forecast, (C) reasonable forecast, and (D) inaccurate forecast. Figure 2.7 shows the location of buckling events documented in the database for Ontario, Quebec and New York. Ontario hosts more than 57% of all buckling incidents between these three jurisdictions, and the minimum documented occurrences belong to the Quebec area. An interesting point about the buckling event locations is that most occurrences were located in the border regions between these three areas. This is likely due to natural topographical and geological features related to the geographical borders (e.g., faulting, rivers, lakes). Also, the proximity to high population areas, and thus increased excavation activity, is also a factor in reported buckling events. It is acknowledged that there is undoubtedly an unidentifiable number of undocumented buckling events.

The buckling orientations (α_b) reported for these three areas are dominantly northeast-southwest. Figure 2.8a,b,c show the Rosset plots in Ontario, Quebec and New York, and Figure 2.8d shows the overall orientation of buckling cases. Figure 2.8e shows the stress orientation (β_b) of Ontario for the near-surface region in the upper
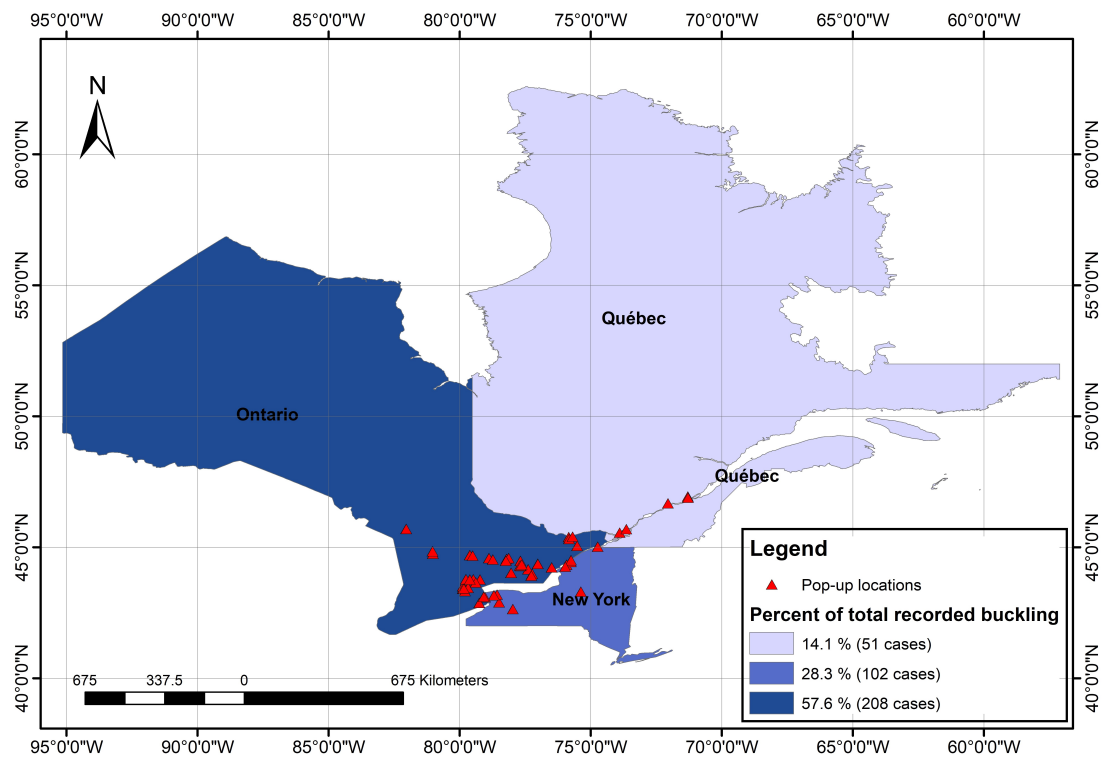
Figure 2.7: Map of Ontario, Quebec and New York showing location of buckling events documented in the buckling database

300 m below ground surface (Kaiser and Maloney, 2005). In this study β_b is the direction of s_H. Figure 2.8f shows the stress orientation (β_b) for Ontario, Quebec and New York from WSM2016. Figure 2.8 shows that the dominant axis strike orientation of buckling cases (α_b) in these areas are almost perpendicular to the direction of s_H orientation β_b. Table 2.4 shows buckling cases α_b versus in situ stress β_b.
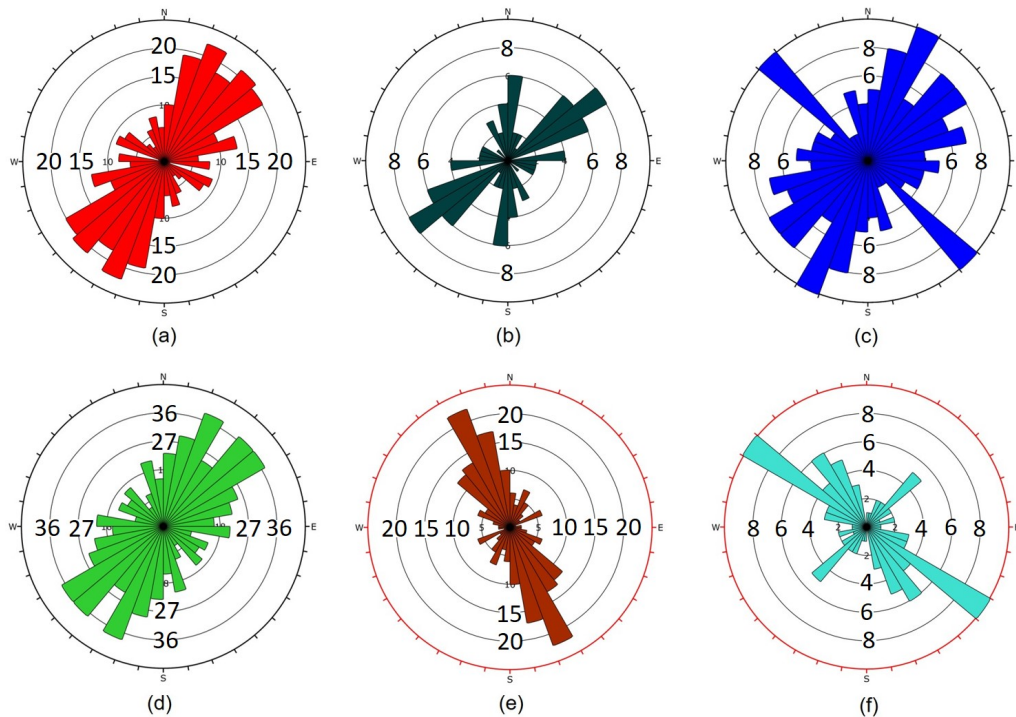
Figure 2.8: Rosette plots showing buckling orientation (direction of buckling) for documented cases observed from literature reports for North America (Ontario, Quebec, and New York) versus the orientation of s_H in the same regions. (a) Ontario; (b) Quebec; (c) New York; (d) Overall (ON, QC, NY); (e) Stress orientation (β_H) of s_H from WSM2016 (ON, QC, NY); (f) Stress orientation (β_H) of s_H from Kaiser and Maloney (2005).

The buckling failures presented in this study, regardless of their geographical locations, have occurred in different location types in terms of land use. Buckles have been reported to have occurred in quarries, open fields, canals, lake bottoms or streams.

Table 2.4: Buckling cases database summary of data

Geographic jurisdiction	Number of cases	Number of buckling orientations*	Predominant orientation	
			Buckling	In situ s_H
Ontario	208	205	NE-SW (135)	NW-SE
Quebec	51	51	NE-SW (135)	NW-SE
New York	102	101	NE-SW (135)	NW-SE

*Multiple orientation measurements were recorded for some cases
where orientation changes along length of buckle.

However, the location type for events that occurred in the western New York State was not distinguished in the literature between open fields and quarries (about 21% of total location types). Figure 2.9 shows specific location types of buckling cases in Ontario, Quebec, and New York, when reported. The data showed that quarries and open fields are the most common areas in Ontario, 35% each, that buckling failure was observed. More than 28% of the pop ups in these areas occurred in lake bottoms and less than 1% were located in canals. In Quebec and New York, these distributions are quite different. In Quebec, all observed cases were found in quarries. In New York, more than 84% of the occurrence were located at either open fields or quarries: in these documented cases, distinction between open fields and quarries was not made. Also, more than 9% were located at quarries and only 2% of incidents occurred within streams or canals. Overall, more than 75% of events occurred in quarries or open fields, whereas at least 35% occurred in quarries.

Buckling events have occurred within a variety of different rock types. Since mechanical behaviour is somewhat different for each type of rock (e.g., soft shale vs stiff dolomite), identifying the type of bedrock that buckling failures have occurred in

(a) Ontario

35.58% Open Field
35.10% Quarry
0.48% Canal
28.85% Lake Bottom

Total =208

(b) New York

9.90% Quarry
3.96% Open Field
0.99% Stream
84.16% Quarries and Open Fields
0.99% Canal

Total =101

(c) Quebec

100.00% Quarry

Total =51

(d) Overall (In North America)

34.41% Quarry
19.70% Open Field
0.50% Canal
9.23% Stream
14.96% Lake Bottom
21.20% Quarries and Open Fields

Total =401
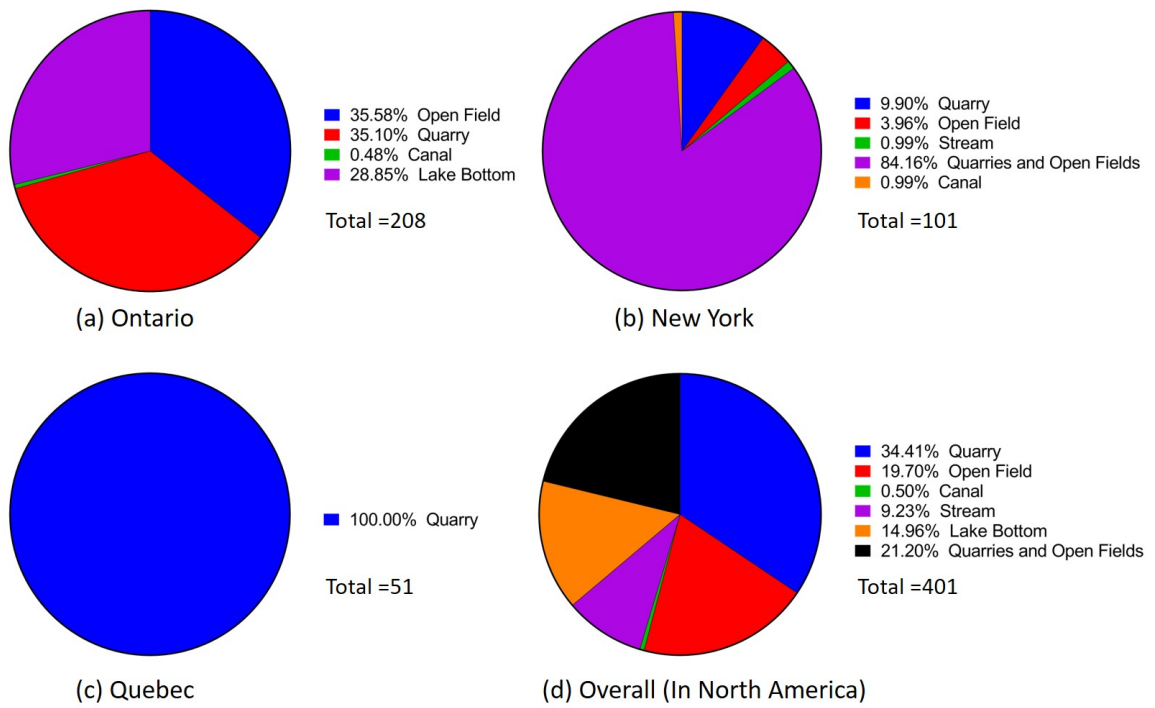
Figure 2.9: Summary of reported location types for buckling cases observed from literature for North America

is critical. In this study, the rock type was collected from literature, when available, at each location. The rock type observed in these areas was limited to dolomite, limestone, siltstone, sandstone, shale, carbonate, diorite and granite. Figure 2.10 shows a summary of rock types for the reported buckling cases. In Ontario, more than 42% of the incidents occurred in carbonate (unspecified type) and more than 33% where specified as limestone. There was insufficient rock type information for about 15% of cases in Ontario. Buckling cases in Quebec mostly occurred in limestone, where more than 94% of cases occurred in this rock type and 4% were documented to occur in dolomite and about 2% in unidentified carbonate rock. In New York state, the variety of rock type was more than the other locations, where eight rock types associated with buckling events were reported. The most common rock type where buckling occurred in this area was shale and sandstone, which accounted for about 50% of the documented events. There is no rock type report for about 24% of cases in New York.

Overall, the dominant bedrocks where documented buckling events occurred in North America are limestone and undifferentiated carbonates with 32% and 22%, respectively. For 14% (57 cases) of cases no rock type data was available.

Dimensions of buckling events, such as length, width, thickness and height was also collected for the database. Unfortunately, this data was only available for about 15% of cases. Table 2.5 provides a summary of the maximum and minimum length and height of the buckling cases reported in the literature. There is no record of both buckling height and length for any buckling cases from New York. In Ontario, the
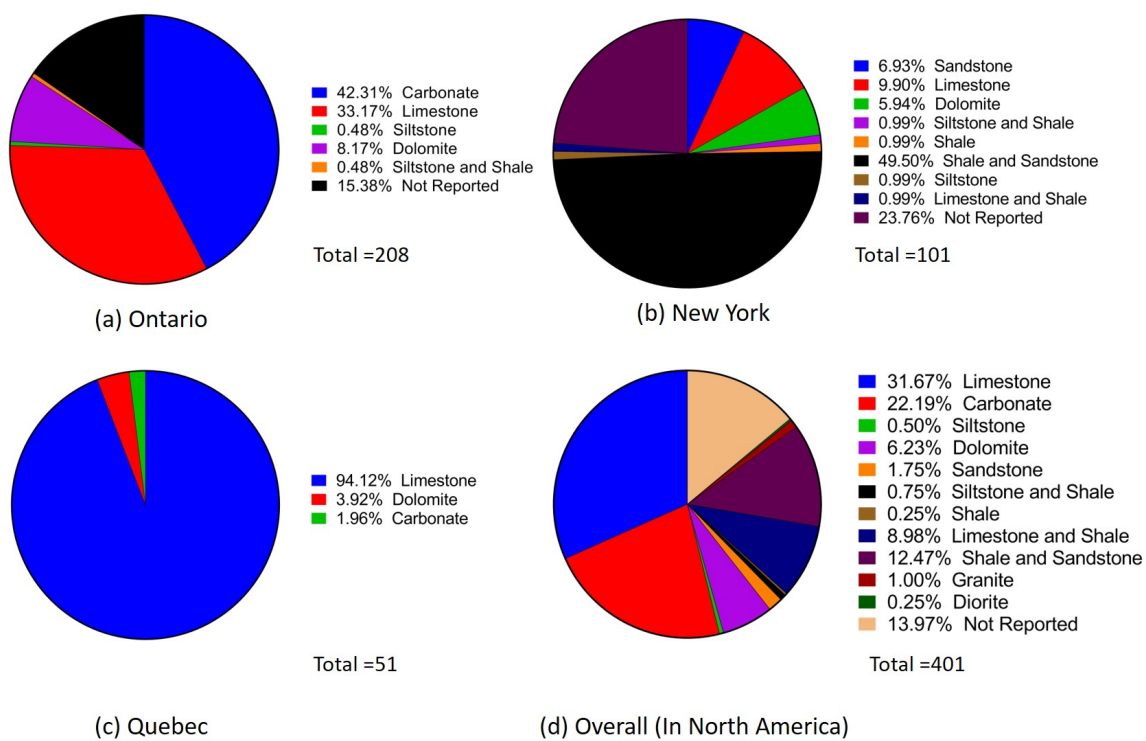
Figure 2.10: Summary of rock type for buckling cases observed in North America

maximum reported buckling length was 3 km, and the minimum recorded buckling length was 1.5 m. For Quebec, the maximum buckling length was about 100 m, and the minimum buckling length reported was 2 m. The maximum heave reported in both Ontario and Quebec areas was 1.5 m. The minimum heave in Ontario was 0.3 m, while in Quebec, the minimum reported heave was about a centimeter.

Table 2.5: Buckling cases database summary of data

Geographic jurisdiction	Cases	L_b Max[a] (m)	L_b Min[a] (m)	H_b Max[b] (m)	H_b Min[b] (m)
Ontario	208	3000	1.5	1.5	0.3
Quebec	51	100	2	1.5	0.01-0.025
New York[*]	102	-	-	-	-

[a] Number of cases with recorded buckling length is 23 and 32 for ON and QC respectively.
[b] Number of cases with recorded buckling height is 14 and 32 for ON and QC respectively.
[*] There is no recorded buckling length and height for NY.

The collected database basic data analysis revealed useful trends in orientations, especially relative to the predominant in situ stress orientation, and an understanding of the range and typical dimensions of buckling events. In addition, the locations where buckling occurred most commonly and the associated rock types were revealed. It is unfortunate that so many events were inadequately documented or quantified. Hopefully, this can be improved going forward for the benefit of public and environmental safety, and aggregate/mining operations.

2.5 An Overview of Common Buckling Mechanisms and Analysis Methods

The collected cases in the surface buckling database provide examples of many different buckling conditions: rock type and rock structure, in situ stress conditions, buckle dimensions, and buckling modes. One of the challenges with prediction of buckling occurrence in rock is the variation in observed buckling modes. There are numerous mechanisms and conditions associated with observed buckling events. Thus it is not possible to develop an analysis procedure suitable to address all potential situations. In addition, the variability and uncertainty associated with geological, geotechnical and hydrogeological conditions presents additional challenges to analysis and stability assessment. Several analysis methods exist that are applicable to certain well-constrained buckling mechanisms and these approaches are presented here. Fig 2.11 summarizes and categorizes the main classes and modes of buckling failure observed within the database.

2.5.1 Buckling within Massive Rock Units

Buckling features have been observed in massive, intact, unjointed or unlaminated rock units and is often referred to as rock 'exfoliation.' The formation and propagation of sheet-like structures parallel to the ground surface topography is a well-known phenomenon. These fractures tend to occur in regions of high s_H within massive brittle rock such as granite and often involve topographical features such as domes or hillsides. The failure mechanism is akin to brittle spalling where tensile fractures
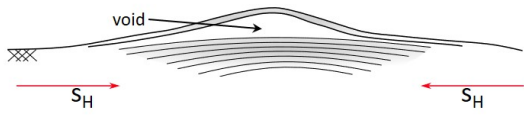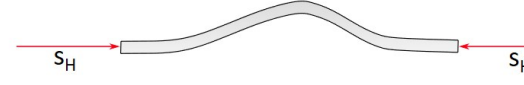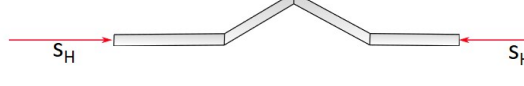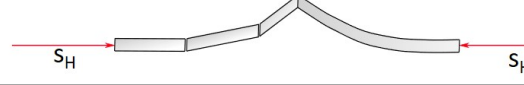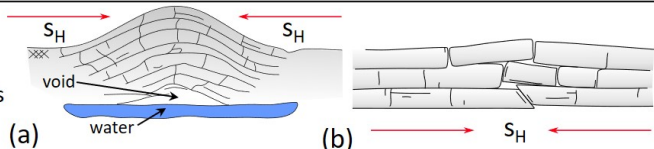
Buckling class	Buckling mode	Typical examples
Massive rock buckling (MRB)	Brittle fracture formation and exfoliation (EXB)	
Single layer buckling (SLB)	Euler-like buckling (EUB)	
	Three hinge buckling (THB)	
	Blocky SLB (BSLB)	
Multi-layer buckling (MLB)	Complex and may consist of sub-modes	

Figure 2.11: Buckling failure mode summary and classification chart based on failure modes observed in the field.

form in an overall compressive stress environment forming long, slab-like features that extend in the maximum principal stress direction. Once these fractures have formed, they create laminated surface features or an open, surface-parallel discontinuity. Under high stress, these features can begin to buckle forming what is sometimes referred to as a rock 'blister.' The process can sometimes continue to advance until a full buckle of the detached rock slab develops. The mechanism can be progressive forming subsequent fractures parallel to the initial, ground-surface parallel feature. This mode of failure is referred to here as exfoliation buckling (EXB). Figure 2.12 shows an example of an exfoliation feature with some minor buckling developing. Other well-known examples of exfoliation features can be observed at Yosemite park and other locations where they sometimes form 'exfoliation domes,' such as the Twain

Harte Dome. These features have also been attributed to thermal loading (cyclic), ice jacking freeze thaw cycles, chemical weathering (oxidation) and the release of 'locked-in' residual stress (Holzhausen and Johnson, 1979; Savage, 1978).

Figure 2.12: Exfoliation, arching, or 'blister' of a thin layer of granite, Hyden Rock, Yilgarn Canyon, Western Australia (Twidale and Bourne, 2009)

Brittle failure mechanisms in rock has been a focus of attention for rock engineering researchers for many decades. Predicting the onset of brittle spalling, and in the extreme, rock bursting, is an important safety and operations issue for underground mining. This topic has received much less attention with respect to near-surface engineering projects. The formation and propagation of brittle spalling fractures has been associated with the crack initiation threshold (σ_{ci}) observed in laboratory

compression testing (Martin et al., 1997). This threshold typically corresponds to a compressive stress level (deviatoric: $\sigma_1 - \sigma_3$) somewhere between 1/3 and 2/3 of σ_c (Hoek and Martin, 2014).

Currently, the primary means of evaluating brittle failure potential is by comparing elastic stress analysis predictions obtained from continuum numerical modelling to σ_{ci}. An example of this approach for underground excavation is presented by Martin and Christiansson (2009). Diederichs (2007) and Perras and Diederichs (2016) proposed a novel modification to the Hoek-Brown failure envelope using continuum numerical modelling to capture this phenomenon. Other more sophisticated analysis methods have also been developed using both continuum and discontinuum (e.g., PFC (Itasca, 2018) and $UDEC$ (Itasca, 2014) tessellated modelling) numerical modelling. However, these advanced analysis methods have not been applied to near-surface excavations. Because exfoliation features are often associated with unloading while maintaining high s_H, an analysis approach suitable for this mechanism would require using a brittle failure criterion and may also require an analysis method that incorporates the release of residual stress and its associated latent strain energy.

2.5.2 Buckling of a Single Rock Layer

The majority of observed buckling cases occur in rocks with pre-existing weak planes parallel to the ground surface, such as sedimentary rock bedding planes, in particular within limestone and dolomite formations. This section will discuss buckling within a single layer or lamina and will be referred to as 'single layer buckling' (SLB). Although

the focus is on a single layer, this could also include cases where several layers are tightly connected (e.g., fully-intact bedding) and buckling occurs along a discrete weak contact as if the buckling stratum acts as a single beam or layer of blocks from a mechanical perspective.

Classical buckling, or Euler buckling (EUB), of a beam or plate within a single layer is the most well-known form of buckling in engineering. However, this form of buckling is rarely observed in a rock stratum. This buckling mode requires that the buckling material is, or behaves as, a continuous beam or plate *throughout* the buckling process. The effects (i.e., resisting strength) of the contact discontinuity between the buckling surface layer and underlying material is considered negligible and the beam bends while remaining in an intact continuum. This means that both compressive and tensile beam stresses are maintained within the beam without significant disruption due to the presence of either pre-existing sub-vertical discontinuities (e.g., cross bedding) or the formation of beam-bending-induced tension cracks. It should be noted that this buckling mode also has several sub-modes depending on the beam's loading and boundary (i.e., end) conditions. Once the buckling beam is influenced by sub-vertical fractures, whether naturally occurring or bending-induced cracking, classical EUB is no longer applicable. Instead a buckling mode that includes the effects of multiple blocks within a single layer applies. These single layer block buckling modes can include two or more blocks of various sizes. These multi-block modes are discussed in a later section.

Euler Buckling Analysis

Cavers (1981) proposed using Euler's method to analyze the flexural buckling modes of

failure in slopes considering some assumptions and simplifications. In this method, an

elastic, weightless, and straight column (slab) were considered that obeys Hooke's law.

Since in Euler's theory, the slab is considered weightless, half of the buckling length's

weight is added to the driving force of buckling. This assumption is conservative,

because during buckling a part of the slab resistance force is an element of the slab's

weight. Based on the Euler's methods, the critical load per unit width of a rock beam,

(P_{cr}/b) , is calculated with the following equation.

$$\frac{P_{cr}}{b} = \frac{K_e \pi^2 EI}{b \, l_b^2} \tag{2.5}$$

The critical load is the maximum load before buckling failure. Where K_e is an

end condition constant with $K_e = 1$ for pinned ends. I is the moment of inertia, l_b

describe the buckled slope length, P_{cr} is the critical load in flexural buckling, E is the

Young's modulus, b is the slope width, and d is the slab thickness. The moment of

inertia for a rectangular solid in equation 5 is:

$$I = \frac{bd^3}{12} \tag{2.6}$$

Also, Cavers stated that using this equation in slopes requires another assumption

that needs to be considered which is the l_b/l ratio of buckled slope length to the total

slope length. This ratio varies depending on the condition and material used i.e., for

rock, this ratio is 0.5. Although this type of failure is essentially a theoretical mode, it rarely occurs geologically because of the presence of pre-existing or induced fractures within the rock column during buckling. Buckling of a continuous rock beam in an Euler-like mode or other similar flexural modes is not considered a likely scenario in typical horizontal configurations, such as a quarry floor. Based on the database of buckling events, none of the documented events appear to match this mode of failure, although it is possible that some events began as an Euler-like buckling mode prior to changing with increased upward displacement and progression of the buckle.

Three Hinge Buckling

Three hinge buckling (THB) has been described for rock slopes by Cavers (1981). This buckling mode consists of buckling of two rock blocks driven by s_H. This configuration requires crushing in the central zone and two lateral hinge zones to allow for kinematic freedom for the buckle to fully develop. THB is an idealized and simplified failure mode that lends itself to analysis. This mode, or similar variations of this mode, have been documented in the buckling events database and also in slopes.

The THB, or similar modes have been studied extensively in masonry construction. An analysis method was proposed by McDowell et al. (1956) who generated static load-deformation curves of masonry beams using the 'Arching Action' theory on masonry walls considering a beam clamped at both ends. They highlighted the failure process in the following steps: First, tension cracks growth at the ends and

center of the span upon the start of loading. These cracks then expand to the centerline of the beam. During the failure process, it is assumed that both beams stay rigid and rotate at the end and center. Crushing of the masonry materials at the ends and center forms a force couple in these areas. The rotation will stop if the couple forces disappear, or the load is removed, and the wall will collapse in both cases. Dawe and Seah (1989) also studied the effects of some design parameters on masonry infilled panels and analyzed post-cracking behaviour as the buckling mode fully develops. These masonry analysis examples are both fairly similar to the THB mode of failure in rock.

For cases related to underground mining (e.g., roof stability), Sterling (1980) conducted laboratory physical modelling of a thick rock section buckling in a THB configuration. Buckling in the underground mining environment was also extensively reviewed by Diederichs and Kaiser (1999). The authors described independent layers each bending under a combination of lateral abutment loading and gravity loading (i.e., self-weight). They presented several modes of instability: snap through, crushing failure, abutment shear failure, and diagonal fracturing. These were partially based on observations from the physical modelling laboratory program by Sterling (1980). Because these modes for underground conditions are significantly influenced by gravity, many do not directly apply to quarry floor stability where gravity resists upward buckling. In quarry floors abutment shear failure is not a realistic mode nor is buckling due to relaxation of abutments because of lack of gravity-driven destabilizing forces. Diagonal fracturing was only observed in relatively thick blocks and is

not considered further because few, if any of the database buckling events included intra-block failure of rock. Diederichs and Kaiser (1999) presented a revised approach to the voussoir arch analogue for stability of rock beams in roof and walls of underground excavations. They identified a critical deflection limit for buckling suggesting that buckling will fully-develop to collapse after deflection of the apex of the buckling beam displaces by 1/10 of the beam thickness (T_b).

Buckling of a Single Layer in a Blocky System

A method to analyze buckling behaviour for bedded sedimentary rocks in Southern Ontario was developed by Roorda et al. (1982). The method is based on two-dimensional conditions, but the method was extended for three-dimensional conditions by Roorda (1995) for buckling of a plate. However, observed failures typically resemble the two-dimensional case more than a three-dimensional plate-like buckle. The method divides the rock stratum into three segments: two unbuckled sections at either end and a buckled centre section. The lateral unbuckled sections account for bed slippage at the base of the rock stratum that provides the driving forces for buckling of the central buckling section. The method assumes no internal joint slippage and treats the entire buckling beam (bed or buffer) thickness (referred to as 'layer thickness') as a continuous beam. The method considers stiffness of the rock unit, shear strength of the bedding plan (basal failure), and weight of overlying rock and overburden. Using the input parameters, the method can provide a critical in situ horizontal stress component for the onset of potential buckling (s_{cr}); the post-buckled

stress; the length of the buckled zone; and the vertical and horizontal displacement of the buckled section.

The method can consider a variety of buckling sub-modes, classified by Roorda as: smooth arch; smooth gable; simple gable; complex modes. The buckling moves progressively through the stages from smoother arch through the more complex modes; however, each stage in the progression does not necessarily occur. As the stratum flexes, inducing tensile stress into the buckling stratum that the jointed rock mass cannot maintain, the smooth arch breaks along existing flaws (e.g., cross-joints) evolving into more complex buckling modes such as a gable shape. Using energy methods, solutions were provided for each of the sub-modes/shapes and the worst-case scenario is considered suitable for design purposes. A set of general equations were presented for analysis, along with a series of input factors for each of the buckling conditions.

Based on the method, an extremely high stress level is required to induce a classic smooth beam buckle into the stratum. Therefore, the method recognizes that a 'displacement trigger' of some type is required to induce buckling such as rapid removal of overlying bedrock, blasting, water pressure, etc. Once s_H exceed s_{cr}, indicating that the potential for buckling exists, there are two possible outcomes: firstly, if the displacement trigger *does not* occur, the stratum achieves a final unbuckled equilibrium; and secondly, if the displacement trigger *does* occur, the stratum buckles and the associated stress relief is achieved.

The equations for both states are combined as a piece-wise buckling potential envelope as a single curve. The mathematical development of this method is fairly

extensive and is therefore not included here but can be found in the original publications (Roorda et al., 1982; Roorda, 1995). The division between stable and (potential) unstable conditions, occurs at s_{cr}. The upper branch of the curve (deformed equilibrium state) represents the final unbuckled equilibrium, while the lower portion of the curve represents the buckled condition. If the displacement trigger occurs, a sudden buckling failure is predicted as the final stresses move from the 'unbuckled equilibrium' to the 'buckled equilibrium' state. The stress within the layer (stress at equilibrium) is much lower for the buckled than the unbuckled state, consistent with the stress-relief nature of the phenomenon.

2.5.3   Buckling of a Multi-Layer Rock Sequence

Although the most commonly documented buckling failure modes in the buckling event database involve a single layer (SLB) or lamina, multi-layer buckling (MLB) has also been observed. MLB is a complex failure mode typically involving multiple layers and multiple blocks acting independently in a non-symmetrical configuration. Block size can vary as well as the thickness of the different layers, and even the rock type (e.g., interbedded shale and siltstone). Because of the total thickness of MLB zones, there exists greater potential of the failure zone intersecting an underlying aquifer resulting in hydraulic connection between the aquifer and the excavation surface. Also, this mode is not necessarily as reliant on stiffness of the unit to build up buckling-inducing stress, but can also involve softening and time-dependent (i.e., viscous) behaviour of the rock unit and is therefore more dependent on strength of

the rock mass than other modes.

MLB can occur over a wide range of scales from large-scale metamorphic process to the smaller-scaled, localized features discussed here. Fabbi and Smeraglia (2019) discuss large-scale pop up structures in fold-thrust belts within sedimentary sequences in the Apennines mountain belt. Davis (2019) discusses spectacularly folded limestone and mudstone layers found in the Peloponnese, Greece. These large-scale metamorphic processes occur over geological time-scales and, although they provide valuable insight into buckling of rock units, these processes are not the focus of this study. This study focuses on MLB occurrences that can occur relatively quickly in the scale of human activities, such as quarry and mine excavation.

Two examples of MLB are shown in Figure 2.13. Both of these examples occurred in sedimentary rock in Ontario and where mapped in detail to scale in excavations where they were carefully exposed. Figure 2.13a was mapped from a quarry floor excavation and is an example of MLB in a fairly stiff dolomite sequence. This buckling zone is approximately 3 m thick. Figure 2.13b was mapped in the Toronto Union Station construction excavation and comprises a complex sequence of sedimentary rocks of different types with a buckling zone approximately 4 m thick.

The potential trigger mechanisms associated with MLB may be similar to other buckling modes, such as stress changes due to excavation, ground motion (e.g., blasting), but can also include changes to rock properties such as the formation of new fractures, separation of bedding planes, or weathering (i.e., softening and weakening) of the formation locally.
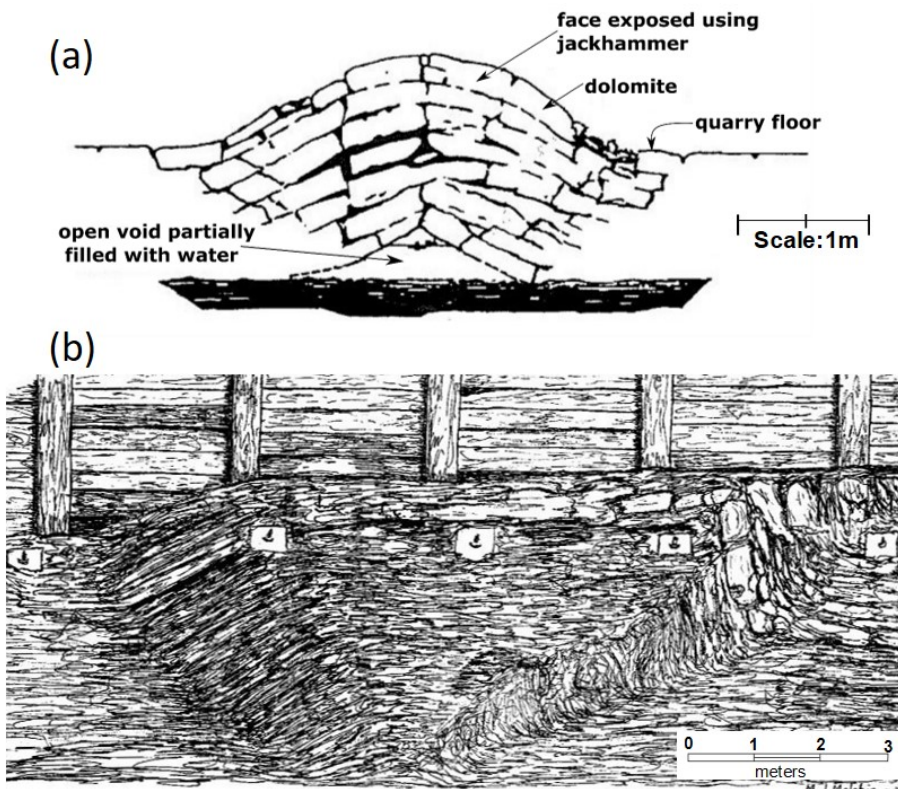
Figure 2.13: Examples of complex-mode, multi-block buckling failures drawn to scale. (a) A pop up mapped from a quarry floor excavation in Ontario. (Modified after Roorda (1995)); (b) A buckling case located in the excavation for Union Station, Toronto, Ontario. (Modified after White and Russell (1982))

Non-symmetrical SLB and MLB modes are likely not possible to evaluate using analytical methods. Numerical modelling methods provide a means to simulate these complex modes. Several studies have utilized numerical modelling to simulate buckling, such as Diederichs (2007); Karampinos et al. (2015), using distinct element codes UDEC and 3DEC, respectively. Although these models are able to capture inter-block (i.e., between blocks) behaviour in a complex system, they were not able to capture intra-block (i.e., within blocks) failure of intact brittle rock. These models can use elasto-plastic models for intact rock, similar to continuum models, however, it has been shown that intact brittle rock is not well represented by such simplified models Hoek and Martin (2014). To capture these complex buckling modes models would need to account for stress and deformation behaviour as the failure mechanism advances progressively, the inter-block interface behaviour, and intra-block failure/fracture formation of intact rock. Models capable of capturing this behaviour exist, such as UDEC/3DEC grain-based models (Gao et al., 2016; Garza-Cruz et al., 2014), PFC2D/3D (Potyondy and Cundall, 2004), ELFEN (Stead et al., 2006; Karami and Stead, 2008), IRAZU (Mahabadi et al., 2016) and others. In most cases, capturing the complex block interaction and inter- and intra-block rock fracturing and behaviour would require tremendous computational resources even for a well-defined back-analysis of a documented case. Moreover, the challenge with such sophisticated modes is the need for careful model calibration which requires detailed rock mechanics, and sometimes hydrogeological, site characterization. In addition, the in situ

stress (s_H) is a critical input that is challenging and costly to obtain. For prediction purposes, characterizing conditions over a large area means we are inevitably always utilizing a data limited system (Starfield and Cundall, 1988). Moreover, time-dependent process, such as bedding delamination are extremely difficult, if at all possible to capture within the context of any analysis. However, advances in this area may lead to improved field assessment. For example, Guerin et al. (2019) present a means to evaluate the continuity of rock bridges using thermal imaging which may provide useful insight into time-dependent buckling potential.

2.6   Conclusion

The buckling stability of quarry floors has become of greater interest over the past decade. There has been significant evidence of buckling failures in various conditions and expressed in various buckling failure modes. In particular, in the region of the North America Craton where high horizontal in situ stresses exist, numerous cases have been observed. A first step in understanding the likelihood of buckling event occurrence under various conditions requires a thorough compilation of past observed in situ buckling events. This study collected documented cases of spontaneous, near-surface buckling events under wide ranging conditions. The database includes information on geological conditions, buckling dimensions and in situ stress, when available.

The cases of buckling events where mapped geographically and compared to reported in situ stress databases of the region to quantify the relation between buckling

events and s_H magnitude. In addition, the relation between the dominant s_H orientation (β_b) and the direction of buckling (α_b) was explored and showed a clear overall correlation throughout the region. The collected data showed that quarries and open fields are the most common areas in North America where buckling failure has been observed, in which at least 35% of the occurrences were in quarries. Furthermore, dominant bedrock types where buckling events have occurred were limestone and undifferentiated carbonates. It was noted that only 15% of total cases reported associated dimensions of buckling events. Although the paucity of dimension data highlighted a data collection need in documenting buckling events, the collected data provided insight into the typical range of buckling dimensions, which could be helpful in risk assessment.

A review of buckling mechanisms applicable to near-surface conditions was presented along with a brief overview of existing stability analysis method. Although it is clear that buckling failure is complex, it may be possible to classify failures into buckling modes as presented in the study. As with analysis for rock slope stability and underground excavations, identification of failure mode is a key step in developing a rational analysis approach. A near-surface buckling mode classification was developed and presented based on typical documented cases.

Analysis and prediction of buckling occurrence seems a daunting task. The difficulty in site characterization such as rock mass conditions, geological conditions, analysis parameters and, in situ stress measurement are a major challenge for assessment of buckling potential. Moreover, the limitation in analysis methods and

computer modelling requirements (e.g., parameter and model validation and computational resources) are not currently able to address more than relatively simple cases at this time. Due to these limitations, it is likely that some types of risk assessment approach (i.e., risk map) would be suitable to assess buckling potential and buckling risk for rock engineering projects. Such an assessment must be based on a rational framework of analysis methods. As a first step to gaining suitable insight into buckling modes, Ghasemi and Corkum (2020b) have developed a test apparatus to simulate THB under controlled and carefully monitored conditions. Although this is one of the simplest buckling modes, understanding the response of rock under these conditions is a useful starting point in understanding more complex modes.

Carefully documenting future buckling events and adding them to the online database available to researchers and engineering practitioners that include greater details than currently-documented cases presented in this study (e.g., mode of failure, rock type, and detailed dimensions) would be a significant step towards improving our understanding of buckling potential in the near-surface environment.

Declarations

Acknowledgements

Funding Sources

Conflicts of interest/Competing interests

The authors declare that they have no conflict of interest with respect to this study and this publication.

Availability of data and material

The database of collected ground surface rock buckling case studies has been uploaded to an online data repository for data transparency. The database can be found at: Ghasemi, M and Corkum, AG (2020), "Ground surface rock buckling cases," Mendeley Data, v3http://dx.doi.org/10.17632/yh6cfhpjd7.3

Chapter 3

A Three Hinge Buckling Laboratory Test

M. Ghasemi, A.G. Corkum

Manuscript published to *Rock Mechanics and Rock Engineering Journal*

3.1   Abstract

Near-surface buckling of horizontally laminated sedimentary rock has been reported

to occur in Ontario, Canada and the Upper Midwestern U.S. where high horizontal

in situ stresses occur. Often referred to as 'pop ups', these buckling events typically

occur suddenly and are commonly accompanied by a rapid energy release akin to

rock bursting. In recent years, this mode of instability has become a concern for

surface mining and quarry operations, in particular in cases where the buckling failure

creates a connection between an underlying aquifer and the excavation. Despite

previous research on the topic of buckling instability, there remains many limitations

in development of a design methodology to account for buckling failure. The main

objective of this research study is to experimentally investigate a simple buckling

failure mode, known as three hinge buckling (THB): buckling that involves rotation

of a two-rock block configuration with a central hinge. An experimental testing

procedure was developed to reproduce THB at laboratory scale, including the design

and fabrication of a new testing apparatus and development of a testing methodology. A preliminary THB test was conducted and the results are presented. A simplified, elastic block numerical model was developed using the distinct element method code *3DEC* in order to provide insight into the laboratory experiment. Overall, this newly-developed test was able to reproduce the THB failure experimentally in the laboratory and to provide an opportunity to observe the brittle buckling failure in order to obtain valuable, quantifiable information about the failure process.

3.2 Introduction

The occurrence of spontaneous buckling failures have been observed in the sedimentary rock sequences of Ontario and Quebec, Canada and the Upper Midwestern U.S. These buckling failures occur in regions of high horizontal in situ stress ($\bar{\sigma}_H$) and occur relatively rapidly with little warning. Sometimes referred to as 'pop ups', these buckling events typically occur suddenly and are commonly accompanied by a rapid energy release akin to rock bursting. Some type of 'trigger' mechanism, such as blast vibrations or water pressure, is thought to often initiate these failure events. An example of a pop up, mapped in detail from a road cut in Ontario, is shown in Figure 3.1. This buckling failure involves a complex interaction of numerous rock blocks and multiple layers of the sedimentary rock sequence. The water observed at the base of the failure zone shown in the figure may have influenced or triggered the failure. Other examples of similar buckling failures have been reported by Adams (1982); Roorda et al. (1982); Wallach et al. (1993).
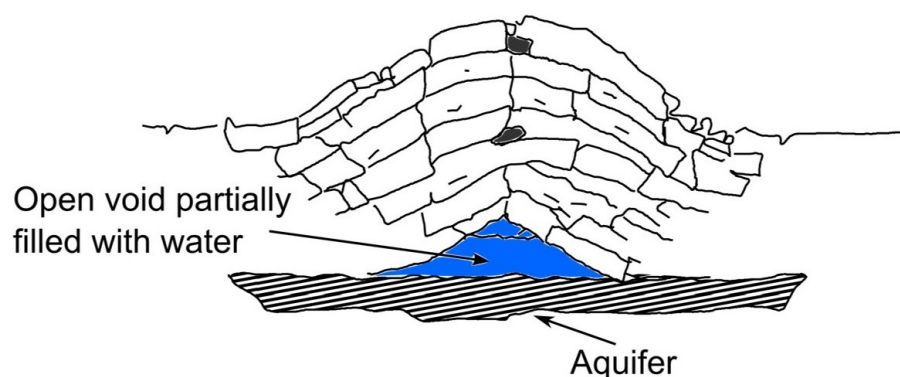
Figure 3.1: Section through a multilayered pop up mapped in a road cut in Ontario, Canada. Modified after Roorda (1995)

In recent years, buckling instability has become a concern for surface mining

and quarrying operations, in particular in cases where the buckling failure creates a hydraulic connection between an underlying aquifer and the excavation. This can result in operational issues (e.g., flooding) and also detrimental environmental impacts (e.g., aquifer and water wells). Therefore, design of pits and quarries that account for this instability mode is becoming increasingly important.

Rock buckling has been studied by numerous authors, such as Adams (1982); Roorda et al. (1982); White and Russell (1982); Roorda (1995), who studied buckling instability in quarry environments. Buckling related to underground excavations have been presented by Sofianos (1996); Diederichs and Kaiser (1999) for mine stopes and by Boon (2019) for roof support of a cavern in horizontally bedded sedimentary rock. Buckling for slopes has been discussed by Cavers (1981); Tommasi et al. (2009); Martin et al. (1997), and for masonry structures as discussed by McDowell et al. (1956) and Dawe and Seah (1989). Despite this past work, there remain many limitations to development of reliable analysis methods and currently no established design methodology (e.g., limit equilibrium method) to account for buckling failure in excavation floors exists.

Some pop up buckling cases involve softening of the rock (in particular for shales), exfoliation and brittle fracture, buckling of multiple blocks, and other complex mechanisms and combinations of these mechanisms. There is little hope that a simple laboratory experiment or analytical analysis method can adequately address all of these complex modes of failure and provide a suitable design basis. However, there is a realistic possibility that development of advanced numerical modelling techniques

may be able to capture much of the complex behaviour. For example, codes such as *PFC* (Itasca, 2018), *UDEC* (Itasca, 2014) with a Voronoi tesselated grain-based model (*UDEC-GBM*) and the recently-developed *3DEC* bonded block model (*3DEC-BBM*) (Garza-Cruz et al., 2014) show promise as a means of capturing this complex behaviour. Development of such sophisticated numerical models requires careful calibration and verification in order to capture the evolution of failure. A carefully controlled and monitored laboratory study would be an important contribution to analysis and modelling developments.

The classic Euler buckling failure mode that occurs in slender beams and columns is an unlikely dominant failure mode for these quarry rocks under typical conditions. The presence of cross bedded structures and other discontinuities in the rock mass allow for non-Euler buckling modes to occur at lower stress levels than would be required for Euler buckling. A simple buckling failure mode known as three hinge buckling (THB) has been described by Cavers (1981) for rock slopes. THB is a relatively common buckling mode observed in quarry floors. This mode involves rotation of a two-rock block configuration with a central hinge, or fulcrum, at the centre of the two blocks. Two lateral hinges occur at the outside block interfaces. Kinematically, this mode of buckling requires fracturing of the block corners at the hinge locations, referred to as 'crushing zones.' A conceptual sketch of the THB mode for a quarry condition is shown in Figure 3.2.

Although THB is a very specific and simplified buckling mechanism, it is an important first step in clearly understanding this failure mode prior to considering
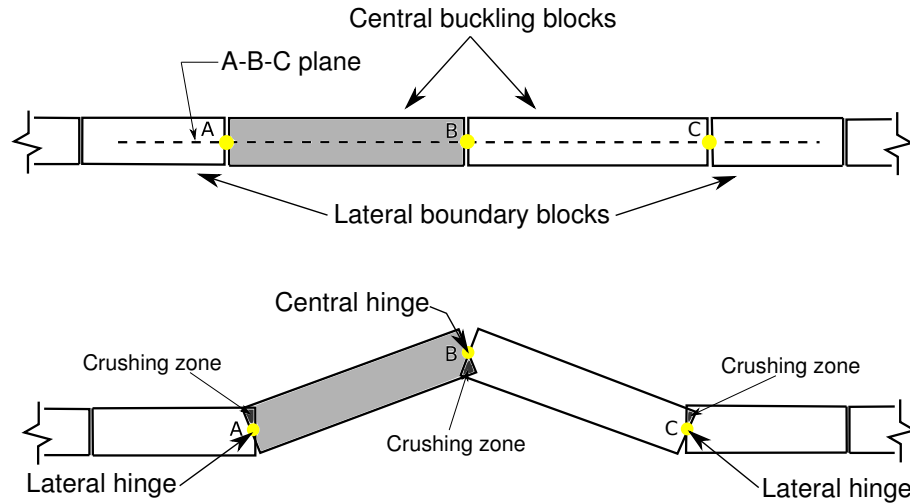
Figure 3.2: Conceptual illustration of the simple three hinge buckling (THB) mechanism. Crushing zones at each of the three hinge points are kinematically necessary for the failure to occur. (Exaggerated for clarity)

more complex, multi-block buckling modes. Some important questions that could be addressed with a full understanding of this mode are: What strength parameters are most critical in the crushing zone?; How does block geometry (block length, L and thickness, T) impact failure?; What is the role of the instability-driving stress ($\bar{\sigma}_H$)?; What is the nature and role of destabilizing trigger mechanisms (e.g., water pressure and blasting vibrations)? In addition to these THB-specific questions, issues related to more complex failure modes, and the statistical distribution of geological structures and rock properties at a given site will also require further consideration beyond the scope of a THB-focused study.

This paper presents the development of a unique laboratory testing apparatus and methodology to simulate THB under controlled, and carefully monitored experimental conditions. The test is somewhat similar to the well-known three- and four-point bending tests (ASTM C1609/C1609M-12, 12) conducted on a beam (single block),

but in this case the test is modified to produce controlled THB on a symmetrical configuration of two rock blocks under a constant load (stress) analogous to the field conditions of a rock bed under constant horizontal in situ stress.

3.3   Apparatus Design and Experimental Setup

A new experimental setup was designed to simulate a simple THB configuration at laboratory scale. The objective of the test is to capture the relatively-violent THB failure behaviour in a controlled manner that reasonably matches the in situ conditions. The test is conducted on two rock blocks with boundary conditions that simulate the high in situ 'clamping' stress. A trigger mechanism that acts to initiate the buckling failure is also incorporated. The test system is carefully instrumented and monitored in order to extract meaningful data from the test. The test apparatus and methodology have been developed using an iterative process with a series of initial developmental tests conducted on concrete block specimens with continued improvements and refinements until arriving at a suitable configuration. A preliminary test on rock block specimens was then conducted.

A particular challenge is the configuration of test boundary conditions. In situ, rock blocks involved in the failure are held in place by adjacent blocks under in situ stress and it is debatable if this condition is best replicated experimentally as a constant stress or constant displacement boundary condition. The reality is likely often somewhere between these two boundary states and experimental boundary conditions

were imposed that reasonably replicate this condition while allowing for clear test interpretation and relative ease of experimental setup. In order to make best use of existing laboratory apparatus, the test was aligned in the vertical direction (as opposed to the in situ horizontal orientation) with blocks stacked on top of one another with buckling induced outwards in a horizontal direction (as opposed to upwards in the in situ orientation). The two rectangular block specimens with dimensions of length (L), width (W), and thickness (T), and a ratio of the block length to the thickness (L/T) are utilized in the test. The axial (vertical) load (P_a) and lateral trigger load (P_l) are applied to the block boundaries during testing. The conceptual test block configuration is shown in Figure 3.3.
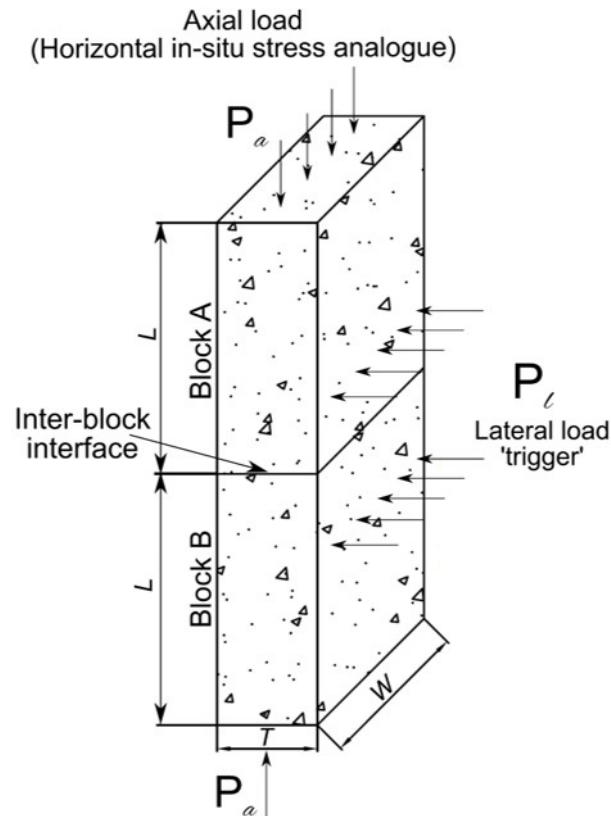
Figure 3.3: Geometry of the test block setup used for the simple THB test

A constant load is applied axially to blocks (P_a) consistent with the target horizontal in situ stress of interest. P_a is applied through a spherically-seated upper platen in order to ensure a uniform load application. However, buckling of the sample with a fixed lower platen and an upper platen free to rotate would make interpretation of the test results difficult and would be dissimilar to field conditions. Therefore, once the test blocks are equalibrated under P_a, the upper platen is immobilized from rotation by inserting a steel shim (wedge or key) into the platen's spherical-seating mechanism. Buckling will then occur under constant vertical load against platens fixed with respect to rotation. With the specimens in the vertically-aligned load frame, the buckling failure is initiated with the application of a horizontal load applied to the test block faces, referred to as lateral load (P_l). As mentioned previously, the buckling trigger in the field is not always known or well understood, but this relatively simplistic failure initiation mechanism results in a relatively easy way to interpret loading condition for the laboratory test.

In order to produce the test configuration and conditions described above, a THB testing apparatus was developed that could be attached to a conventional vertically-oriented hydraulic load frame. The apparatus design is shown in Figure 3.4. The boundary conditions and loading sequence is shown in Figure 3.5. A 2 MN-capacity load frame was utilized (Instron UTM-HYD Model 5596-E2-F4-G1). Given that axial loading is a small fraction of the frame's capacity, the system is considered 'stiff' for the purposes of these experiments. An L-shaped steel frame ('L-frame') was fabricated to provide a horizontal base platen and a vertical mounting surface for the horizontal

load actuator (see Figure 3.6). The THB test apparatus was installed onto the load

frame and fixed in-place by bolting directly onto the load frame as shown in Figure 3.7.

A 45 kN-capacity hydraulic jack was attached to the vertical face of the L-frame in

line with a 250 kN-capacity load cell to measure the applied lateral load. A loading

arm was fabricated and attached to the hydraulic jack that included two symmetrical

loading bars (12.7 mm diameter) in a 'forked' configuration attached to the loading

arm via a swivel hinge (see Figure 3.8). A retaining spring was connected to the top of

the loading bars to help stabilize and even-out the lateral load between the two loading

bars during the test. This would allow application of equal and balanced line loads

across the face of each of the test blocks throughout the test. An electric hydraulic

pump with a directional control valve (DCV: Emerson 53518) was used to apply P_l

as it is increased gradually until buckling failure initiation. The DCV and electronic

pump provide precise regulation of the application of lateral load and associated

displacement than the hand pump used in the preliminary test configuration. In

order to prevent horizontal sliding displacement of the test blocks on the platens,

two 16 mm-diameter restraining bars were installed in front of the test blocks on each

platen. These restraining bars prevent sliding with minimal impact on buckling of the

test blocks. The THB test apparatus was designed so that various specimen sizes (i.e.,

L, W and T) and loading conditions could be tested with relatively easy adjustments.

In addition, the location of application of P_l can also be readily adjusted.

Monitoring of the experiment during testing is an important component because

of the progressive development of failure concluding with a violent test termination. It
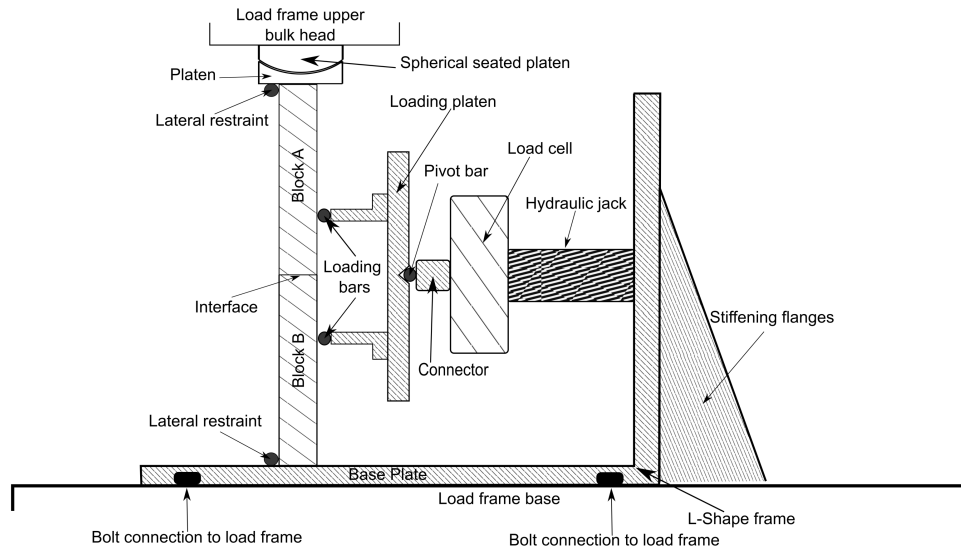
Figure 3.4: The designed fixture used to implement the simple THB failure (Note: the LP and reference tab are not shown in this figure)

is hoped that the test would reveal not only the final buckling loads and displacement at failure, but also provide insight into the progression of the failure mechanism. The monitoring program is based on methods presented by Li and Einstein (2017) for a carefully-monitored four-point bending test. Load magnitudes are measured by load cells in-line with the vertical and lateral loading systems to record P_a and P_l. Axial (vertical) displacement (δ_a) is measured by a linear variable differential transducer (LVDT), although very little δ_a is anticipated during the buckling phase. A small steel reference tab was attached to the loading arm (see Figure 3.9) in order to measure lateral displacement of the loading arm using a linear potentiometer (LP). The monitoring system was set to record automatically and continuously using a digital data acquisition system (DAQ). In addition to these basic monitoring components, a high-speed video camera was used to capture the test in order to provide insight throughout the failure process. This image data also will be analyzed with a digital
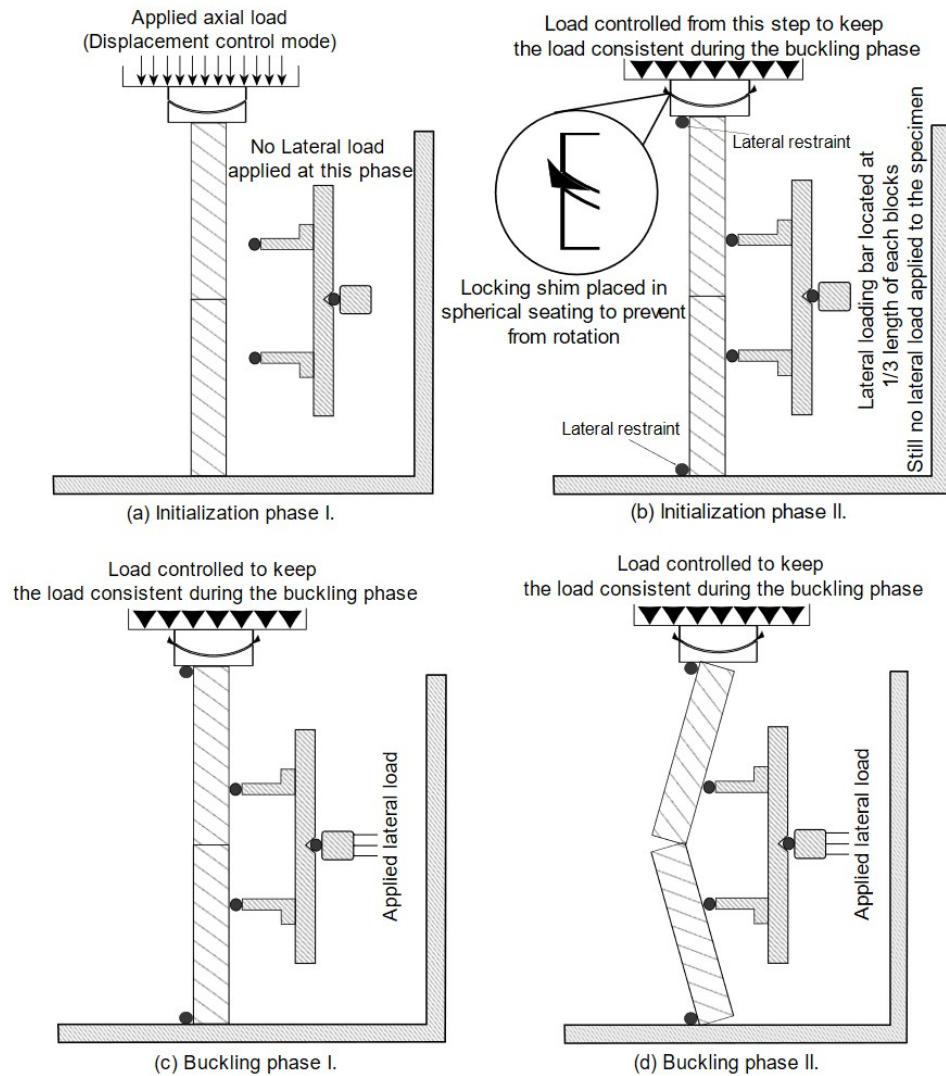
Figure 3.5: THB test boundary conditions, loading configuration and testing sequence. The testing sequence was designed to closely mimic field conditions in two main testing phases: Initialization and Buckling.

image correlation (DIC) processing software to provide the full displacement field during testing. Acoustic emission (AE) sensors will be attached to the test blocks to track 'hit' count (a count of AE events above a predefined magnitude threshold) during the test as a means to further evaluate failure mechanism development. Because the focus of this study was development of the test apparatus and methodology, the DIC and AE systems were not utilized for the preliminary tests in this study. Details regarding the AE and DIC equipment and methods will be provided in a future publication.
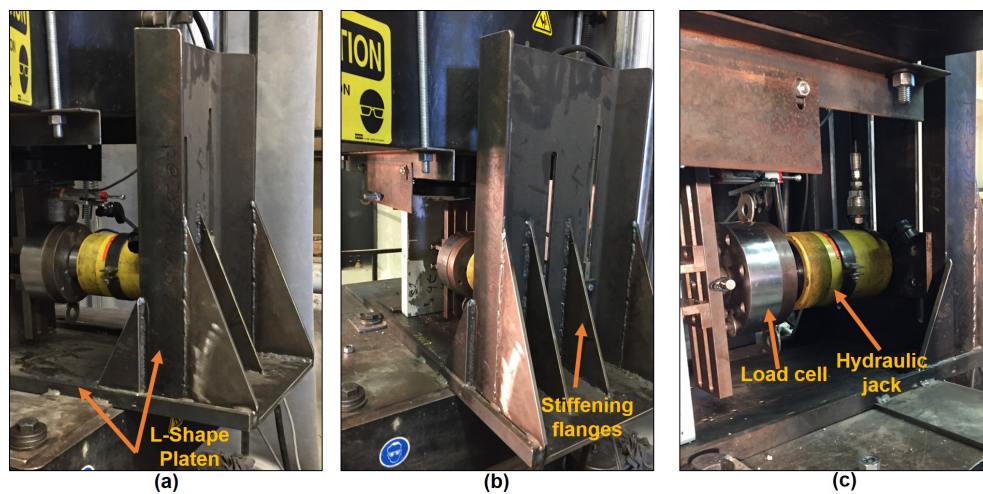
Figure 3.6: The fabricated apparatus setup: (a) L-shape platen; (b) Stiffening flanges; (c) Load cell and actuator

3.4 Test Methodology Development

Standard methods such as those provided by ASTM and ISRM-SM (Suggested Methods) promote much-needed consistency in testing. The THB test has been uniquely-developed in this program and no standard exists. As part of overall test development, test methods were explored, and initial developmental and preliminary testing
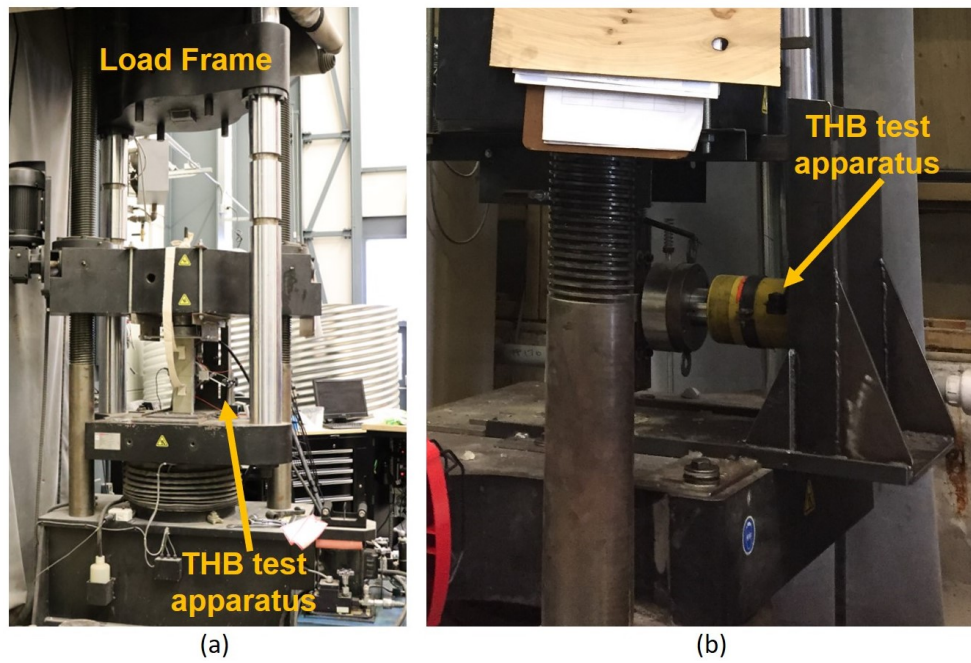
Figure 3.7: The THB test apparatus installed on the 2-MN-capacity load frame
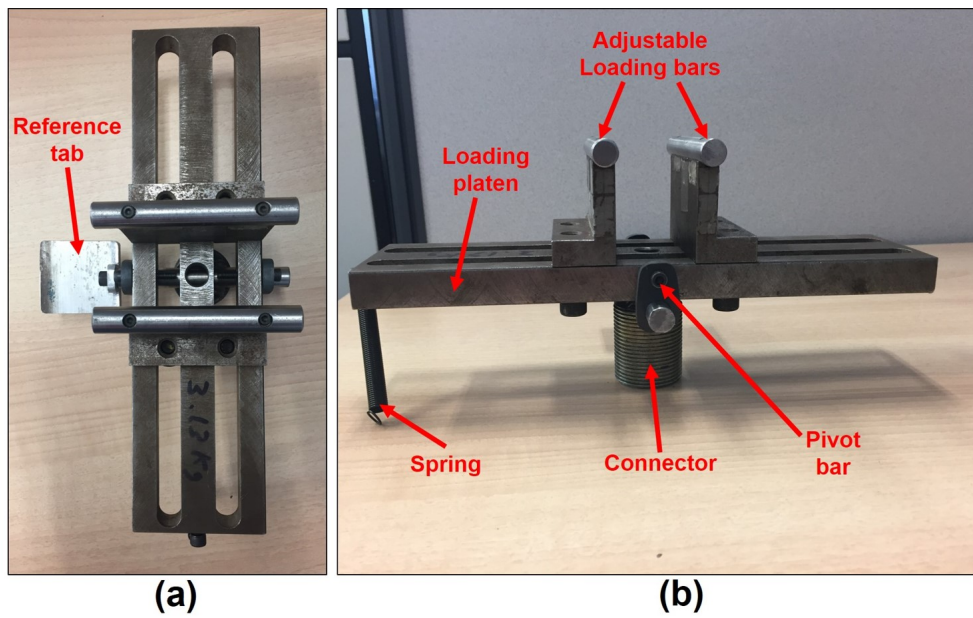
Figure 3.8: Lateral loading platen with load bars. (a) Front view including the reference tab for displacement measurement. (b) Side view showing adjustable loading bars, retaining spring, hinge and connector (to loading arm)
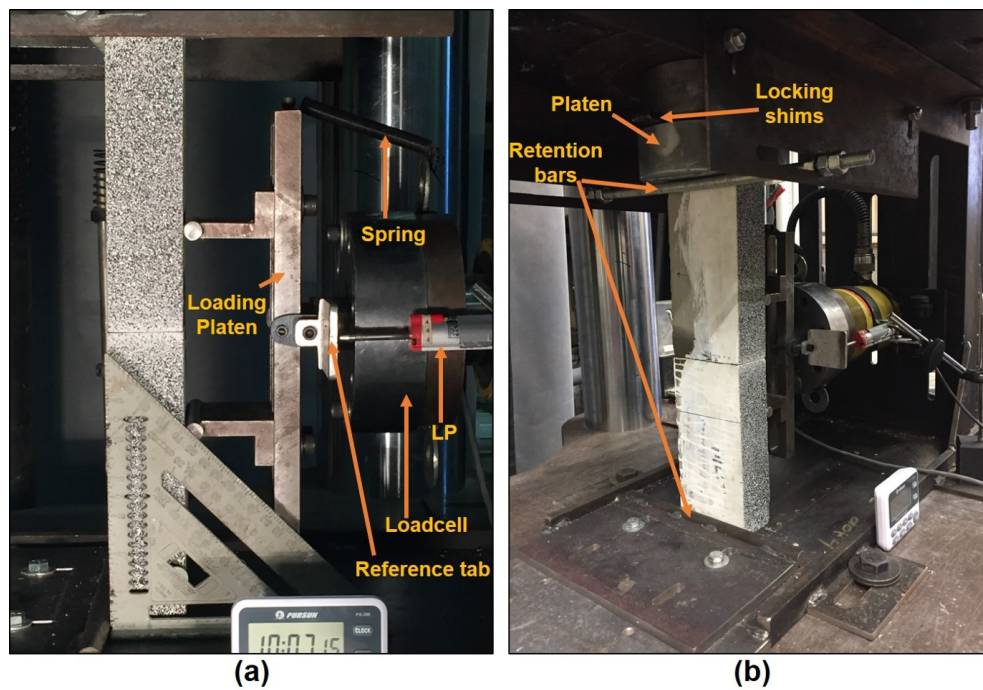
Figure 3.9: THB test setup for preliminary testing on Wallace sandstone test blocks (note the speckled paint pattern on the inner face towards the camera). (a) Position of the sample on the apparatus (b) Location of the upper and lower retaining bars and spherical-seating locking shim

was conducted to refine the apparatus and methodology. Where possible, information from standards for similar tests, such as the three-point bending test (ASTM C1609/C1609M-12, 12) and the UCS test (ISRM, 2007) were considered to guide methodology development.

Careful preparation of the test block specimens was considered to be critical to a meaningful test result so that misalignment of the test blocks does not significantly impact the test results. This is particularly important for the specimen end faces that will be in contact with platens and the interface between the test blocks. Specimens were first cut with a rock saw with care to achieve flat and parallel faces. Although for the majority of rocks, the surface quality is sufficiently treated for testing purposes after saw cutting (ASTM D4543, 2008), each specimen face was then machine-ground using an automatic feed grinder to achieve suitable end conditions. The specimens were carefully inspected for structural flaws (i.e., geological features), such as microdefects or bedding planes, and any of these present were then photographed and documented. One face of the specimens was then surface treated with a speckled paint pattern to enhance image capture for DIC purposes.

Two initial developmental tests were conducted on concrete specimens to evaluate the test apparatus and methodology. Two test blocks were selected that were made from commercially-available concrete paving blocks with dimensions: $L = 17$ cm, $W = 9$ cm, and $T = 4$ cm. The two initial tests were conducted on specimens using σ_a of 10 and 15 MPa. Initially, the two test blocks were carefully aligned within the test apparatus and the lateral loading bars where placed at an equal distance on either

side of the inter-block interface. In the initial tests the loading bars were positioned a distance of 2.5 cm on either side of the inter-block interface (this distance was modified for subsequent tests, as described later). The newly-developed THB test apparatus (Figure 3.4) reproduces the THB failure in a two-phases test: first, the 'Initialization' phase where axial boundary conditions analogous to in situ stress ($\bar{\sigma}_H$) is applied (P_a corresponding to σ_a); and secondly, the 'Buckling' phase where the lateral load to induce the THB failure is applied in an increasing manner (P_l). It is acknowledged that the trigger mechanism used in this apparatus is purely artificial and does not represent any real field condition. However, it is necessary to induce buckling in order to study the failure mechanism in the laboratory and this was considered to be a relatively easily interpretable approach.

Images from select stages of the initial tests are shown in Figure 3.10 and a plot showing δ_l versus P_l is shown in Figure 3.11. After a review of the recorded data, and based on similar laboratory tests reviewed in the literature, the plot of δ_l versus P_l was considered the most meaningful means of evaluating the test performance. These curves showed some non-linearity throughout the test and some 'stepping' in the response data.

From careful observations of the test video, several issues with the test where identified and adjustments were made. Firstly, an improved locking mechanism was needed to hold the spherically-seated platen more firmly in place throughout the test. Secondly, the blocks required better resistance to lateral sliding. Thirdly, it was observed that fracturing in the crushing zone was significantly influenced by the

contact with the loading bars. These issues were addressed by adding a better locking shim to the spherical platen, adding restraint bars to both upper and lower platen, and moving the loading bars farther apart to a distance of 1/3 L from the inter-block interface. In addition, a DCV was installed onto the lateral loading arm to enhance greater control on lateral load and displacement rate. These improvements were implemented and an additional initial test was conducted on a concrete specimen with $\sigma_a = 10$ MPa. The resulting plot of δ_l versus P_l is shown in (Figure 3.11) where it can be seen that the improved test setup has clearly increased the linearity of the data to what might be considered a more 'well-behaved' test response. It should be noted that the apparatus setup described in Section 3.3 is the final setup that includes these design refinements.

(a)   **(b)**   **(c)**   **(d)**   **(e)**
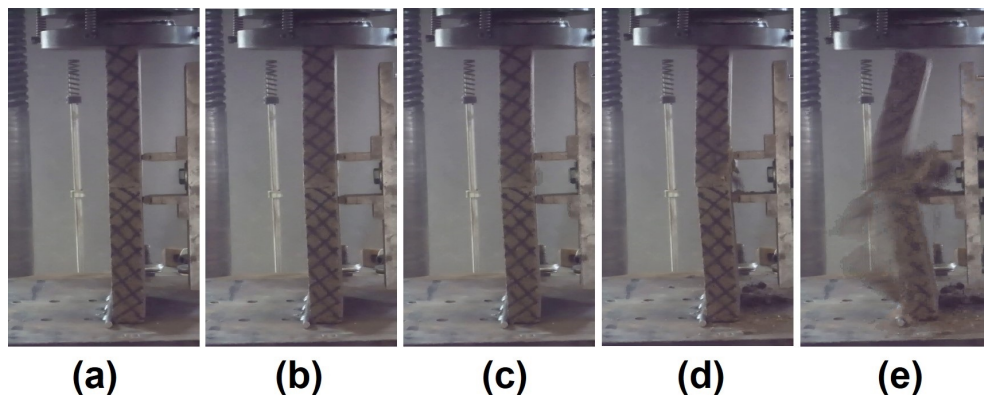
Figure 3.10: Images from select stages of the initial THB test on concrete samples with σ_a =10 MPa (prior to apparatus improvements). A crosshatched pattern was added to the specimens to aid in image interpretation

Upon completion of initial testing, a preliminary test was conducted on Wallace sandstone samples; a particularly homogeneous and consistent sandstone formation found in Nova Scotia, Canada. Two test blocks of Wallace sandstone were cut to the
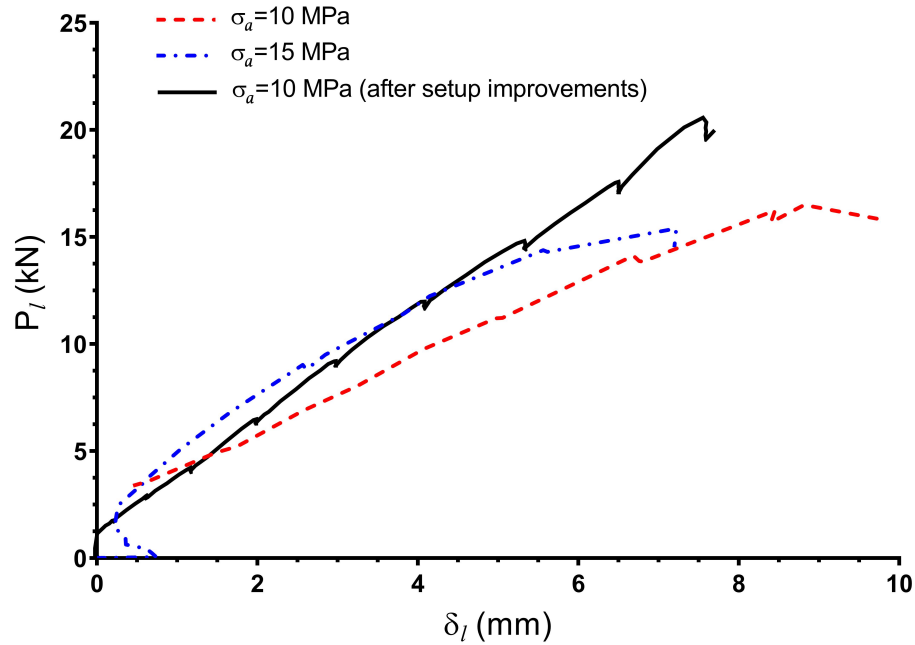
Figure 3.11: Comparison between the initial experimental tests on concrete specimens before and after improvements (described in Section 3) of the apparatus

following dimensions: $L = 20$ cm, $W = 10$ cm, and $T = 5$ cm. The specimens were machine-ground on the end faces to ensure a flat and parallel loading surface, and painted with speckle paint to aid with DIC. The test blocks were placed within the apparatus and positioned evenly along the loading platen. To ensure the lower block did not slide when a lateral load was applied, a restraint bar was installed on the lower loading platen, connected to the base plate (see Figure 3.9). Next, an initial seating load of $P_a = 3$ kN was applied to constrain the specimen, with a spherical seated platen situated above the top block sample, ensuring even load application. Then a second restraint bar was positioned on the top platen, locking the test blocks in-place. Finally, prior to applying the lateral load, the location of the loading bars was measured to make sure contact points were correctly located: evenly spaced with

each at a distance of $1/3L$ from the inter-block interface. The LP was positioned in contact with the measurement reference tab that is connected to the lateral loading arm, as shown in Figure 3.9. A large-display digital clock was placed in front of the apparatus to indicate time directly in the images captured during the test. The data recorded from the load cells, LP, and LVDT was recorded using the DAQ system. The AE system and DIC analysis were not incorporated into the preliminary test.

The test boundary condition setup and loading sequence was conducted as shown in Figure 3.5. In the Initialization phase a $P_a = 75$ kN ($\sigma_a = 15$ MPa) axial load was gradually applied to the specimen. After equilibration under load, a small steel shim, or key, was used to lock the spherical platen to prevent any rotation of the swivel during the Buckling phase. In the Buckling phase an advance rate of 0.5 mm/min was used for lateral loading (i.e., the preliminary test was performed under constant δ_l conditions). This advancement rate was applied until buckling failure occurred. The duration of the Buckling phase was approximately 11 minutes which is within the range recommended by ISRM-SM for the duration of a UCS test.

3.5 Results of the Preliminary Test

The test conducted on the Wallace sandstone test block specimens utilized the refined apparatus setup and methodology as outlined in the previous sections. A series of images captured using the high-speed video camera at various stages of the test are provided in Figure 3.12. The images show the formation of a fracture in the upper test block within the central crushing zone at a relatively early stage of loading causing

the initiation of buckling. This was soon followed by initiation of fractures in the crushing zones at both the upper and lower platen contacts (lateral crush zones in the field condition). However, complete failure did not occur immediately after the initial fracture, but instead occurred after further δ_l was induced. The final failure was violent and was captured clearly by the high-speed images. Fractures were observed in all crushing zones (upper, lower and central), to a depth of approximately 1/3 to 1/2 T (thickness).
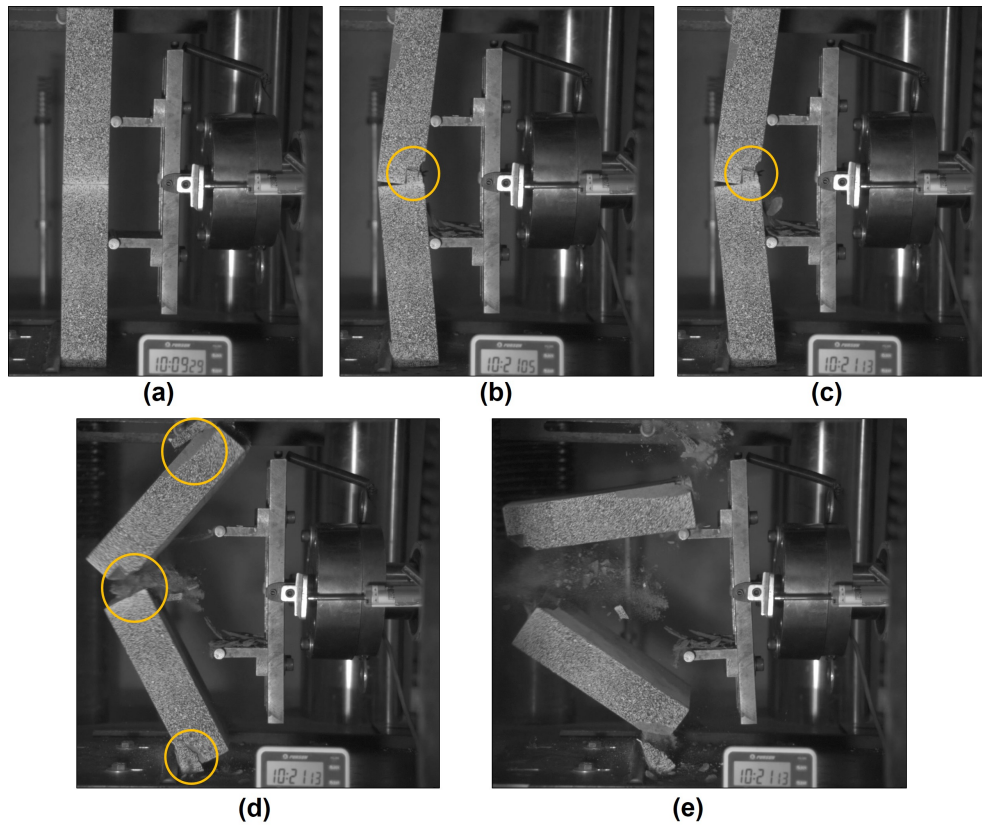
Figure 3.12: Laboratory test of THB on Wallace sandstone: (a) before applying the lateral load (δ_l); (b) and (c) during application of lateral load (δ_l); (d) and (e) after failure. The yellow circle indicates an initial fracture within the central crushing zone. Note the speckled paint showing on the exposed face of the test blocks

A plot of δ_l versus P_l is shown in Figure 3.13. In this figure the images from

Figure 3.12 are identified along the data plot with the exclusion of the post-peak images where displacement data was not accurately captured (the LP reference tab is connected to loading arm and not the specimen). The plot shows relatively linear behaviour until approximately $\delta_l = 6.5$ mm where the formation of the initial fracture in the top block's central crushing zone can be clearly seen in both the image and the test data. The lack of non-linearity in its behaviour may be partly due to the constant stress axial boundary condition. Complete failure occurred at $\delta_l = 11.5$ mm with a peak load of $P_l = 34$ kN. A plot of δ_l versus δ_a is also shown in Figure 3.13 to provide insight into the behaviour at the test platen boundary during the Buckling phase. δ_a is positive for downward displacement of the upper platen. As expected, δ_a is relatively small with constant stress conditions applied from the vertical load frame. Initially, the upper platen moves downward (increasing δ_a) as the blocks move laterally. This changes quickly to upward displacement (decreasing δ_a) as the kinematics of block rotation push the test block corners upwards and into the platens with resulting maximum of $\delta_a = -0.5$ mm at failure. P_a was monitored throughout the test and it was observed to hold constant in agreement with the boundary conditions intended for the test until the violent failure event (i.e., post-peak).

Although the high speed camera was used to record the test, the DIC data was not synthesized, but instead the images were manually reviewed to reveal failure mechanism advancement. AE data was also not recorded for this preliminary test. Both the DIC and AE data will be collected and synthesized in a future formalized parametric testing program.
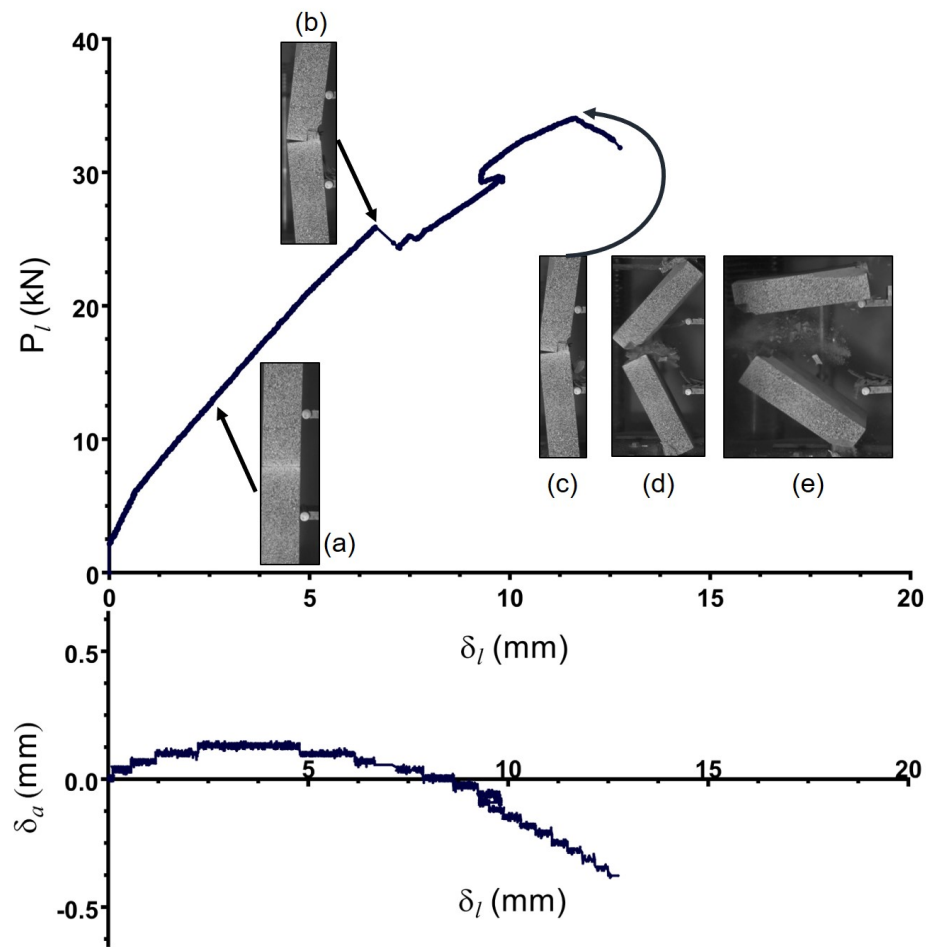
Figure 3.13: Characteristics lateral load-displacement behaviour during the THB test on Wallace sandstone

3.6   Numerical Simulation

A simplified numerical model was developed to simulate the experiment in order to
provide insight into the stress magnitudes throughout progression of the test. The
commercial software code *3DEC*[1] was used to simulate the preliminary experimental
test on Wallace sandstone. *3DEC* is a distinct element method (DEM) code used for
discontinuum modelling (Itasca, 2014). This code uses the finite difference method
to simulates both continuum regions (i.e., rock blocks) and also the interfaces (i.e.,
joints) between continuum regions. The code allows for linear (elastic) and non-linear
(elastoplastic) behaviour of both continuum regions and interfaces. The goal of this
modelling exercise was to simulate the experiment using a simple elastic model for
the test blocks with an elastoplastic (i.e., failure) model for the interfaces to allow
the necessary inter-block movement that occurs during the test. Ultimately, a more
complex modelling approach (e.g., micromechanical modelling) will be utilized to
capture the brittle failure behaviour observed in the test; however, for the purpose of
development and evaluation of the test apparatus, this simplified model simulation
provides useful insight.

The simulated THB experiment included two test blocks with dimensions of $L =$
20 cm, $T = 5$ cm, and $W = 10$ cm. Platens were included explicitly within the
model as very stiff blocks. The boundary conditions were similar to the actual test
with a constant axial (vertical) stress initialized on the upper platen which was then
'locked in' by fixing the platen vertically. The lateral trigger was simulated with an

---

[1]www.itascacg.com

applied velocity boundary conditions in a line across the face of the test blocks at a distance $1/3L$ away from the inter-block interface. This lateral boundary condition allows the model to advance through the buckling phase in a controlled manner in order to observe simulated conditions throughout test advancement. These slightly simplified boundary conditions are suitable to provide insight into the test given that it is a simple elastic model. The model setup is shown in Figure 3.14.
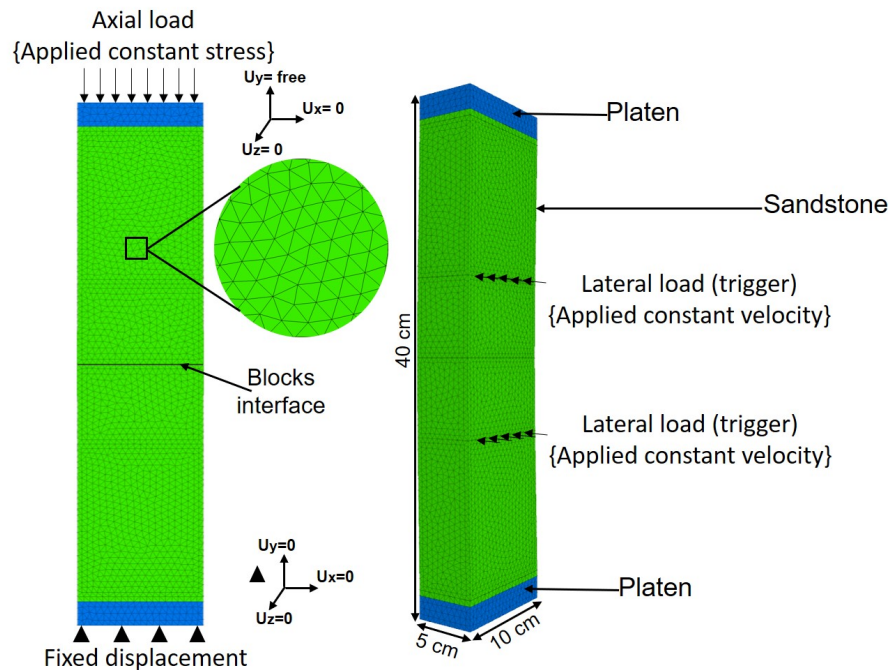
Figure 3.14: *3DEC* model setup for simulation of simple THB buckling failure of Wallace sandstone test blocks

The test blocks were simulated with mechanical properties and geometry based on those of the experimental test conducted on Wallace sandstone. The Wallace sandstone blocks were modelled with a linear elastic continuum model with material properties: $E = 17.5$ GPa, $\nu = 0.22$, and $\rho = 2600$ kg/m^3 (Corkum et al., 2018b). The interface model parameters used in the *3DEC* were estimated based on values

for similar rock interfaces reported by Kulhawy (1975). A brief parametric study was conducted on the interface stiffness values, applying uniform parameters in each analysis for both block-platen and block-block contacts ($K_n = K_s$ of 1×10^2, 1×10^3 and 1×10^4 GPa/m). The interface strength parameters used were $c_j = t_j = 0$ for all interfaces and $\phi_j = 3$ and 35° for block-platen and block-block interfaces, respectively.

In the first stage, the vertical boundary conditions were applied and the model was cycled until a state of equilibrated was achieve under the initial boundary conditions. The second stage involved addition of the lateral velocity boundary condition (trigger) and the model was cycled (stepped through time) in order to advance the buckling behaviour. The lateral applied velocity boundary condition was 1×10^{-5} m/s. The applied velocity boundary magnitude was selected so that it was low enough that the model would remain in quasi-static equilibrium throughout the simulation. The model was cycled until it had displaced laterally (δ_l) a distance equal to that coincident with failure observed in the actual preliminary test case. The model was monitored by tracking various stresses and displacements within the model using the code's built in *history* functions and with custom-programmed *FISH* function histories.

A comparison of the laboratory experimental results of the Wallace sandstone test blocks with the *3DEC* simulation is shown in Figure 3.15 and Figure 3.16. Figure 3.15 shows the δ_l–P_l response of the observed experimental test with that of the *3DEC* simulation for various values of interface stiffness. The best match of the data is achieved by the higher stiffness values; however, in order to properly simulate the response a more sophisticated, calibrated model is required. Figure 3.16 shows images

of the post-failure blocks where fractured rock regions are evident. The model images show contours of vertical (σ_y) stress from the elastic model when δ_l was coincident with the actual, experimentally-observed failure. From UCS tests conducted on Wallace sandstone (Corkum et al., 2018b), σ_c is typically approximately 80 MPa (800 bar). Based on the plotted model contours of σ_y, the experimentally-observed failure zone corresponds approximately with the region in the model defined by 100 MPa vertical stress. Because this is a simple elastic model, no stress redistribution from pre-failure damage, such as fracturing and microcracking, is accounted for in the model.
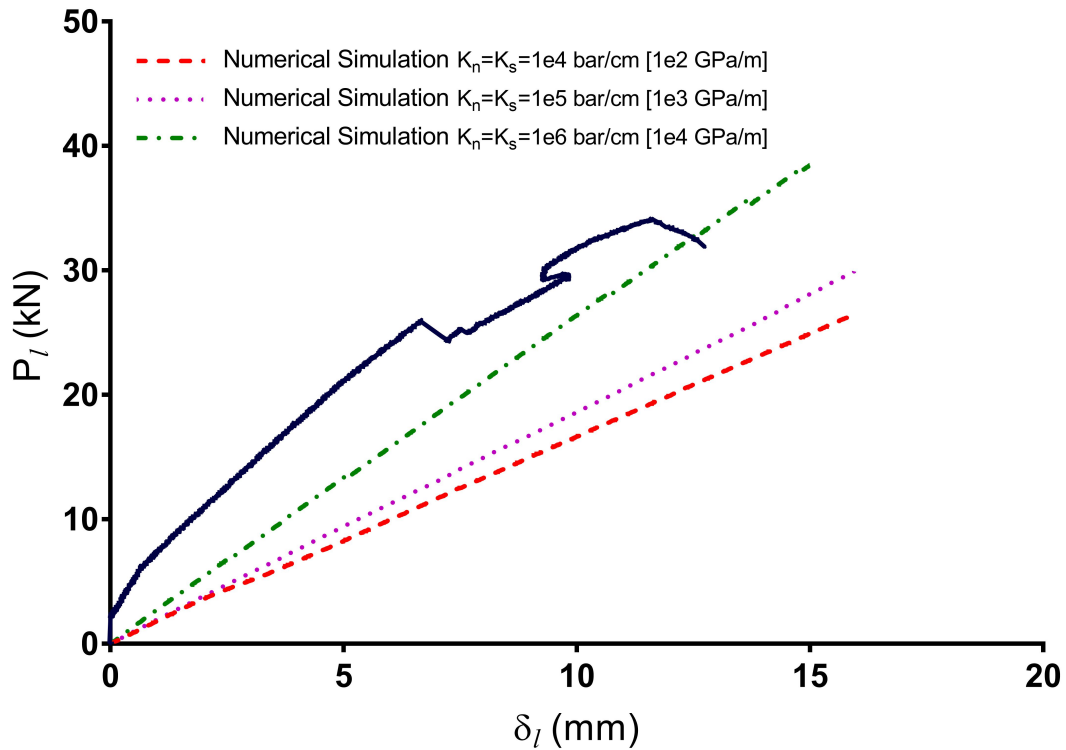
Figure 3.15: Comparison of laboratory test to numerical model results for a range of joint stiffness values.

Cavers (1981) hypothesized that THB failure is governed by σ_c in the crushing
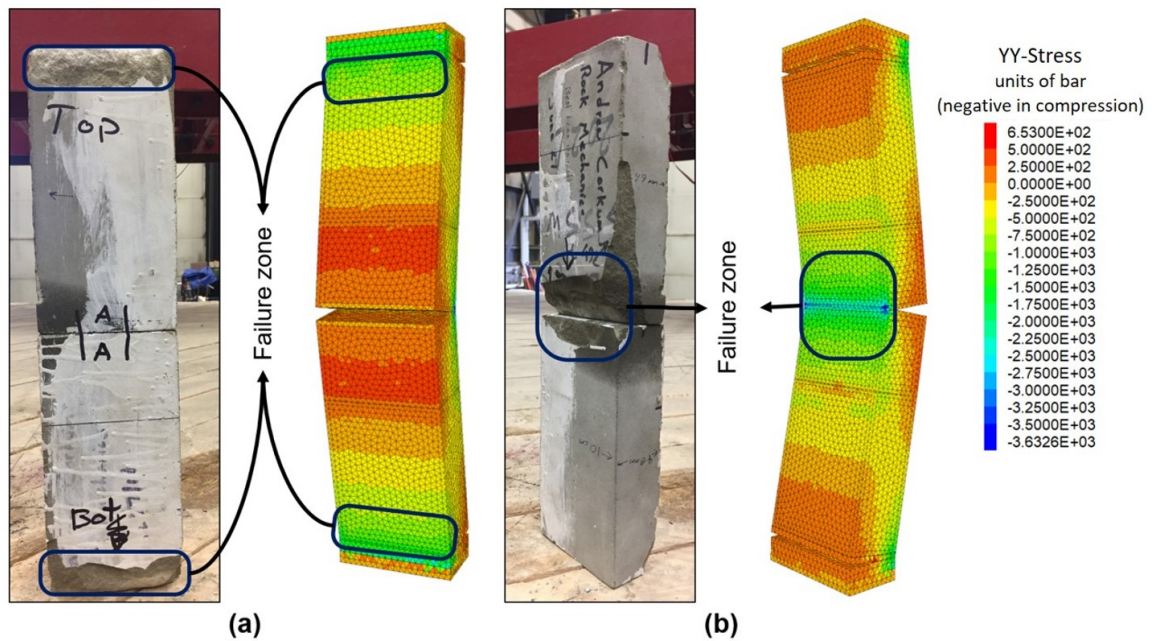
Figure 3.16: Comparison of axial stresses in the crushing zone in the numerical model ($K_n = K_s = 100$ GPa/m) and the experimental test. The contour plot shows the vertical stress (σ_y) in bar (negative in compression)

zones. Preliminarily, this hypothesis is supported by the experimental test-model comparison. Given the simplified nature of this model, further evaluation using more sophisticated modelling techniques that can replicated brittle rock failure is required for confirmation. However, the model simulation does support that the experimental setup and methodology reasonably reproduces the THB test.

3.7 Conclusion

Understanding and predicting quarry floor buckling failure, or pop up, is becoming increasingly important for quarry and mine operators. A first step is to gain greater insight into well-constrained, simplified buckling failure under controlled laboratory conditions. Although the THB failure mechanism is a simplification of most buckling

failures observed in the field, the fundamental nature of this failure mechanism is not well understood. A novel experimental apparatus and testing methodology was developed to simulate the THB failure mode. This involved design and fabrication of a test apparatus that could be fitted to an existing vertically-aligned, high-capacity load frame. Two carefully prepared prismatic rock specimens were stacked vertically within the test frame in a THB configuration. The load frame was used to provide an axial load (P_a), analogous to the horizontal in situ stress ($\bar{\sigma}_H$). A 'trigger' mechanism was applied using lateral loading bars to drive the two-block configuration with lateral load (P_l) in a controlled manner through the buckling failure process. Axial and lateral, load and displacements were recorded and high-speed video images were recorded throughout the test. Future testing will incorporate both AE monitoring and DIC data analysis.

Development of the test apparatus and methodology required numerous initial and preliminary tests, and subsequent modifications to arrive at an experimental procedure that resulted in a test with well-understood boundary conditions and loading sequence. For example, developing a method for locking of the platen swivel after axial loading, but prior to buckling initiation to insure uniform horizontal loading, but with buckling occurring with the specimen ends against a fixed, stress-controlled, flat platen boundary. Specimen preparation techniques were developed to obtain suitably parallel and level test block end conditions. One of the main features of the test apparatus is versatility and adjustability of the test configuration to support future

parametric studies. The apparatus was designed and fabricated to be completely adjustable. This allows for testing under various geometrical configurations (e.g., block dimensions L, T and W) and under different initial σ_a values (analogous to $\bar{\sigma}_H$). Exploring the results from a range of test configurations under controlled experimental conditions with extensive monitoring, is essential for development of analysis and design methods.

The resulting preliminary experimental test yielded results that we consistent with the anticipated response and also provided insight into controlled THB behaviour. Fracturing in the crushing zones was observed prior to complete failure while maintaining some reserve, additional buckling resistance even after initial fracturing occurred. Fracturing was observed within all of the anticipated hinge crushing zones. The crushing zone extent was observed to be approximately 1/3 to 1/2 of the specimen's thickness (T). As hypothesized, complete through-going fractures with detachment of material in the crushing zones was required for complete, violent buckling failure to occur. A future parametric testing program utilizing the apparatus and methods described in this paper, will be conducted to explore the key parameters influencing THB failure. The test may also serve as a means to further study high-stress brittle rock failure in addition to the THB failure mode.

A simplified elastic distinct element method numerical model to simulate the test was developed using *3DEC* software. Although the elastic model is not capable of capturing failure of the intact rock, the interfaces between blocks and platens was realistically simulated (e.g., sliding, separation and rotation). The model showed

that in the crushing zone(s) the axial stress was greater than the σ_c of the specimen. However, further testing and interpretation is required to more clearly quantify this associated brittle failure mechanism.

The trigger mechanism that drives the THB failure process in the field is not fully understood at this time. The current experimental configuration uses lateral line loads to drive the test through to buckling failure. In order to explore the effects of a uniform load as a trigger mechanism, the experimental apparatus could be modified for future testing with a pneumatic pressure bladder to apply a pressure to the test block surfaces. This modified apparatus would reasonably simulate loading of the buckling stratum by water pressure to explore this anticipated buckling failure trigger mechanism.

Publication Notes

Acknowledgements

Funding Sources

organization.

Compliance with Ethical Standards

The authors declare that they have no known conflict of interest with respect to the study presented in this article.

Chapter 4

An experimental study and modelling simulation of three hinge buckling

M. Ghasemi, A.G. Corkum

4.1 Abstract

A laboratory experimental program has been conducted to investigate three hinge buckling failure (THB) using a newly developed THB testing apparatus and methodology. The objective of the study was to gain quantifiable insight into the THB failure mechanisms to inform future development of stability analysis methods. Specimens of the relatively homogeneous Wallace sandstone formation were selected and a total of seven tests were conducted to parametrically explore a range a specimen thickness (3.2 to 5 cm) and two levels of axial 'clamping' stress (10 and 15 MPa). In addition to load and displacement monitoring, digital image correlation (DIC) and acoustic emission (AE) data was collected during each test. The tests revealed relatively consistent characteristics behaviour with an identifiable thresholds of yield, peak and failure (collapse). A brittle-ductile response transition was observed based

on the tested parameters, although not clearly identified from the limited testing. A clear relation was develop for specimen thickness and axial stress. A distance element grain-based modelling simulation of the experiment was conducted based on calibration with unconfined compression test values of the specimens. The simulation showed a reasonable match to the characteristic behaviour. This provided greater insight into the THB failure mechanism and showed that this method of simulation is a suitable analysis method for this mode of failure.

Keywords: three hinge buckling, distinct element, DIC, acoustic emission

4.2 Introduction

Although buckling failure modes are relatively common in rock engineering the analysis of buckling problems continues to pose a challenge. Issues related to geometry, stiffness, strength, loading and boundary conditions make all but the simplest buckling problem difficult to analyze. Over the past decade near-surface buckling in highly-stresses, horizontally-bedded sedimentary rock units has become a concern for aggregate mining and quarry operations. Numerous cases of observed buckling failure has been report, for example Adams (1982); Roorda et al. (1982); Wallach et al. (1993). A database of historical cases documented in the literature has recently been compiled by Ghasemi et al. (2020) who also presented a classification for near-surface buckling modes based on these collected cases.

As a starting point in better understanding these buckling modes, a novel testing apparatus was developed by the authors to carry out three hinge buckling (THB) tests under controlled, and carefully monitored experimental conditions (Ghasemi and Corkum, 2020b). The THB failure mode, first described by Cavers (1981) for rock slopes, is a relatively simple buckling mode that occurs in rock. It is relatively common in laminated/layered rock units with cross-bedding structures resulting in a blocky structure. In THB, high stresses acting within the rock layer drive failure of a two-blocks system forming a tent-like post-failure configuration. For this mode to fully develop, some internal fracturing must occur within the intact rock at the hinge points between the blocks allowing kinematic freedom for block rotation. Often some type of 'trigger' mechanism is required to initiate the buckling event, moving it from

a stable configuration to an unstable configuration, such as blasting vibrations, or water pressure.

The test setup allows for THB to occur with simplified boundary conditions similar to field conditions. Axial confining stress (σ_a), or 'clamping' stress, corresponding to the field condition of horizontal in situ stress is applied to the test blocks throughout the THB test. Buckling is driven by horizontal load platens applying an increasing lateral load (P_l) until failure occurs. The test system was developed so that a range of block specimen dimensions can be tested under a range of σ_a values. The objective of this study was to use the newly developed THB test to explore the buckling response and stability of various test configurations through a parametric study. A range of block thickness (T) was explored under two levels of σ_a (selected similar to typical in situ stress values). The testing program was conducted on block specimens of Wallace sandstone. Advanced laboratory monitoring methods, i.e. acoustic emission (AE) and digital image correlation (DIC), were utilized with the experiments to obtain valuable data such as the apex displacement, crack growth and fracture initiation during the THB failure process.

To provide further insight into the experimental response, a numerical modelling program was conducted to simulate the THB test. The grained-based model (GBM) using *UDEC* (Itasca, 2014) Voronoi tessellation method was used because it can capture elastoplastic behaviour of a continuum and discontinuum and also can include the effects of fracture formation and propagation throughout the failure process. The model was calibrated to unconfined compressive strength (UCS) tests. A properly

calibrated GBM is a suitable tool to capture this complex failure mode in the laboratory and may also prove to be a key means of field analysis of THB and more complex modes. However, scale effects will have to be accounted for in any upscaled analysis.

4.3 Experimental Program

The newly developed THB experimental methodology introduced by Ghasemi and Corkum (2020b) was used to reproduce simple THB and capture the progression of yielding and ultimate violent failure associate at the laboratory scale. The THB experiment requires a two-rock-block system, stacked vertically (one on top of the other) under axial confinement to simulate the boundary conditions of a 'clamping' horizontal in situ stress of the field condition. Also, a trigger mechanism to initiate buckling failure is part of this experiment via lateral loading. In this study, seven THB tests were conducted on Wallace sandstone specimens with the proposed THB experimental setup.

4.3.1 Test Specimens

The Wallace sandstone, a durable and consistently homogeneous sandstone, was used for the THB experiments. The Wallace sandstone has been quarried for the last 150 years and used for many building and monument construction projects. Wallace sandstone was chosen for the experiments because it was one of the main rock type that buckling failure observed in the field and readily-available and accessible commercially in various pre-cut dimensions in Nova Scotia, where the THB experiments

were carried out at Dalhousie University. Wallace sandstone is from the Cumberland group of the late carboniferous Boss Point formation (Dickie, 1993). The sandstone typically consists of approximately 82% Silica, 8.12% Alumina, and Hematile 3.19% (NRC-NS, 1967). According to Dickie (1993) the olive-coloured Wallace sandstone used in this study has an average unit weight of 2320 Kg/m^3, with a UCS value of $\sigma_c = 94$ MPa.

Some laboratory characterization testing has been carried out on the Wallace sandstone as part of this study. All tests were conducted in accordance with the ISRM Suggested Method (ISRM, 1977). A summary of the test results are shown in Table 4.1. The six tests show four had relatively consistent σ_c of approximately 80 MPa with one test substantially higher and one substantially lower than these. The data showed a mean and median σ_c of 87 and 81.6 MPa, respectively. Only the high and low test results had measure values of Young's modulus (E) with consistent values of Modulus Ratio (MR $= E/\sigma_c$) of approximately 300. Also, 3 Brazilian tests (each test include 10 disks) conducted based on ther ISRM Suggested Method (Bieniawski and Hawkes, 1978) were carried out in order to obtain the tensile strength of the Wallace sandstone. The average tensile strength (indirect Brazilian) obtained from these experiments was about $\sigma_t = 5$ MPa.

Table 4.1: UCS tests on specimens of Wallace sandstone

Test ID	σ_c (MPa)	E (GPa)	MR
UCS-1	81.61	-	-
UCS-2	81.54	-	-
UCS-3	81.6	-	-
UCS-4	80.5	-	-
UCS-5	137	39.8	291.6
UCS-6	59.9	17.7	295.7

4.3.2 Experimental Methodology

The proposed THB experiment is a newly-developed test with no pre-existing standards or procedure, Ghasemi and Corkum (2020b). Some minor modifications/reinforcing was added to the test apparatus for the testing conducted in this study, including reinforcing the load frame base, stiffening flanges, and loading platen before the THB experiments were carried out. In order to monitor the experiments, monitoring methods similar to those used by Li and Einstein (2017) for four-point bending tests were utilized. Two load cells in alignment with the lateral and axial load actuators were used to measure the P_a and P_l values. A linear variable differential transducer (LVDT) recorded axial displacement (δ_a), and a linear potentiometer (LP) attached to the lateral loading platen reference tab was used to capture the lateral displacement (δ_l) of the loading ram. Two advanced monitoring methods, AE and DIC methods, were also implemented and used during these experiments to monitor the THB process and capture the crack initiations and crack 'hit' count during test evolution. Figure 4.1 shows the THB test setup up and monitoring locations used during the THB experiment.
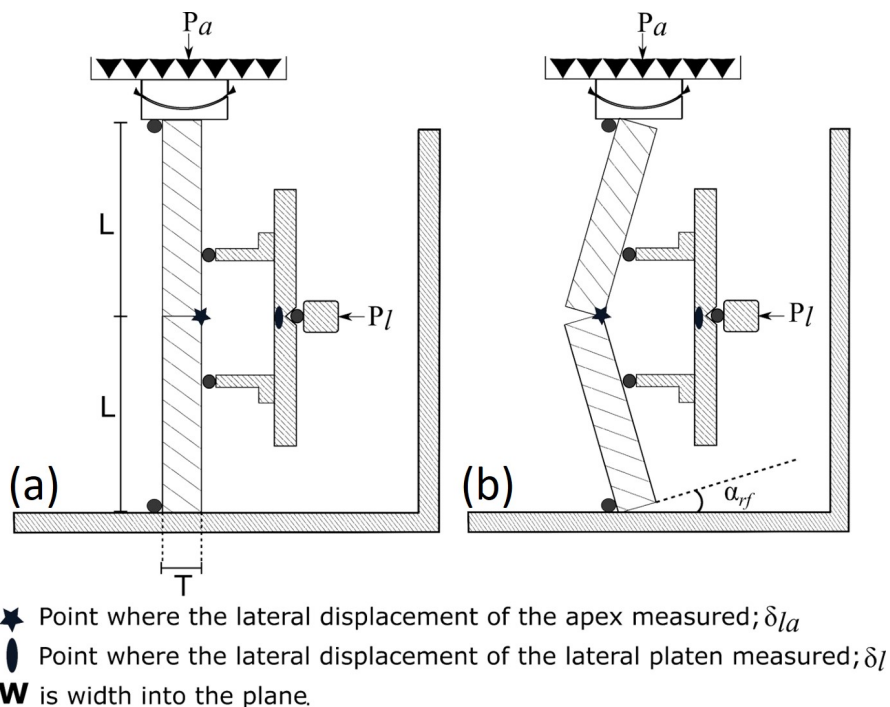
Figure 4.1: Schematic of the THB test apparatus showing the test setup and monitoring locations

A high-speed video camera was used to monitor and capture the THB failure development in the specimens. The camera is a Chronos 1.4 (1.4 gigapixel-per-second (Gpx/s) monochrome), available commercially from Kron Technologies Inc. This camera has a 1.3-megapixel image sensor that captures 1057 fps (frame-per-second) images with a resolution of 1280 × 1024, and up to 38500 fps at a lower resolution. In this study, the high-speed video camera was set to record a video with 1057 fps. The captured video was utilized to observe the fracture initiation and patterns within the test specimen while THB progresses. The video was then converted to image series and used with the DIC method (computer-aided image pixel location tracking) to capture and quantify the displacement and rotations of specimens during the experiments.

A second high-resolution camera (Canon EOS Rebel SL3) was also used to monitor the whole buckling experiment's overall progress, including the specimen, THB apparatus, and load frame. The Canon EOS Rebel SL3 is commercially available by Canon and features a 24.1 Megapixel sensor that can capture high-resolution images up to 6000×4000 resolution and record 4K videos. These two cameras were set to record the THB experiment simultaneously.

In order to utilize the DIC method, the Ncorr programming routine was used to analyze the images obtained via a high-speed video camera. Ncorr is an open-source 2D digital image correlation MATLAB program (Blaber et al., 2015). This open-source program provides a GUI (graphical user interface) in the MATLAB environment that uses DIC analysis and output easily and efficiently. Digital Image Correlation (DIC) is a method that tracks any movement or strain of an object captured in a series of images. This method is done by dividing the first image into pixel subsets groupings and each subset has a pattern. Then, by searching and matching the pattern movements in the image series, each subsets' displacement is calculated, which results in the calculation of displacement and strain of the object captured in the images.

The AE technology is widely used for different laboratory tests, such as three-point bending tests on steel-reinforced concrete in civil structures, hydraulic fracture tests for the oil and gas industry, and also rock mechanics tests. This technology can locate microfracture formation and propagation events acoustically during the experiments, leading to a better understanding of rock failure progression. The AE system used

in this experiment included a Milne16 data acquisition system, a Trigger-Hit-Count (THC) hardware, and Pulser Amplifier System (PAS) commercially available from Applied Seismology Consulting Limited (ASC). The Milne16 is a multi-functional and multi-channel DAQ (up to 32 channels) with the ability to store all channel data at the same time, and could be used in microseismic (MS) and AE event monitoring. The THC system also was used accompanied by the Milne16 DAQ to capture the trigger and hit counts during the AE monitoring. The PAS also is a multi-channel system, including the Pulser Amplifier Desktop units (PADs) and Pulser Interface Unit (PIU). The PAS system enables pre-amplification and switching between pulsing and receiving modes for all transducers, and each PAD has an optional hearing interval between 30 to 70 dB with a broad frequency response. This system was utilized in the THB tests using two AE sensors (NANO-30), one at the top specimen and the other on the bottom specimen during the THB experiments. It is important to monitor the event until the end of the experiment. Therefore, the sensors' location was chosen at the place that has minimal possibility of fractures or failure. Each sensor was located at the $2/3\ L$ from the blocks interface, and on the same side that the lateral loading platen were located .

The InSite Lab software was used to analyze the data obtained by the AE system. Our focus in this study was to capture and analyze the hit count during the THB tests. The InSite Lab is a data acquisition, data processing and management, and data visualization software incorporated with the AE system and commercially available via ASC. InSite Lab allows for presentation of output such as hit count, waveform

processing (manually and automatically), and 3D spatial visualization of events.

The first step in the THB tests was specimen selection and preparation. The Wallace sandstone specimens chosen in this study were inspected and selected so that no major geological structures were observed (i.e., pre-existing fractures). The specimens were then carefully prepared to have parallel ends while cutting with a rock saw. Specimens were machine-ground after cutting to achieve a proper surface condition. After preparation, specimens were again investigated to be free of structural defects and flaws, before taking images and documenting specimens. Then, specimens were painted carefully using a speckled paint texture to increase the DIC method's accuracy to enhance images captured via high-speed video camera.

Seven THB tests were carried out to study the THB failure mechanism and understand the critical parameters that play a role in THB failure. The specimen thickness (T) and the 'clamping' or axial load (P_a), or expressed as an axial pressure (σ_a), are thought (based on mechanistic behaviour) to be two main parameters that effect THB failure. Therefore, this paper is mainly focused on the effect of these two parameters on buckling failure. In this study, tests were conducted on specimens with similar length (L) and width (W) and different T. As a result, these seven tests were carried out with $L = 20$ cm and $W = 10$ cm, and T ranging between 3.2 cm to 5 cm. These specimens geometries were chosen based on limitations that exist for the experiments, such as load frame capacity and available space within the test setup. The geometrical parameters used for these experiments are summarized in Table 4.2.

Table 4.2: Summary of the THB experiments conducted on Wallace sandstone.

Test ID	Specimen ID	T (cm)	L (cm)	W (cm)	T/L	σ_a (MPa)
T39S10	SP4	3.9	19.9	9.8	0.20	10
T35S10	SP7	3.5	19.8	9.8	0.18	10
T33S10	SP2	3.3	19.7	9.2	0.17	10
T50S15	SP0	5.0	20.0	10.0	0.25	15
T44S15	SP3	4.4	19.9	10.5	0.22	15
T34S15	SP1	3.4	19.8	10.0	0.17	15
T32S15[*]	SP5	3.2	19.8	9.9	0.16	15

*Top and bottom blocks of this test were slightly different in thickness(3.2T/3.6B)

Specimens were placed on the apparatus centred on the base platen and aligned parallel to the loading platen. The boundary condition steps and loading orders were followed based on the THB experiment methodology suggested by Ghasemi and Corkum (2020b). The lower restraint bar was placed in the front of lower block to prevent lateral sliding while the axial load was applied. An initial axial seating load was applied ($P_a = 10$ kN) to ensure good contact of the upper spherically-seated platen. The second, upper restraint bar was positioned at the top platen to lock the specimen blocks in-place. The lateral bars were placed at $1/3$ L above/below the inter-block interface on the back face of each block before applying the lateral load. Then, one AE sensor was attached to the front of each block at $2/3$ L in order to track the cracks counts produced during the THB process. At this stage, the connection of LP, LVDT, load cell, and AE sensors were checked for properer working conditions. Also, a simple digital clock was placed near the test specimen to track time directly within the recorded videos. The data obtained from LP, LVDT, and load cell were controlled and recorded automatically using the same DAQ system and the AE data

was captured using a separate DAQ system.

The axial confinements (σ_a) used in these experiments was based on typical values of horizontal stresses observed in the field. Based (Kaiser and Maloney, 2005; Corkum et al., 2018a), the maximum horizontal in situ stresses reported for Ontario is somewhat between 9 to 12 MPa; however, this can vary significantly based on various factors such as surface topography. Therefore, in the initial phase the load frame was directed to apply σ_a of 10 or 15 MPa using the spherically-seated platen, providing uniform loading to the test specimens.

Before starting the buckling phase of the test, and after applying the axial confinement, locking steel shims were placed within the spherically-seated platen to prevent rotation of the upper platen during the buckling phase. Using a DCV system, the lateral load was then applied to the specimens with the 0.5mm/min advance rate. The duration of these THB experiments was 10-15 minutes on average, which is within the range suggested for UCS testing by the ISRM Suggested Method (ISRM, 1977).

4.3.3 Experimental Results

Different equipment types such as load-cell, LVDTs, LPs , high-speed camera with DIC, and the AE system were used to observe the THB process. Because this is a newly developed test, it was not clear what was the most informative format to present the data; however, similar tests, such as four-point bending and masonry panel testing, provided some insight. The test data was synthesized and plotted in various forms, to elucidate the key test responses.

The direct test measurements included axial (P_a) and lateral platen loads (P_l), and axial (δ_a) and lateral displacement (δ_l). The δ_l is a measure of the displacement of the reference tab which is connected to the plate that holds the upper and lower later platen bars and is, therefore, a measure of the average lateral displacement of these two lateral platens. The platens contact the test specimens at a distance of $\frac{1}{3}L$ from the mid-block interface and are thus not a direct measure of the movement of the apex at the inter-block interface. The apex displacement measure (δ_{la}) is likely the most meaningful displacement in terms of THB behaviour. In addition, the rotation angle of the blocks (α_r) is also of interest. Both δ_{la} and α_r where calculated based on specimen geometry and directly-measured δ_l values. Both of these indirect measurements were also verified by comparison with high speed camera images using DIC.

Figure 4.2 $(\sigma_a = 10 \text{ MPa})$ and Figure 4.3 $(\sigma_a = 15 \text{ MPa})$ consist of monochrome image series captured using the high-speed video camera showing the progressive stages of the THB tests for each specimen. These specimens are painted with speckling and the images have been digitally enhanced (i.e., increased image contrast) to increase visibility. These images show the essential stages of the experiments, including buckling initiation (fracture initiation at the central crushing zone, and the lower and upper platen contact) and complete buckling failure. It was observed that the failure process for all THB experiments was somewhat similar and occurred in two main phases, 'buckling yield' and final, catastrophic 'buckling failure'. During the buckling yield phase, fractures first initiated in the central crushing zone (process

zone) which indicates initiation of the buckling process. Initial fractures started from specimens' surface and then progressed to a depth of approximately 1/3 to 1/2 of the specimen thickness, except for one experiment: T33S10. In specimen T33S10 the initial fracture starts from the center of specimen thickness, due to what appears to be a micro defect that was not observed during the specimen preparation. Soon after formation of initial fractures near the central hinge, additional initial fractures were observed near the upper and lower platen contact hinge zones. At this point, the buckling yield phase was completed and this typically corresponds to where the maximum P_l was often observed. It was observed that after the buckling yield phase, some resistance until rupture still exists. With additional lateral loading increasing damage occurred until the buckling failure phase where complete failure occurred. The final stage of buckling failure was violent and rapid, captured clearly by the high-speed camera images. Based on visual observation, there seems to be some variation in the test progression from peak to rupture. In some cases the damage is relatively confined to the hinge zones. However, in many cases a fracture can be observed to propagate axially into a block from the inter-block interface. As the fracture propagates and the blocks rotate, the unfractured block (the one without the large, explicit, propagating fracture) will start to push open the fracture in the opposing block resulting in tensile fracture propagation. Ultimately, this results in a sort-of splitting failure in the fractured block, driven by the unfractured block. A good example of this mechanism is T44S15 (see Figure 4.3).
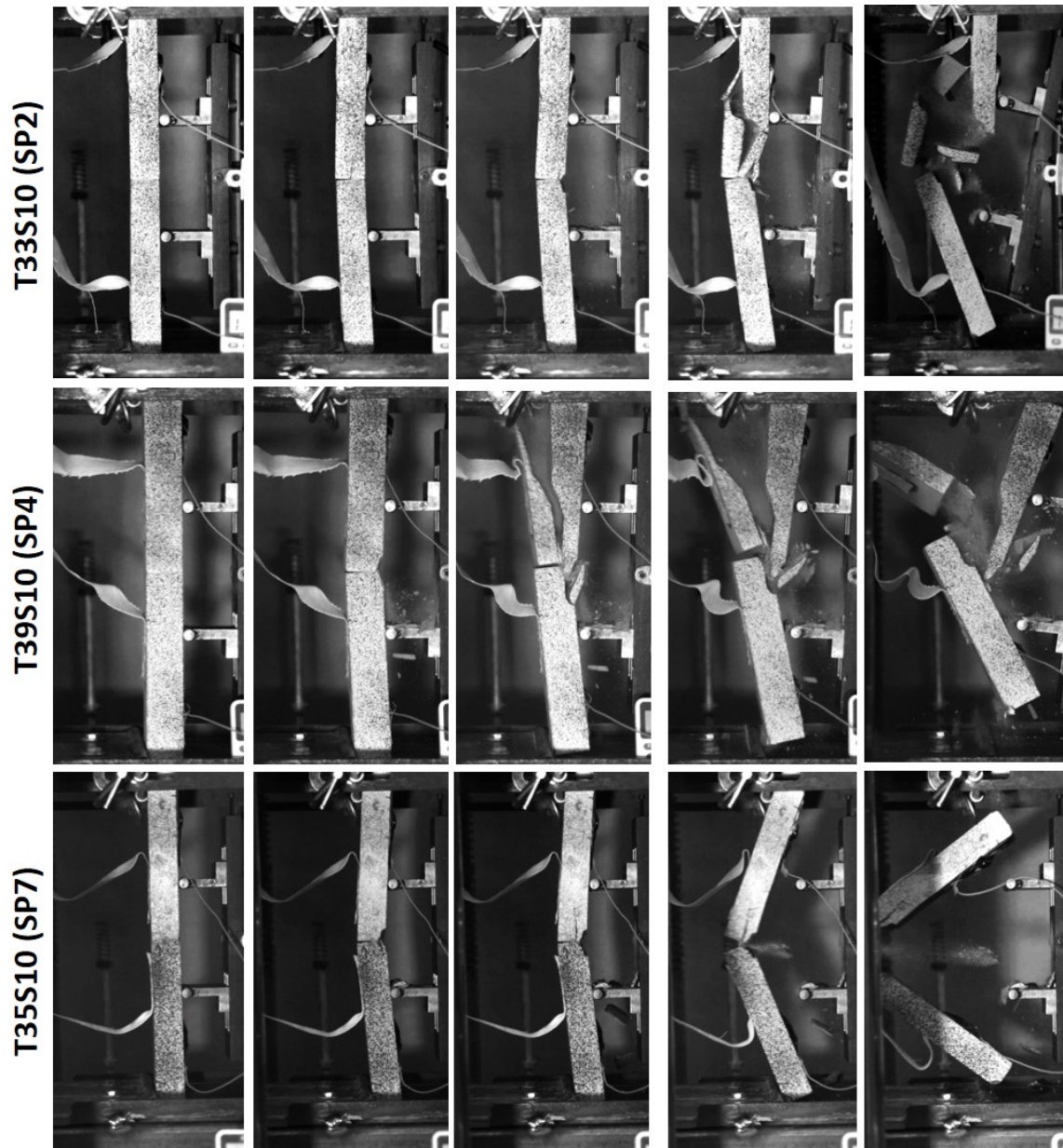
Figure 4.2: Wallace sandstone THB laboratory tests progression conducted under $\sigma_a = 10$ MPa confinement (Images have been modified to increase contrast).
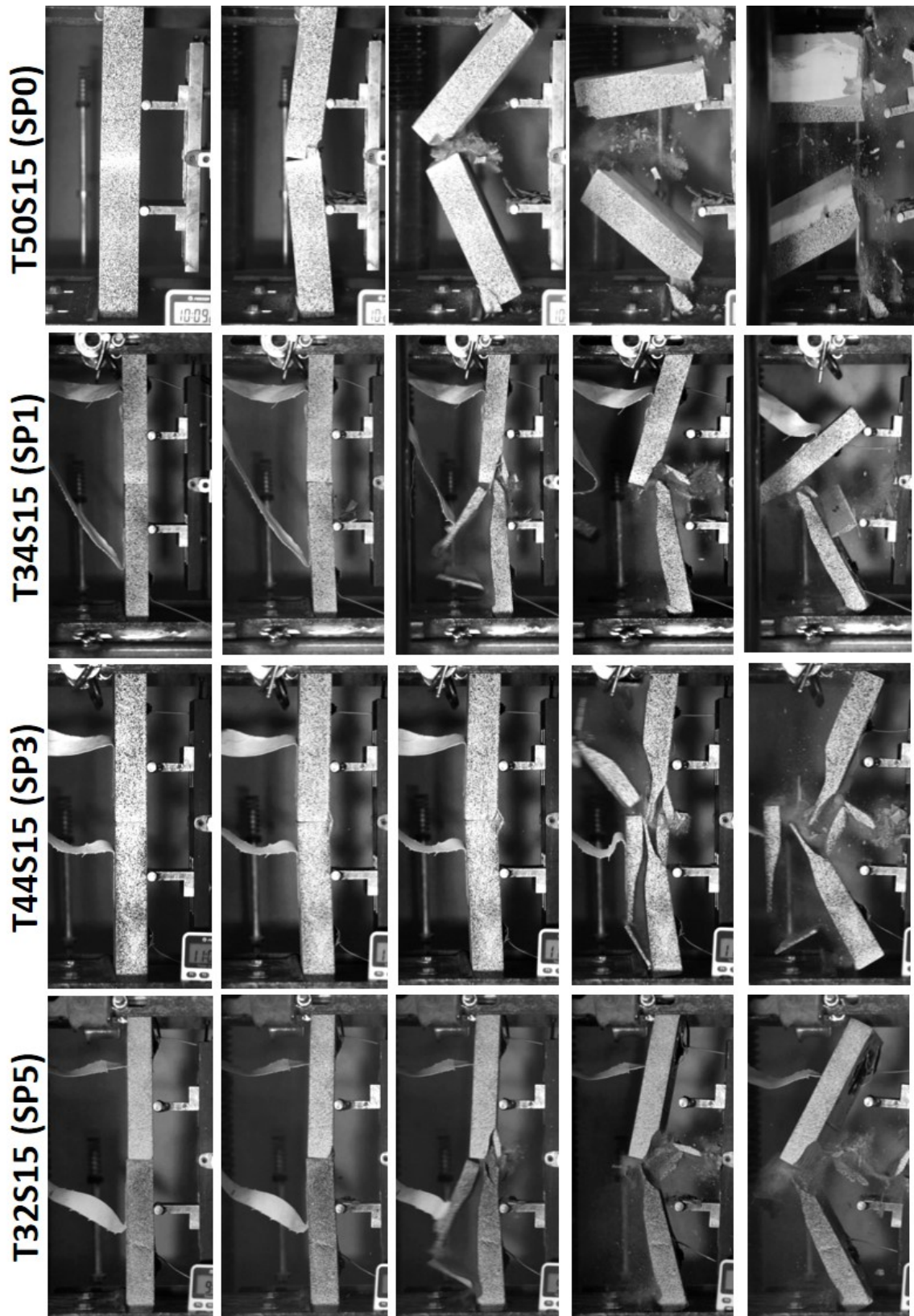
Figure 4.3: Wallace sandstone THB laboratory tests progression conducted under $\sigma_a = 15$ MPa confinement (Images have been modified to increase contrast).

Figure 4.4 shows the fractures pattern captured via high-speed camera at the moment that specimens were about to rupture. These images revealed that, generally, fracture formation and damage accumulated within the central hinge zones. However, frequently an axial fracture formed that propagated into one, or both of the blocks. The ultimate rupture involved a complex combination of crushing and unstable fracture growth which sometimes even transected the block. Variability and the presence of microdefects likely played a role in this. Test T50S15 was unique in the localization of fracturing within the hinge zone due to formation of a fracture on a likely pre-existing flaw early on in the test progression.
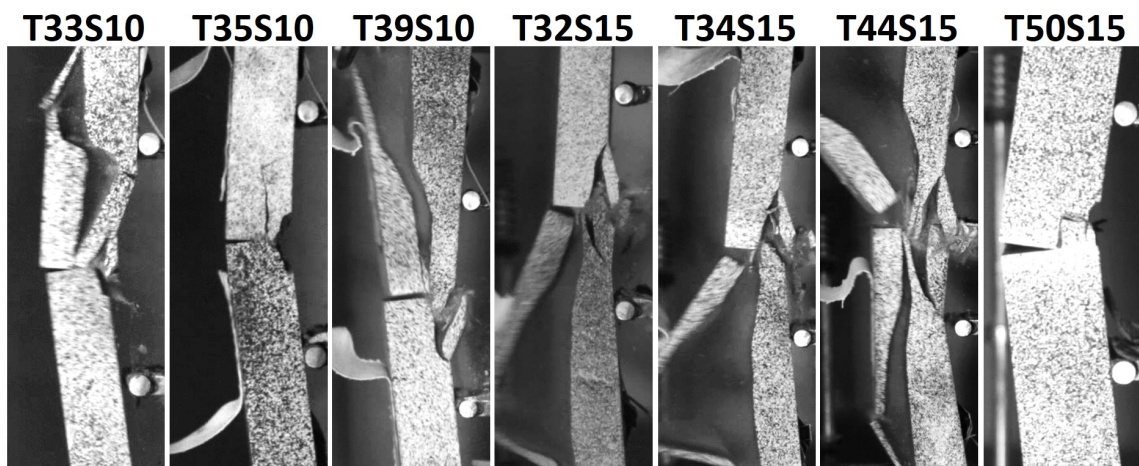
Figure 4.4: Images obtained from the high-speed camera, showing the fractures pattern for each THB experiment just before failure (Images have been modified to increase the contrast).

Similarly to other buckling tests, the plot of δ_l vs P_l seems to capture the characteristic behaviour of the THB test most appropriately. Figure 4.5 shows seven $\delta_l - P_l$ plots from the THB experiments. There are clear similarities in the characteristic behaviour of most of the tests. As can be seen, the $\delta_l - P_l$ curves consisted of three

main regions: (1). linear region, (2). nonlinear part consists of fracture initiation and load increasing (yield region), (3). decreasing load until the complete rupture occurs (failure region). These stages are illustrated conceptually in the inset figure of Figure 4.5 and are labelled directly on the curves. Although there is not always a clear demarkation of the onset of each stage, the three regions of the $\delta_l - P_l$ curves where demarked by yield, peak, and rupture. Correspondingly, subscripts y, p and r are appended to the load and displacements values to indicate these points (e.g., δ_{ly}, δ_{lp} and δ_{lr}). Although often these points are fairly clear to identify, some judgement was required. A summary of the test results is provided in Table 4.3. The dimensionless ratio T/L was used to normalize the test data to allow for comparison with the findings from other buckling studies, such as Diederichs and Kaiser (1999).

Table 4.3: Summary of test results and pertinent parameters from the Wallace sandstone THB experiments

Test ID	T/L	σ_a (MPa)	Yeild		Peak		Rupture		
			P_{ly} (KN)	δ_{ly} (mm)	P_{lp} (KN)	δ_{lp} (mm)	P_{lr} (KN)	δ_{lr} (mm)	δ_{lar}* (mm)
T39S10	0.20	10	13.4	1.4	18.1	4.2	17	6.2	11.1
T35S10	0.18	10	13.5	3.1	13.8	4.2	4.0	10	10.3
T33S10	0.17	10	10.9	1.9	12.4	3.3	10.4	6.9	8.7
T50S15	0.25	15	25.8	2.9	34.1	5.1	33.7	5.6	8.7
T44S15	0.22	15	27.5	2.8	29.0	4.0	27.7	5.2	9.1
T34S15	0.17	15	16.8	2.3	18.6	3.1	16.8	5.5	5.7
T32S15	0.16	15	15.1	2.1	16.8	3.1	16.0	4.9	5.1

* The apex displacement obtained using the DIC method.

The $\delta_l - P_l$ curves for all of the tests, except the two thickest, conducted at $\sigma_a =$ 15 MPa (T44S15 and T50S15) had very similar characteristic responses that seemed
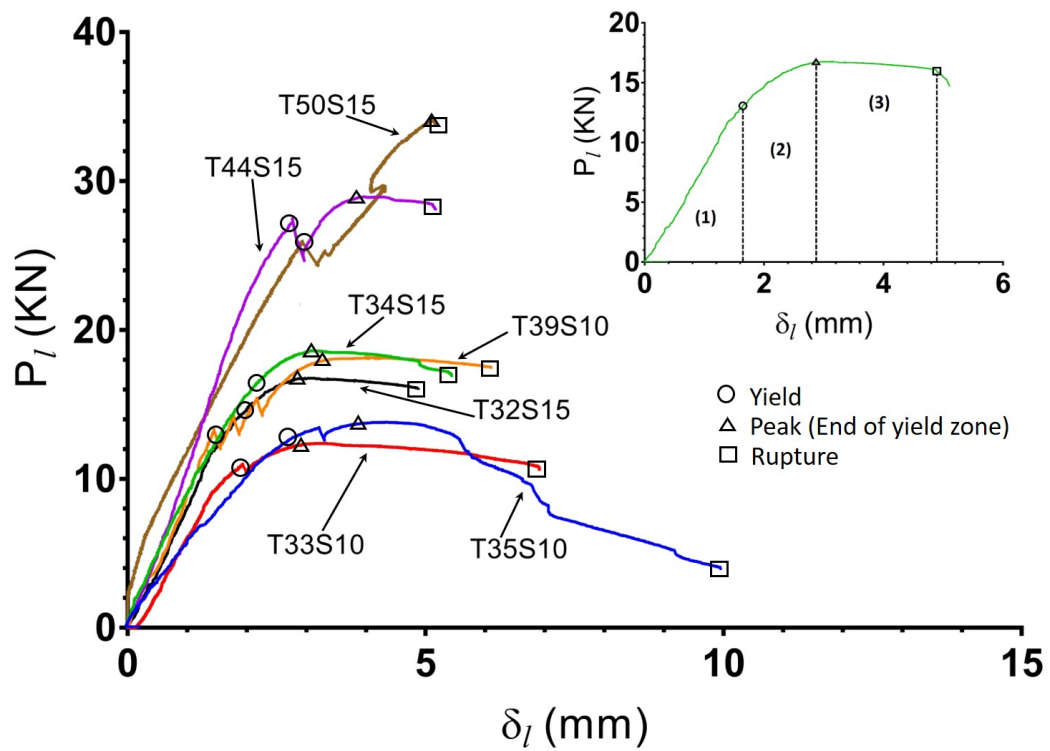
Figure 4.5: Lateral load vs lateral displacement curves obtained from the seven THB experiments carried on Wallace sandstone. They key thresholds are indicated by symbols

relatively ductile. Yield occurred approximately 90% of the peak ($P_{ly} \approx 0.9 P_{lp}$) followed by a relatively ductile displacement until ultimate rupture occurred (P_{lr}). In contrast, tests T44S15 and T50S15 on the thicker specimens, showed a brittle response with increased P_l required to achieve peak and rupture after yield ($P_{ly} << P_{lr}$). This implies that there is some transition from ductile to brittle response based on the thickness and clamping stress. However, there are not enough tests in the study to clearly identify this transition or to clearly identify which parameters to attribute to the transition. Test T35S10 showed by far the most displacement to rupture (with some loss of resistance capacity). As shown in the images in Figure 4.2 this specimen exhibited the most classic form of THB with failure mostly confined to the crushing zones hinge regions. In many other cases, failure was initiated by propagation of a long fracture from the crushing zone into the block.

The AE system was used for six of the experiments (all but the first test on specimen T50S15) to capture the number of cracks (AE hit count events) during test evolution until rupture occurred. Details of the system, sensors and software were provided previously in the Methodology section. Each test duration varied somewhat, but was approximately 10 to 15 minutes in total. In order to make the AE data easily comparable between tests, *InSight* software was used to 'scale' the test time. The time span for all experiments was considered equal to 1000 seconds (i.e., the true, real time is scaled over 1000 'imaginary' seconds). The AE results in Figure 4.6 show AE event frequency and cumulative frequency for each of the THB tests where AE was recorded. Figure 4.7 shows the cumulative AE events for the

tests at failure and yield. In general, there was a gradual increase in AE events with a rapid rise coinciding with yield. Following yield there was a general reduction in AE events, although with significant variability between tests, until a rapid increase corresponding to rupture. Although this trend was fairly consistent between tests, there was significant variability in the number of AE events between tests.
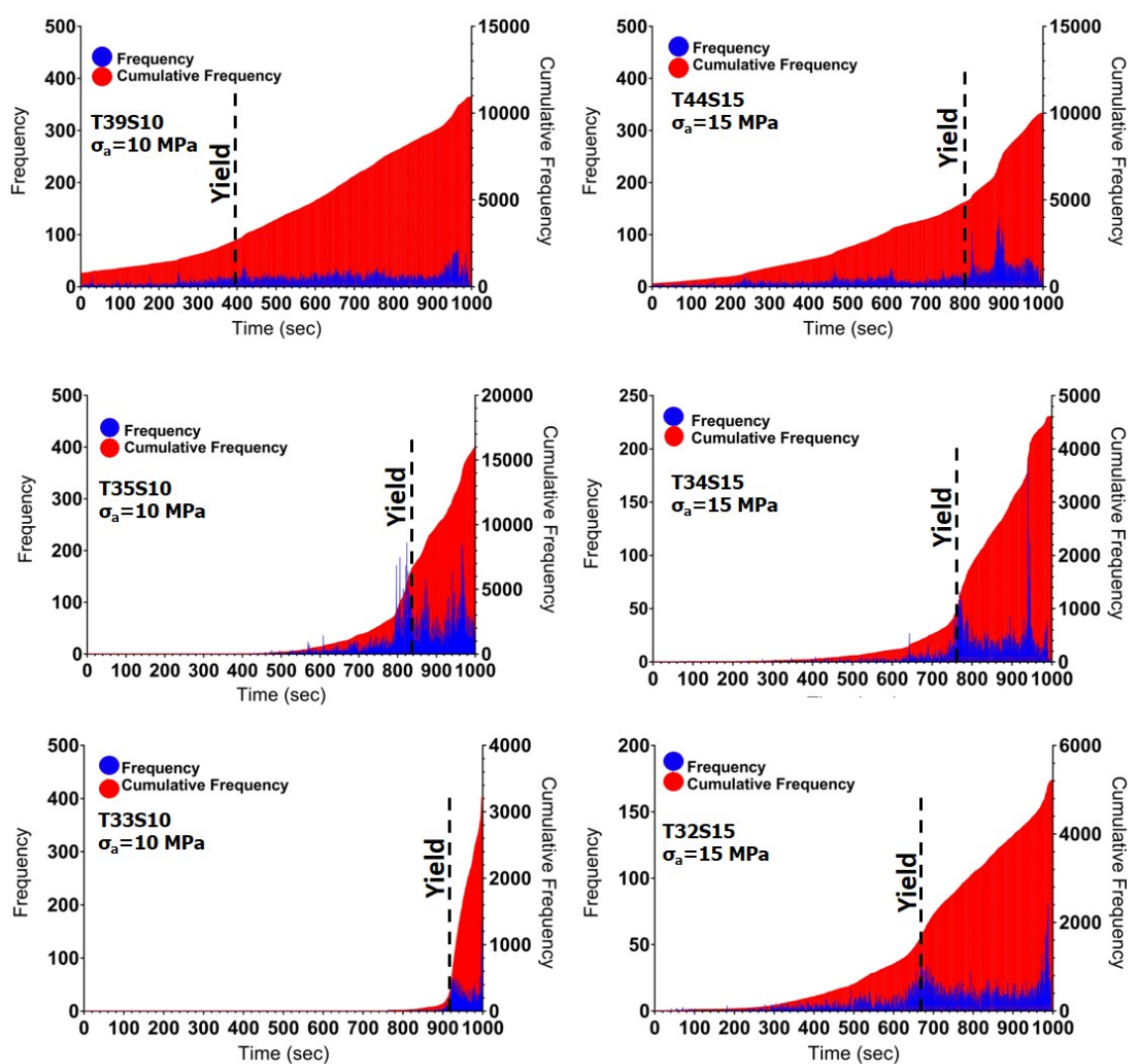
Figure 4.6: AE results showing the frequency and cumulative frequency of crack events during the entire THB experiments. Note that the vertical axis scales vary to improve visibility.
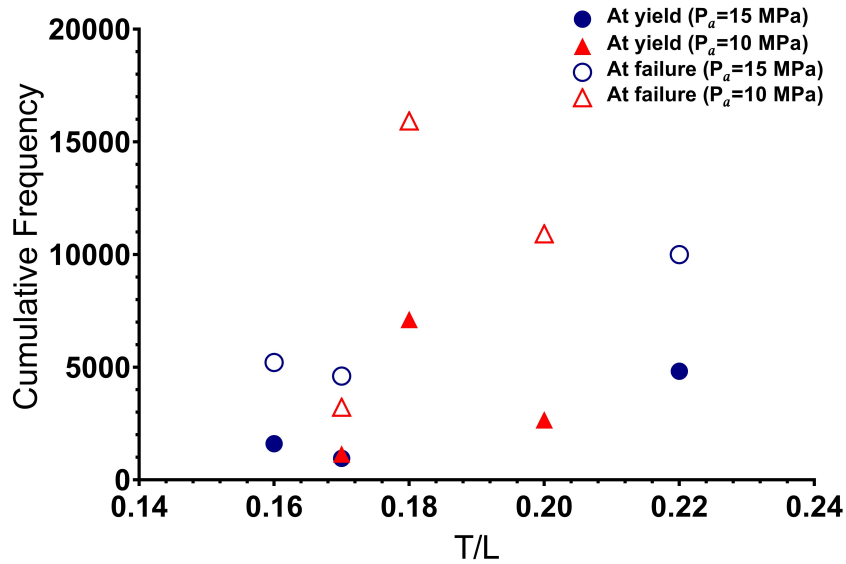
Figure 4.7: Cumulative frequency of AE events at yield and rupture during THB experiments versus T/L ratio

Figure 4.8 shows the T/L versus peak lateral loads (P_{lp}) for all experiments grouped by σ_a. The data trends are consistent within groupings and based on the plot a linear relation exists with strong, positive correlation. The linear regression equations for each value of σ_a are provided in Eqs. 4.1 and 4.2. The equations have nearly identical slope but are offset by approximately 6.5 kN in the P_{lp} axis intercept. It would require testing under a larger range of σ_a values to explore the change of P_{lp} with σ_a more fully and the trends presented here are valid only for the range of data presented.

$$P_{lp} = 195(T/L) - 21 \text{ for } \sigma_a = 10 \text{ MPa} \tag{4.1}$$

$$P_{lp} = 195.6(T/L) - 14.5 \text{ for } \sigma_a = 15 \text{ MPa} \tag{4.2}$$
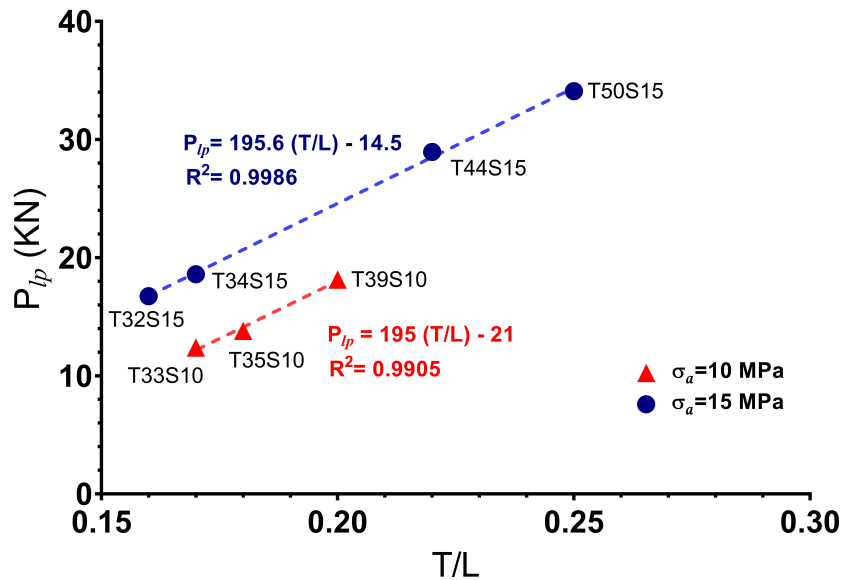
Figure 4.8: Peak lateral load (P_{lp}) versus T/L obtained from THB experiments and linear regression lines for both $\sigma_a = 10$ and 15 MPa.

Displacement trends for the tests were explored in several ways. Plots of δ_{ly} and δ_{lr}, normalized to L, are shown in Figure 4.9 and the differential value $(\Delta\delta_l = \delta_{lr} - \delta_{ly})$ is plotted in Figure 4.10. The values are plotted against the T/L ratio in these plots. The data shows a clear trend with peak achieved at approximate $0.1L$ consistently for both series. Rupture occurs more closely to peak for the the $\sigma_a = 15$ MPa series than for the $\sigma_a = 10$ MPa series, implying that higher confinement results in an decrease in the ductile response (i.e., more brittle). As T increases, there is also a clear trend of decreasing $\Delta\delta_l$ also implying decreasing ductile behaviour with greater thickness. Specimen T35S10 is markedly greater δ_{lr}, as shown in the $\delta_l - P_l$ curves. As discussed earlier, this specimen experienced almost pure compression failure in the hinge zones leading to rupture.

The values of δ_l were directly measured during the test and were thus the focus

of the data analysis. However, the displacement of the apex (δ_{la}) is probably the most meaningful measure, although it was obtained indirectly from the test. The normalized values of δ_{la}/L at rupture obtain from the DIC images is plotted versus T/L in Figure 4.11. Similarly to the δ_l plots shown earlier, there are clear trends within each σ_a series and, as expected, the $\sigma_a = 15$ MPa series reaches rupture at a lower displacement than the $\sigma_a = 10$ MPa series. This plot allows for comparison with field observations of displacement at failure and also with other studies and analyses found in the literature. For example, based on analysis Diederichs and Kaiser (1999) stated that buckling failure would typically occur at $\delta_{la}/L = 0.1$. The THB test results show greater values of δ_{la}/L at rupture than 0.1, but the values are reasonably close to the theoretical-based prediction. Based on the photographic images, the THB failure mode can be somewhat variable and complex internally resulting in differentiation from theoretical predictions.
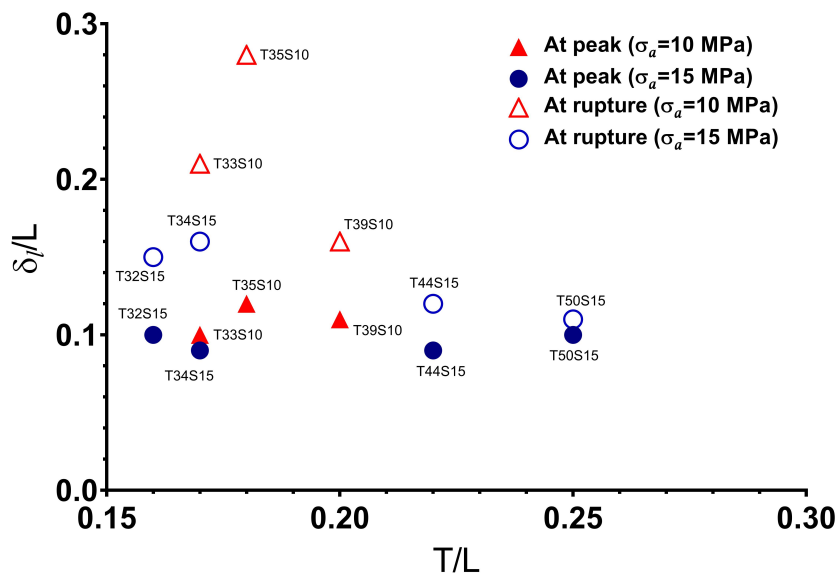
Figure 4.9: Comparison of δ_l/L ratio at yield and failure for $\sigma_a = 10$ and 15 MPa.
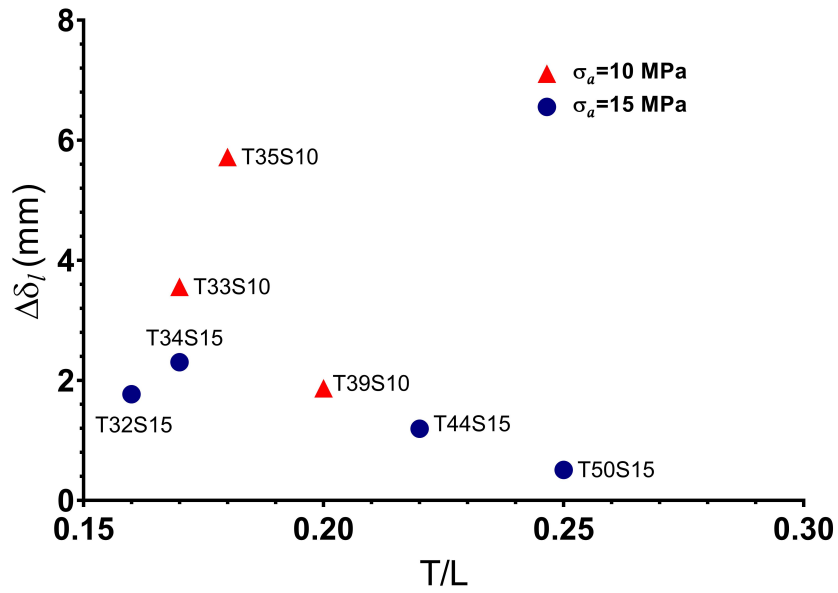
Figure 4.10: Variation of failure stage displacement respect to T/L ratio at 10 and 15 MPa confinement.
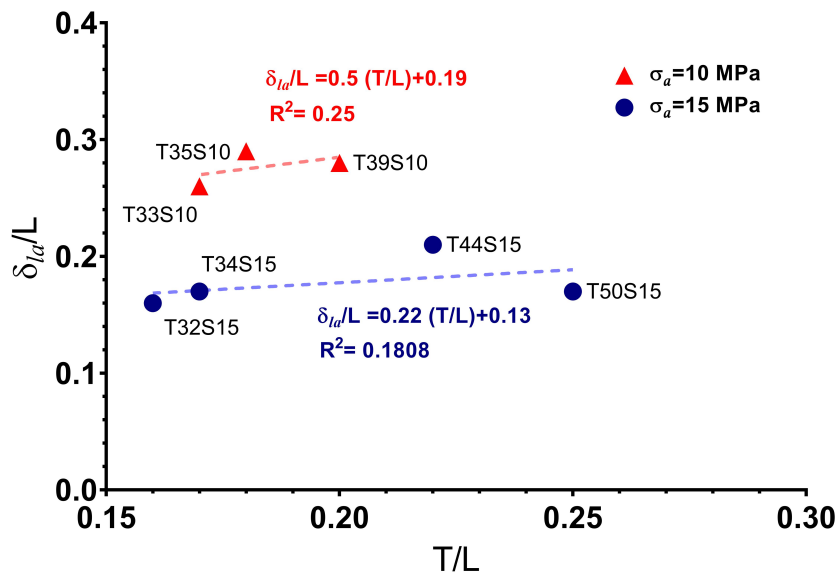
Figure 4.11: Apex ratio at rupture obtained using the DIC method from the images captured using the high-speed camera at $\sigma_a = 10$ and 15 MPa.

4.4   Analytical Approach

The rigid arching analysis method in masonry structures is similar to THB con-figuration conducted in this study, which occurs when a masonry wall is built with a tight, rigid, lateral contact. The method was used to provide some comparative insight into the THB experiment results. When a lateral load is applied to the wall a compressive force is induced due to the bending. The induced compressive force causes arching of the wall and cracking at the supports and center (midspan) of the wall. The clamping forces will be created when the wall pushes against the supports with an increase of the lateral load. As a result of increasing clamping forces, a three hinged arch is developed at the locations where the internal couple resisted the cre-ated external moments. The proposed aching theory by McDowell et al. (1956) for masonry walls assumes that the supports are rigid and the materials have an ideal-ized stress-strain relationship (Drysdale and Hamid, 2005). Based on this theory, the lateral peak stress, σ_{lp}, can be calculated by taking a moment at the point (a), as shown in Figure 4.12, using the Eq. 4.3:

$$\sigma_{lp} = \frac{2C}{L^2}(\gamma T - \Delta_{lp}) \tag{4.3}$$

Where L is the length of the specimen, T is the specimen's thickness, γ is a factor related to compression zone size (the thickness of the blocks' interface that is not in contact at failure), Δ_{lp} is apex displacement at the peak load, and C is
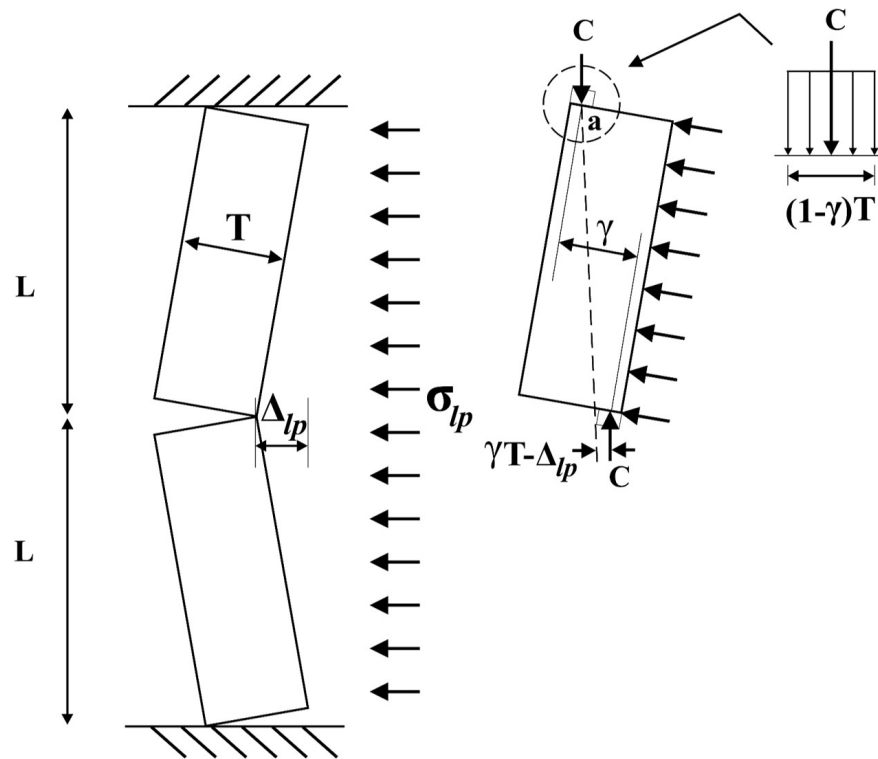
Figure 4.12: Three hinge arch with deflection method modified to use for THB analysis (modified after Drysdale and Hamid (2005))

.

the compression force per unit length within the crushing zones calculated using the

Eq. 4.4:

$$C = \Phi_m \sigma_c (1 - \gamma) T \tag{4.4}$$

Where σ_c is the unconfined compressive strength of the masonry block, and Φ_m

is the resistance factor applied to the specimen (or strength reduction factor).

Due to the dependency of the compression zone to the wall geometry and stress

levels, it was assumed that the compression zone is a factor of thickness, i.e. $(1-\gamma)t$.

The THB experiments showed that the average thickness of the compression zone in

Wallace sandstone was 1/3 of the specimens' thicknesses. Therefore, the γ factor was

considered as 0.67. Also, it was assumed that the stress over the compression zone is

equal to the $\sigma_c = 82$ MPa for Wallace sandstone.

Another critical factor that should be explicitly identified for rocks is selection of

Φ_m. For initial calculations it was assumed that $\Phi_m = 1$ to calculate the peak lateral

loads (P_{lp}) predicted and compare them with actual results, which are presented

in Table 4.4. The calculated P_{lp} values show that there is considerable difference

between the experimental and analytically-calculated values of the P_{lp}. These errors

show the importance of the Φ_m factor in the calculation of peak lateral loads. The

peak lateral load P_{lp} was obtained from the calculated σ_{lp} in Eq. 4.3 considering it as

a simple rectangular stress. Values of Φ_m that reproduce the THB test results were

back-calculated based on the P_{lp}. Table 4.4 presents the analysis's summary data to

back-calculate the Φ_m.

Table 4.4: Summary of the analysis were carried out using the three hinge arching theory to calculate the peak lateral load and the back-calculated resistant factor

Test ID	T/L	σ_a (MPa)	Δ_{lp} (mm)	P_{lp} experimental (kN)	P_{lp} calculated (with $\Phi_m{=}1$) (kN)	$\Phi_m{}^*$
T33S10	0.17	10	5	12.4	30.5	0.41
T35S10	0.18	10	6.3	13.8	32.4	0.43
T39S10	0.20	10	6.4	18.14	41.7	0.43
T32S15	0.16	15	4.7	16.75	29.1	0.58
T34S15	0.17	15	4.7	18.6	33.3	0.56
T44S15	0.22	15	6	28.95	55.9	0.52
T50S15	0.25	15	7.7	34.1	70	0.49

* Φ_m back-calculated to achieve the P_{lp} experimental.

The back-calculation of the resistance factor showed that Φ_m could be divided to three categories: (1) $\Phi_m = 0.4$ for $\sigma_a = 10$ MPa, (2) $\Phi_m = 0.5$ for T/L >0.2 and $\sigma_a = 15$ MPa, (3) $\Phi_m = 0.6$ for T/L <0.2 and $\sigma_a = 15$ MPa. The obtained results for Φ_m showed that besides dependency on the material properties, it depends on the axial confinement and thickness of the blocks for the THB experiment. Although the back-calculated Φ_m could be used to calculate the peak lateral load, the different boundary condition assumptions (i.e. did not take the axial confinement into account) could raise a question about the validity of this analysis method for THB. Therefore, a wide range of THB experiments is required with different rock types, geometries and axial confinements for the sensitivity analysis of the Φ_m. One of the objectives of the study is to determine if σ_c or σ_{ci} is a better predictor of THB behaviour. Typically σ_{ci} is in the range of 1/3 to 2/3 σ_c which is consistent with the values of Φ_m observed implying that σ_{ci} may be a better predictor of THB behaviour.

4.5   Numerical Modelling

A numerical modelling program was conducted as part of the study to simulate the THB experiment. The objective was to develop a suitably-calibrated model that could capture the main features of the experiment, such as the buckling process, crack initiation and growth, and stress distribution for entire THB testing process. Therefore, the commercial *UDEC* software using its Voronoi tessellation feature was used to simulate the behaviour of rocks, commonly referred to as a grain-based modelling (GBM). *UDEC* is a two-dimensional distinct element software code that uses a distinct element method introduced by Cundall (1971) for discontinuum modelling in rock engineering. This code can simulate the discontinuous nature of rock, like a jointed rock mass, under either dynamic or static loads. Also, a powerful programming language, called *FISH*, is incorporated into the software. *FISH* is inherent within *UDEC*, which allows the user to develop personalized functions to improve the efficiency of the *UDEC*. This simulation aims to model a simple THB failure using the recent Voronoi tessellation technique to capture the brittle behaviour of the rock.

4.5.1   Modelling Methodology

The first step of the modelling program was parameter calibration using the experimental data obtained from the UCS tests on Wallace sandstone. It is important that the Voronoi tessellation of the calibration model (UCS test) be similar to the dimensions of the final THB model. A Voronoi block model simulating the UCS experiment with a dimension of 5×5 cm and with a typical Voronoi block diameter

of 2 to 3 mm and zone size of 1 mm was conducted to calibrate Wallace sandstone's macro-mechanical properties (σ_c and E). Because the UCS test was conducted via a vertical velocity boundary condition (i.e., as if frictionless platens), a square model geometry produces equivalent results to using the true UCS geometry (i.e., 2:1 dimension ratio). The Voronoi block model's contact properties were varied by trial and error to match with the stiffness and strength of the Wallace sandstone; however, the calibration approach used by Damjanac and Group (2008) was utilized as a guideline (e.g., maintaining a consistent ratio of c_j to t_j). In this approach, it was assumed that the Voronoi blocks were infinitely strong, and the strength of the overall model was derived from the grain interfaces ('joints') within the structure. In contrast to this, the model stiffness was derived from the Voronoi blocks (and subsequent finite difference zones), and the joints were extremely stiff (no compliance derived from the joints). The calibrated modelling parameters that reproduce Wallace sandstone's properties are presented as BU1 in Table 4.5. The Young's modulus and σ_c obtained from this model were in good agreement with the experiment data. The model's Young modulus and σ_c were 24.6 GPa and 82.1 MPa, which the experimental data was 24.6 GPa and 82 MPa, respectively. Figure 4.14 shows the axial strain-stress curve of the calibrated UCS test modelling. As discussed in the Modelling Results section, two other sets of micro-mechanical properties (BU2 and BU3) were also used (Table 4.5), and the results are also plotted (Figure 4.14).

The THB model geometry was nearly an exact replica of the experimental setup,

Table 4.5: Calibrated contact properties to match macro-mechanical properties of Wallace sandstone

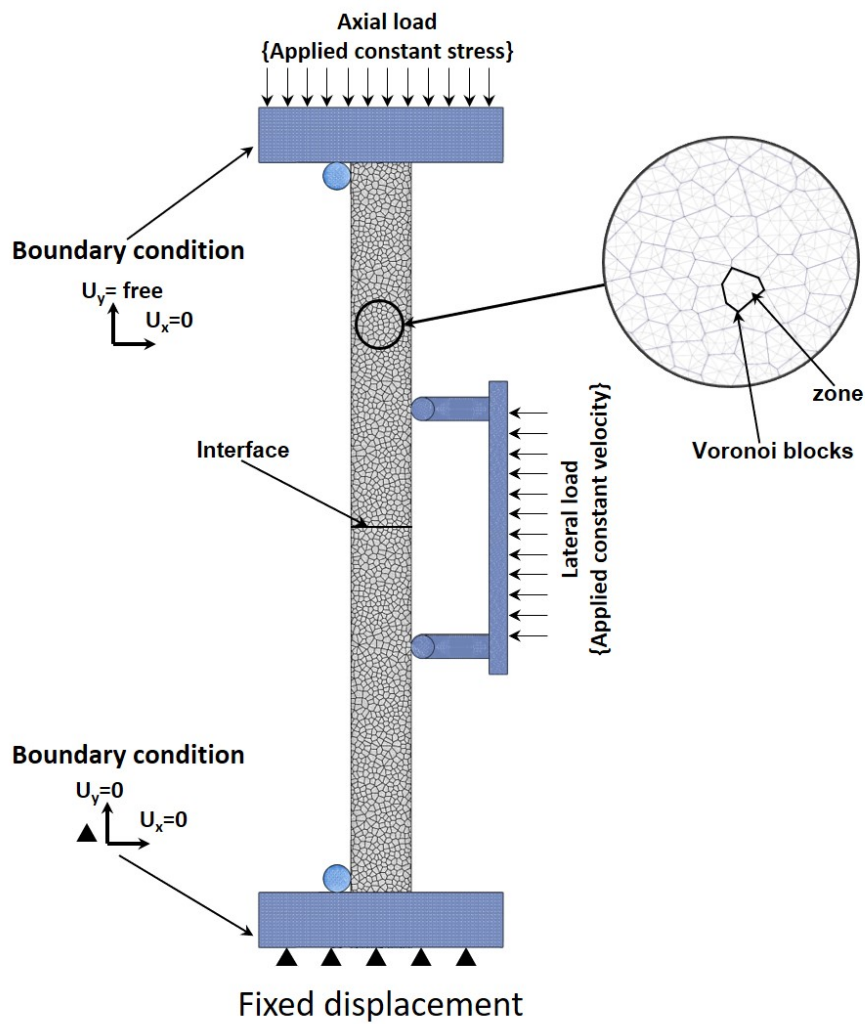| Parameter ID	K (Pa)	G (Pa)	c_j (Pa)	ϕ_j (°)	t_j (Pa)
BU1	22×10^9	17.1×10^9	36.5×10^6	32	14.6×10^6
BU2	11.8×10^9	7.08×10^9	36.5×10^6	32	14.6×10^6
BU3	11.8×10^9	7.08×10^9	36.5×10^6	32	29.2×10^6

Figure 4.13: *UDEC* Voronoi block model setup for simulation of the THB test T33S10 experiment on Wallace sandstone
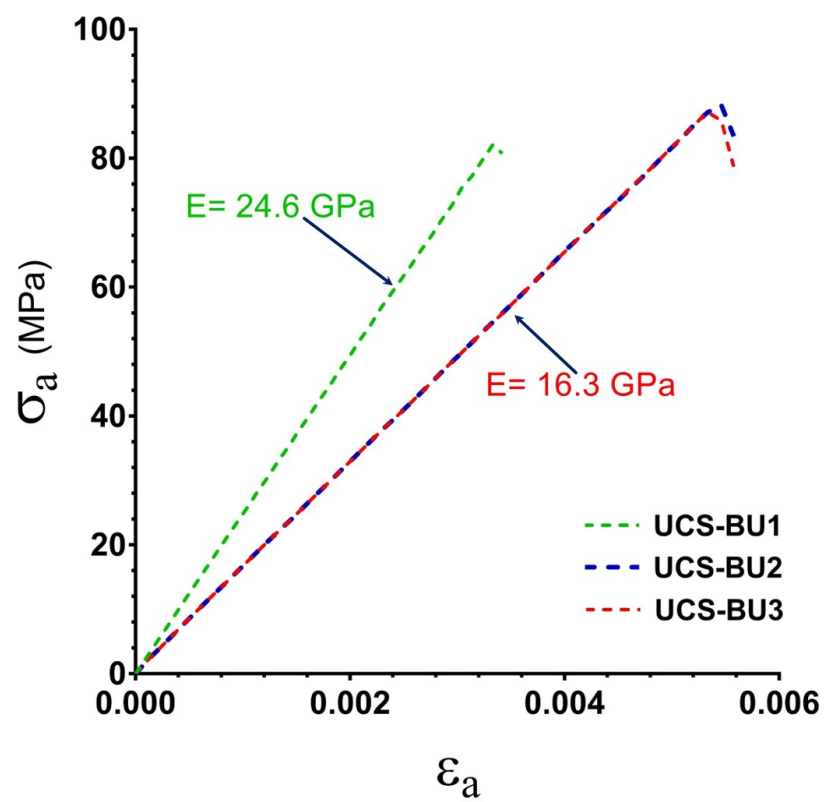
Figure 4.14: UCS tests data obtained from calibrate *UDEC* Voronoi block model for Wallace sandstone

including the vertical and lateral platens. The geometry of the numerical model is shown in Figure 4.13. The THB experiment was simulated using two blocks with a the dimension of test T33S10: $L = 20$ cm, $W = 10$ cm, and $T = 3.3$ cm. Test T33S10 was selected for simulation because it had a very well-behaved response, indicating minimal influence from various geological micro-defects or flaws. The Voronoi blocks and internal finite difference zone dimensions were the same as the UCS calibration model resulting in approximately 12 blocks across the model thickness.

The Wallace sandstone's calibrated contact properties (Table 4.5) were used to simulate the simple THB experiments carried out in this study. The inter-block interface stiffness values (K_n and K_s) were simplified to be the same as the Voronoi block interfaces. Although these values are unrealistically high, it should have minimal impact on the test results, which are dominated by internal block stiffness and fracturing. Inter-block strength values of $c_j = 0$, $\phi_j = 32°$, $t_j = 0$ were used which are suitable for typical sandstone saw-cut joints. The loading platens (i.e. axial and lateral), lateral restrained bars, and base platen were simulated by assigned high stiffness and elastic behaviour to the zones. The rock-platen interfaces had zero strength and extremely low frictional strength ($\phi = 3°$).

The boundary condition of the model was similar to the THB experiment as shown in Figure 4.13. The THB test was simulated in stages, similarly to the real experimental methodology. First, constant axial stress was applied to the upper platen and kept fixed during the buckling phase. The model was cycled until the model reached the equilibrium state based on the applied boundary conditions. The

two lateral restrained bars used in the actual experiment were also modelled and located at the specimen's front top and bottom to prevent the block sliding. The lateral platen was also modelled identical to the lateral platen. In the second phase, the lateral load was applied to lateral platen using a velocity boundary condition at the rate of 1×10^{-5} m/s. This low boundary velocity was chosen to keep the model in a quasi-static equilibrium state throughout the simulation. The model was then cycled until the amount of δ_l reached the actual value observed in the THB experiment. The model's stresses and displacements were monitored using the pre-defined history functions and customized *FISH* codes that were programmed to capture the 'histories' (i.e., saved to UDEC-allocated computer memory) of different parameters in the model.

4.5.2   Modelling Results and Discussion

Figure 4.15 shows the comparison of δ_l - P_l graphs between the THB numerical simulations using the *UDEC* code and the experimental results of the test T33S10 on Wallace sandstone. Images of the test and simulation at various stages of test progression are shown in Figure 4.16. The initially-calibrated model, or base model (BU1), showed a fairly similar characteristic response trend based on δ_l - P_l but with some deviation in magnitudes. The BU1 model showed a steeper linear region, followed by a lower first fracture at yield, and higher peak and rupture loads. In general, the mean calibrated parameters reproduced the test fairly well.

Although the Wallace sandstone was selected because of its consistency, as shown
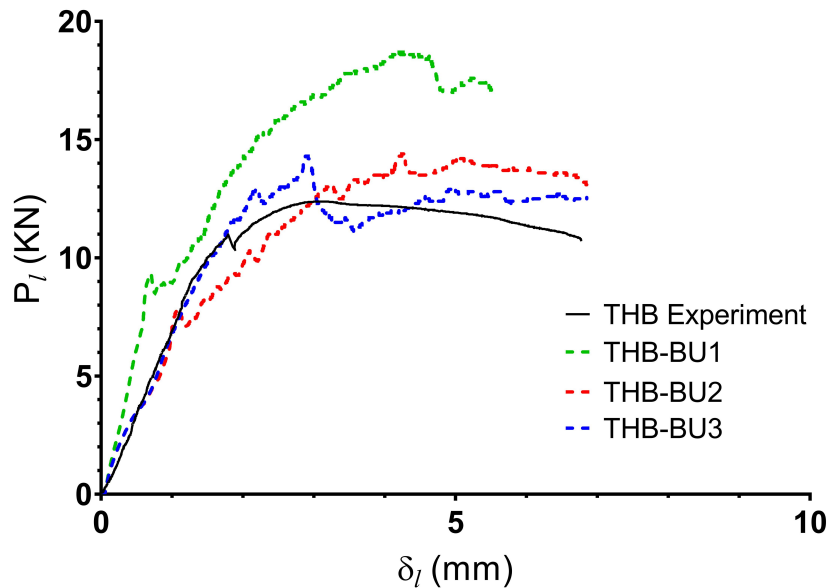
Figure 4.15: Lateral load versus lateral displacement obtained from numerical THB tests compared with the THB results obtained for the test T33S10. The numbers in the image indicates (1) linear region, (2) yield, (3) peak, and (4),(5) post-peak of THB test process

in Table 4.1, there is clearly some variation in σ_c and E among specimens, and it is unsurprising if the specimens T33S10's parameters deviated somewhat from the mean values for which the model was calibrated. A reduced stiffness model (BU1), based on the stiffness of UCS-6 (Table 4.1) was used. The model response in the linear range was improved in this model, but yield occurred much lower, although P_{lp} was also improved. The model parameters could also have been calibrated directly to the THB experimental results and subsequently the parameters of the test specimens (e.g., σ_c of specimen T33S10).

In Figure 4.16, the fracturing progression for BU1 and BU2 both show in initial fracture forming near the middle of the inter-block interface, corresponding to yield.

Figure 4.16: Images showing fracturing for progressive stages of the THB experiment and numerical simulations for T33S10. The numbers indicate: (1) linear region; (2) yield; (3) peak; and (4),(5) post-peak

However, these models both show significant development of a tensile fracture opposite the lateral platens due to block bending. Although there is evidence that some damage may occur in some of the specimens near the platens in th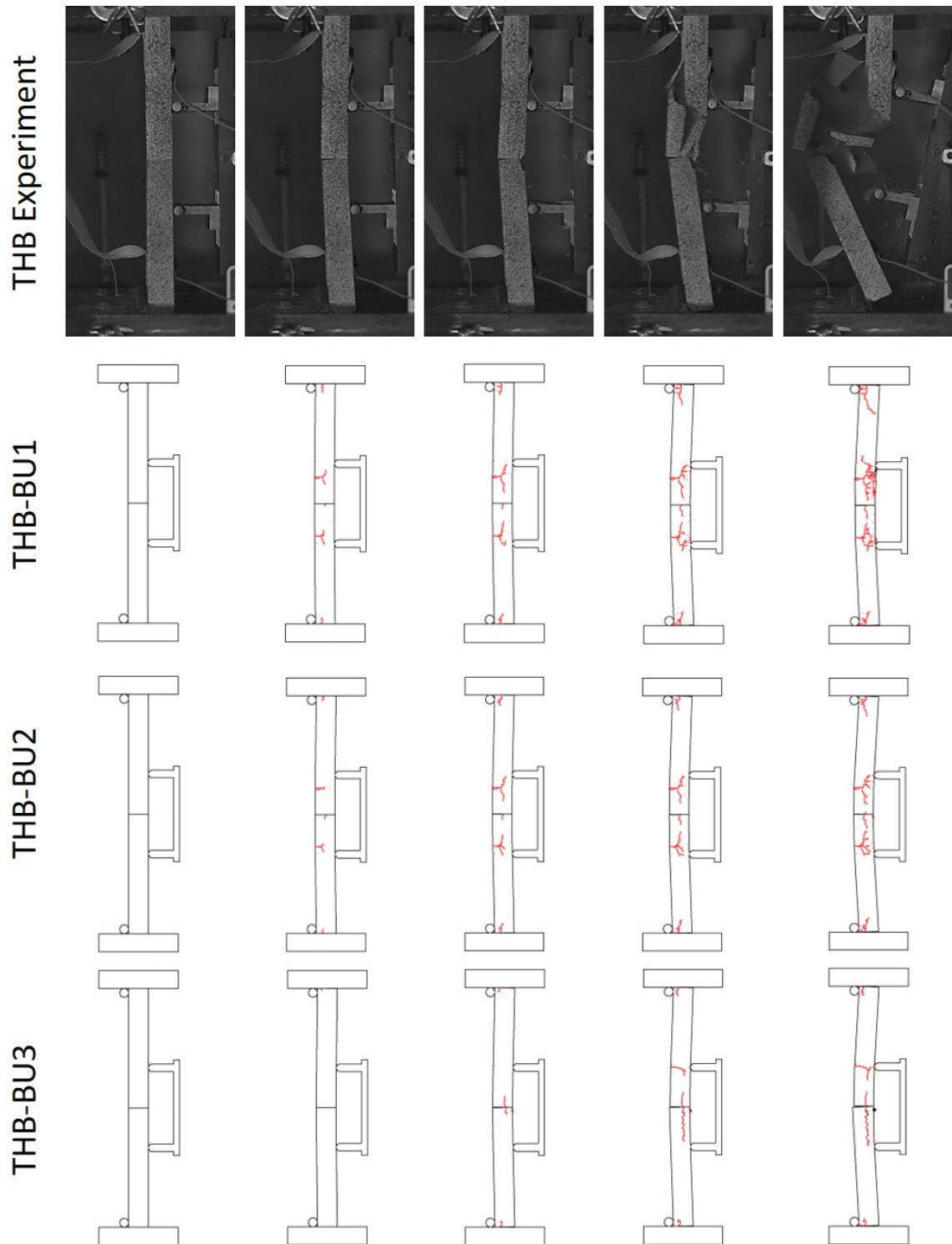e real experimental tests, they do not show any influence on the test until at, or near, rupture. This impact is accentuated in the numerical simulations. This may be due to many factors, such as Voronoi block geometry (i.e., block size), calibration of a multi-parameter model, or other issues within the software (e.g., contact models). In order to explore a relatively simplistic parameter variation to limit tensile fracturing to better match the observed experimental test response, the t_j was doubled in BU3. The UCS calibration models for BU2 and BU3 are shown in Figure 4.14 which reveals that t_j has negligible impact on the simulate σ_c.

As shown in Figure 4.15, BU3 parameters resulted in a good match to the observed T33S10 test in both the load-displacement response and fracture formation. Figure 4.16 shows initial fracturing at all of the hinge points (crushing zones), which extended. This model still shows damage accumulating in the upper block on the face opposite the lateral platen. Ultimately, although the model simulations show some deviation with actual test behaviour, the model captured the overall behaviour well and provided significant insight into the test. More detailed calibration and more extensive parametric study of both properties and Voronoi block geometry, would further refine the model. One insight is that although significant fracturing at the lateral platens was not observed in the experimental tests, perhaps the test setup should be revised to reduce tensile stresses in this region by adding additional lateral

platens (e.g., 4 instead of 2).

In order to compare the simulated behaviour of a single block under the same loading conditions versus the two-block system, a numerical simulation was carried out identically to the THB configuration with a single block. Figure 4.17 shows the P_l - δ_l of the single block simulation versus THB experiment and numerical modelling. The results show that the overall behaviour trend is fairly similar; however, the single block model yielded at a lower lateral load compared to the THB experiment and simulation ($P_l \approx 8$ kN). The reason for this early failure is that the failure mode of the single block is bending failure at two locations, while the THB is a buckling failure mode. In bending, the tensile stress can transmit through the specimen. Therefore, in a single beam bending, both compression and tensile zone exist. While in THB, blocks are separated at the center, and there is no tensile stress transmission through the blocks. Therefore, there is only a compression zone at the hinge locations. Also, in contrast to the THB experiments and corresponding numerical modelling, no vertical fractures were observed at the mid-block location at the inter-block interface.

4.6   Conclusion

The recently-developed THB test was conducted on a series of Wallace sandstone block specimens over a range of thicknesses (T) and for two levels of clamping stresses (σ_a of 10 and 15 MPa). The tests were monitored with conventional load and displacement devices and also using high-speed digital video imaging with DIC methods, and an AE system.
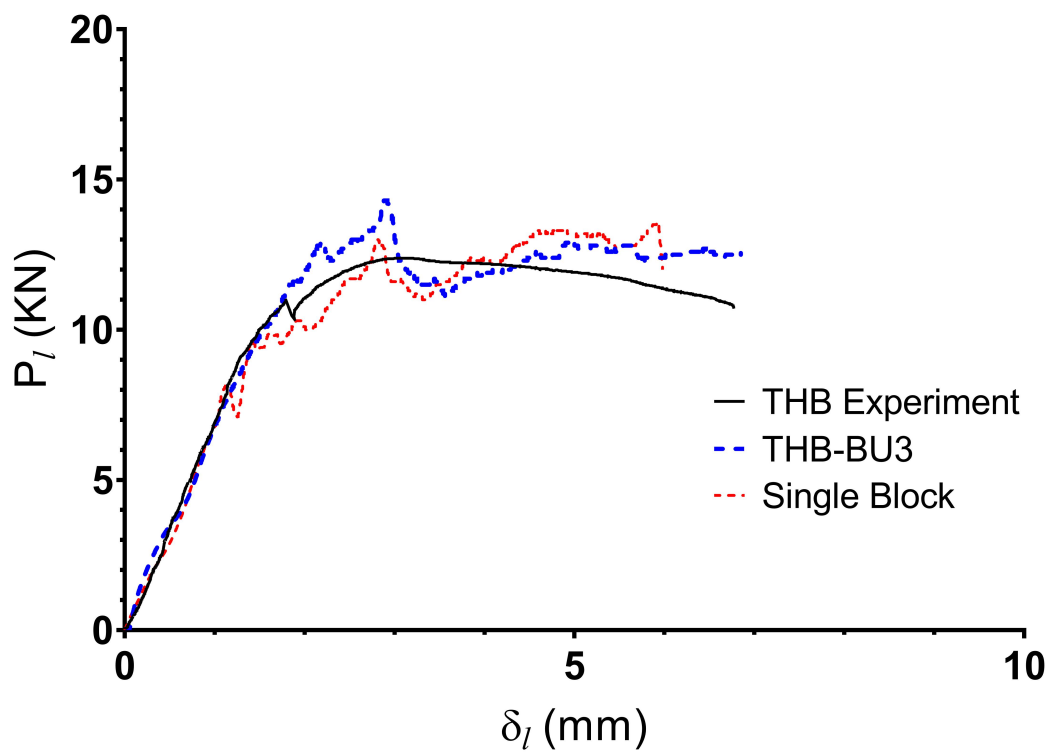
Figure 4.17: Graphs showing the comparison between THB experiment and simulation versus single block simulation

Overall, the tests response was generally in-line with expectations and the characteristic load-displacement response, as measured by $\delta_l - P_l$ curves, was informative. Based on high speed video images, the failure mode varied somewhat between specimens, but generally consisted of the formation of initial tensile fractures in the crushing zones (inter-block and near the upper and lower axial platens). These initial fractures typically occurred at 1/3 or 1/2 of the block thicknesses. Progression of failure was driven by tensile fracturing and influenced, to some extent, by the distribution of natural flaws (micro-defects) within the rock structure. Final rupture failure was violent involving complete fracture of one or both blocks. The $\delta_l - P_l$ curves showed a linear stage, followed by three key load thresholds: yield, peak and rupture. These thresholds could also be identified by AE data indicated by increasing emissions (fracture formation) corresponding to each threshold.

The tests were analyzed as two groupings of σ_a (10 and 15 MPa) for trends and clear relations were shown between T/L ratio with both P_{lp} and δ_{la}/L (at rupture). The tests also show that there is a relation between both T/L and σ_a with brittle-ductile post-peak response based on $\delta_l - P_l$ curves for the thicker specimens under $\sigma_a = 15$ MPa, with both T44S15 and T50S15 showing an increase in load capacity from yield to peak followed by brittle failure/rupture. The results showed lateral displacement of the buckling apex at peak consistently to be approximately δ_{la}/L of 0.16 to 0.2 across the full range of T/L tested, but with somewhat higher values at rupture (0.26 to 0.29). This compares with a value based on theoretical analysis suggested by Diederichs and Kaiser (1999) that buckling failure would typically occur

at $\delta_{la}/L = 0.1$. It is difficult to say if this theoretical value should be compared to either the yield, peak or rupture point.

An analytical approach was carried out using a similar work conducted on masonry structures. The main difference between this method and the THB configuration is the boundary condition assumptions. The initial results regarding the resistance factor, $\Phi_m = 1$, showed a large gap between the analytical and experimental P_{lp} values. This data shows the importance of the resistance factor in calculating the P_{lp}. Therefore, the Φ_m was back-calculated using the experimental P_{lp} to gain insight regarding the variability and sensitivity of Φ_m. The results demonstrated that the Φ_m amount was changed with different axial confinements and thicknesses. It could be concluded that Φ_m is not only dependent on the material, but also it was dependent on the boundary condition and geometry of the specimen. The results suggested that σ_{ci} may be a better predictor of THB behaviour using this analysis method and associated assumptions.

A GBM, micro-mechanical, discontinuum model using the *UDEC* Voronoi block modelling method was used to simulate test T33S10 to provide insight into the experimental results and the failure progression. Analyses were conducted based on material parameters obtained from calibration to the average UCS test properties. Although this test showed a reasonable match to general test trends, the response was stiffer in the linear range and showed substantially more tensile fracturing in the lateral platen area that was observed in the actual tests. Therefore, the model parameters were revised (recalibrated) with reduced stiffness and increased tensile

strength and was able to produce a good match, although the tensile strength used as a micro-mechanical parameter may be considered unrealistically high. The *UDEC-GBM* method and associated calibration techniques for micro-mechanical properties an evolving research topic and currently, no clear guidelines exist. Although tensile failure behaviour in the model needs some improvement, the results of the simulation showed a reasonable match to observed behaviour and provided valuable insight into the failure progression during THB. The model suggests that improvements to the lateral platen configuration, perhaps doubling the platen contacts, may be warranted for future experimental testing. In addition, the model could be calibrated directly to the THB test itself.

Publication Notes

Acknowledgements

Funding Sources

Compliance with Ethical Standards

The authors declare that they have no known conflict of interest with respect to the study presented in this article.

Chapter 5

Conclusion

This research aimed to study the THB failure mechanism in a controlled condition and at a laboratory scale to give an insight regarding the fundamentals of buckling failure mechanisms. This goal was achieved by through the study's 4 steps. The first step was to collect all buckling failure occurrences reported in the field, statistical analysis of these cases relative to parameters such as buckling orientation, in situ stresses distribution at the buckling location, and rock type. A comprehensive study of existence buckling failure stability analysis and buckling failure modes following by introduction of a classification for the possible modes of near-surface buckling failure were presented in this step. In the second step, a new THB experiment methodology and test apparatus were developed to simulated the THB on a laboratory scale. Then, in the third step, several THB tests were carried out using the new THB experiment methodology and apparatus on Wallace sandstone which provided insight regarding the important factors in THB failure. Lastly, in the fourth step, numerical modelling was carried out to simulate the new THB experiment using the commercial code *UDEC* to provide an insight regarding the THB process, fracture and stress distribution of the experiment, and the possibility of modelling the complex modes of buckling failure.

5.1 Review of All Ground Surface Buckling Cases and Failure Mechanisms

This step's goal was to well-understand the occurrence of buckling failure in the field, such as the dominant modes, rock types, and in situ stresses conditions, by studying the buckling failures reported in the field. A database (Ghasemi and Corkum, 2020a) was collected for all past buckling incidents reported in North America with the information regarding geological condition, buckling dimensions and directions, in situ stresses, bedrocks, and buckling locations types if the data were available.

The buckling incidents were compared with the s_H value by geographically mapping all cases and comparing them with the buckling locations' in situ stress regime. Moreover, a good correlation was observed by comparing the orientation of buckling and s_H (α_b and β_b respectively) in the field. It was revealed that the majority of the buckling failure reported in North America were located in quarries and open fields, and dominant rock types that host the buckling failures were limestone and undifferentiated carbonates. It was noted that in only 15% of total buckling cases have reported the buckling dimensions. However, these data gave us a sampling regarding the range dimension for field buckling, which could be utilized in future risk assessment.

In addition, a review of existing buckling stability analysis accompanied by possible buckling mechanisms in quarries and open fields was presented in this study. The classification of the failure mode is an essential step to choose a proper stability analysis, and based on the buckling mode classification presented in this study, it

could be possible to classify the buckling, despite the complexity of buckling failure. Also, this study presented a buckling mode classification for near-surface buckling based on the common documented cases.

5.2   A New THB Experimental Method

This step aimed to provide a method to gain a better understanding of a simplified buckling failure under the controlled laboratory condition. Although the buckling failure in the field is complex, it is essential to well-understand a simplified mode of buckling that is THB due to the lack of knowledge about the nature of this failure mechanism. Therefore, an innovative THB experimental methodology associated with the buckling apparatus's invention was developed to reproduce a simple THB failure at the laboratory scale under well-controlled condition.

Using this new THB experiment, two identical rock blocks were attached together vertically and aligned with the test frame. The load frame was used to apply the axial load (P_a) on the specimen to provide axial confinement. This axial load is representing the horizontal in situ stresses in the field. Two lateral loading bars were utilized to apply a lateral load (P_l) on the specimen in a controlled way to initiate the buckling failure process to reproduce a 'trigger' mechanism. The axial and lateral load and displacement were recorded using the typical monitoring devices, i.e. LVDTs, load cells, and LPs. The experiments were monitored using a high-speed video camera.

In order to improve the test apparatus and methodology, several preliminary tests

were carried out. These preliminary tests resulted in some modification and development in the test apparatus and methodology to properly reproduce the THB considering the proper boundary conditions, loading rate and sequence. This test apparatus was designed to be completely adjustable and allows for THB tests with different specimen geometry or different axial confinement. The primary result of this new experimental methodology showed that it could simulate the THB failure under a controlled and well-designed monitoring system under the wide range of configuration.

In general THB failure mechanism was observed to progress in the experimental test in a manner similar to anticipated with the crushing zones' location observed at the hinge locations, and the buckling failure completed when the specimen was broken and separated at the crushing zone. A numerical model using a simple elastic distinct element method was developed to simulate the THB test using the *3DEC* code. This simplified, preliminary modelling exercise showed that the axial stress in the crushing zone is greater than the specimen's σ_c when the buckling occurred.

5.3 An experimental study and modelling simulation of three hinge buckling

Using the newly introduced THB experiment, several THB tests were carried out on Wallace sandstone in a various range of thickness (T) and two different axial confinement (i.e. $\sigma_a = 10$ and 15 MPa) following with advanced numerical simulation to complete the goals of step three and four. In these tests, novel monitoring methods, i.e. an AE system and high-speed video recording to use in the DIC method, were

utilized accompanied by the conventional devices to capture the load and displacement.

The test result showed a good agreement with our expectation, and load-displacement behaviour ($\delta_l - P_l$) of tests provides useful information that increased our insight regarding THB failure. Images obtained from the high-speed video camera show that the formation of initial tensile fractures occurred in the crushing zones, usually at 1/3 to 1/2 of the block thicknesses. It was observed that the rupture failure for all tests was violent, and fracture progression was observed in both or one of the blocks. Conducting these THB tests revealed that THB failure's completion is consists of a few stages, i.e. linear, yield, peak, and rupture stage, which also identified with AE data. The THB tests were conducted on two sets of confining stresses ($\sigma_a = 10$ and 15 MPa), and in both groups, a clear relationship between the T/L ratio and P_{lp} and δ_{la}/L were observed. Also, a brittle-ductile post-peak behaviour in relation to T/L and σ_a was observed based on the $\delta_l - P_l$ curves. The buckling apex lateral load-displacement results revealed that the peak occurred at δ_{la}/L of 0.16 to 0.2, and this amount was increased at rupture in the range between (0.26 to 0.29).

A numerical simulation of test T33S10 using *UDEC* Voronoi block modelling method with a GBM, micro-mechanical, discontinuum model was carried out to provide insight into the THB results. The material properties of the models were calibrated with the average UCS test properties. The test simulation generally was in good agreement with the test's general trends; however, the model shows a stiffer

behaviour in a linear range and more tensile fracturing around the lateral platen location. This behaviour resulted in some modifications to the model parameters by reducing the stiffness and increase in tensile strength. This revised version of the model has produced a good match with the actual test. It should be noted that although the tensile strength of the micro-mechanical parameter of the model may be high, the *UDEC*-GBM method is an evolving research area, and no clear guideline exists. Overall, the simulation results showed an acceptable match with THB experiment behaviour and provided a useful understanding of THB failure.

5.4 Recommendations for Future Work

The following steps are recommended for future work:

- In case of future buckling events, it is recommended to carefully document these events and adding them to the online database (Ghasemi and Corkum, 2020a) which is accessible to researchers and engineers with more details compared to the current documented cases presented in this study such as mode of failure, dimensions details, and rock type. This database would be a crucial step in a good understating of buckling instability in the near-surface environment.

- The trigger mechanism of the current test utilizes two lateral bars to initiate buckling. In order to gain better insight regarding the effect of the uniform load as a trigger, using an air bladder (distributed load) is recommended for future tests to apply the trigger pressure. This modification would reasonably simulate the loading of the buckling stratum by water pressure – an expected

failure trigger in some cases.

- The experimental results revealed valuable parametric data regarding the THB mechanism. However more experiments with different T/L ratio, or axial confinement ranges is required to complete our understanding about THB failure.

- In order to fully understand the crack and fracture progression during the THB tests, the complete AE analysis is recommended to map the location of each event in entire specimens. This analysis requires more sensors attached to the specimen during the test. The AE system could also provide valuable data regarding the effect of the boundary condition and trigger mechanism during the experiment.

- The numerical model suggests that the lateral platen may be improved by some modifications. This modification might include doubling the platens' contacts (i.e., 4 bars instead of 2).

- Numerical simulation showed that the complex models using the *UDEC* software can reproduce THB failure, but it requires more research about the effect of micro-mechanical parameters, especially tensile strength, on simulating the THB. Perhaps it would be beneficial to calibrate the model with a larger range of laboratory testing, such as UCS, triaxial test and tensile strength tests. In addition the THB experiment itself can be a useful direct calibration test.

- This novel THB experiment could modified and used for future studies on high-stress brittle failure (i.e., spalling) in rock.

Bibliography

J. Adams. Stress-relief buckles in the McFarland quarry, Ottawa. *Canadian Journal of Earth Sciences*, 19(10):1883–1887, 1982.

J. Adams and J. Bell. Crustal stresses in Canada. In *Neotectonics of North America*, pages 367–386. Geological Society of America, U.S.A, 1991.

B. Amadei, H. Swolfs, and W. Savage. Gravity-induced stresses in stratified rock masses. *Rock Mechanics and Rock Engineering*, 21(1):1–20, 1988.

B. Arjang. Database on Canadian in situ ground stresses. Technical report, CANMET Mining and Mineral Sciences Laboratories report, 2001.

D. Armstrong. Paleozoic geology of the northern lake Simcoe area, south-central Ontario. Technical report, Ontario Geological Survey, 2000.

D. Armstrong and J. Dodge. Paleozoic Geology of Southern Ontario - Project Summary and Technical Document. *Ontario Geological Survey*, Miscellane:30, 2007.

ASTM C1609/C1609M-12. Standard Test Method for Flexural Performance of Fiber-Reinforced Concrete (Using Beam With Third-Point Loading) BT - Standard Test Method for Flexural Performance of Fiber-Reinforced Concrete (Using Beam With Third-Point Loading). Technical Report C 1609/C 1609M-05, 12.

ASTM D4543. Standard Practices for Preparing Rock Core as Cylindrical Test Specimens and verifying Conformance to Dimensional and Shape Tolerances. *Astm*, (D4543-08):1–9, 2008.

Z. T. Bieniawski and I. Hawkes. Suggested Methods for Determining Tensile Strength of Rock Materials - 1. Suggested Method for Determining Direct Tensile Strength. *International Journal of Rock Mechanics and Mining Sciences*, 15(3):99–103, 1978. ISSN 13651609.

J. Blaber, B. Adair, and A. Antoniou. Ncorr: Open-Source 2D Digital Image Correlation Matlab Software. *Experimental Mechanics*, 55(6):1105–1122, jul 2015. ISSN 0014-4851.

C. W. Boon. Study of reinforcement support mechanisms for wide-span horse-shoe-shaped openings in horizontally layered jointed rock using the distinct element method. *Rock Mechanics and Rock Engineering*, 52(4):1179–1191, 2019.

C. Brawner. *Engineer– Around the World in Fifty Years*. BiTech Publishers, Richmond, BC, 2003.

D. Carson. Paleozoic geology of the Belleville-wellington area, southern Ontario. Technical report, Ontario Geological Survey, 1981.

D. Cavers. Simple methods to analyze buckling of rock slopes. *Rock Mechanics*, 14 (2):87–104, 1981.

J. A. Corbin. Stress Distribution in Laminar Rock during Sliding Failure. *International Journal of Rock Mechanics and Mining Sciences*, 15/3(6):113–119, 1978.

A. Corkum, B. Damjanac, and T. Lam. Variation of horizontal in situ stress with depth for long-term performance evaluation of the Deep Geological Repository project access shaft. *International Journal of Rock Mechanics and Mining Sciences*, 107(March 2017):75–85, 2018a.

A. G. Corkum, Y. Asiri, H. El Naggar, and D. Kinakin. The leeb hardness test for rock: An updated methodology and ucs correlation. *Rock Mechanics and Rock Engineering*, 51(3):665–675, 2018b.

F. Crossley. Wood's Sand and Gravel Quarry - Dewatering Effects, 1991.

P. Cundall. A Computer Model for Simulating Progressive Large Scale Movements in Blocky Rock Systems. volume 1, 1971.

B. Damjanac and I. C. Group. Supporting Technical Report Phase I Long-Term Cavern Stability. 2008.

G. Davis. Partitioned tectonic shortening, with emphasis on outcrop-scale folding and flattening, Pindos fold-and-thrust belt, Peloponnese, Greece. *Canadian Journal of Earth Sciences*, 56(11):1181–1201, jan 2019.

J. L. Dawe and C. K. Seah. Out-of-plane resistance of concrete masonry infilled panels. 1989.

G. Dickie. *Building Stone in Nova Scotia*. Department of Natural Resources, Mines and Energy Branches, Halifax, 3 edition, 1993.

M. S. Diederichs. The 2003 Canadian Geotechnical Colloquium: Mechanistic interpretation and practical application of damage and spalling prediction criteria for deep tunnelling. *Canadian Geotechnical Journal*, 44(9):1082–1116, 2007.

M. S. Diederichs and P. K. Kaiser. Stability of large excavations in laminated hard rock masses: The voussoir analogue revisited. *International Journal of Rock Mechanics and Mining Sciences*, 36(1):97–117, 1999.

R. G. Drysdale and A. A. Hamid. *Masonry Structures: behaviour and design*. Canada Masonry Design Centre, canadian e edition, 2005.

E. Esterhuizen, C. Mark, and M. Murphy. Numerical model calibration for simulating coal pillars, gob and overburden response. *Proceedings - 29th International Conference on Ground Control in Mining, ICGCM*, pages 46–57, 2010.

R. Everitt. Pop-ups and related damage in granite at the Medika Pluton in southeastern Manitoba. *Canadian Geotechnical Journal*, 46(8):1001–1008, 2009.

S. Fabbi and L. Smeraglia. Pop-up structure in massive carbonate-hosted fold-and-thrust belt: Insight from field mapping and 2D kinematic model in the central Apennines. *Journal of Structural Geology*, 126(February):258–271, 2019.

F. Gao, D. Stead, and D. Elmo. Numerical simulation of microstructure of brittle rock using a grain-breakable distinct element grain-based model. *Computers and Geotechnics*, 78(September):203–217, 2016.

T. V. Garza-Cruz, M. Pierce, and P. Kaiser. Use of 3DEC to study spalling and deformation associated with tunnelling at depth. In *Proceedings of the Seventh International Conference on Deep and High Stress Mining*, pages 421–434. Australian Centre for Geomechanics, 2014.

M. Ghasemi and A. Corkum. Ground surface rock buckling cases: Published Dataset, 2020a. Mendeley Data, v3http://dx.doi.org/10.17632/yh6cfhpjd7.3.

M. Ghasemi and A. Corkum. A three hinge buckling laboratory test. *Rock Mech Rock Eng*, 2020b.

M. Ghasemi and A. G. Corkum. Development of a Laboratory Testing Apparatus for Three-Hinge Buckling. In *ARMA18 - 52nd US Rock Mechanics / Geomechanics Symposium*, number 18–040, Seattle, 2018.

M. Ghasemi, A. Corkum, and G. Gorrell. Ground surface rock buckling: a review of collected cases and failure mechanisms. *Rock Mechanics and Rock Engineering*, submitted 2020.

G. P. Giani. *Rock Slope Stability Analysis*. A.A. Balkema, Netherland, 1992.

R. E. Goodman. *Methods of geological engineering in discontinuous rocks*. West Publishing Company, New York, 1976.

G. Gorrell. Investigation and Documentation of the Neotechtonic Record of Prince Edward County, Ontario. Technical report, GSC Open File Report 2062, 1988.

G. Gorrell. Supplementary Information from 2002 to 2009 Field Investigations, Proposed Braeside Quarry Expansion, Part Lots 16 & 17, Concession A, Township of McNab/Braeside, Renfrew County. Technical report, 2012.

G. Gorrell and T. Fletcher. Mineral Aggregate Resources Inventory of the County of Hastings; Southern Ontario. Technical report, Ontario Geological Survey, 1987.

GRI. Aggregate Assessment of Ottawa Carleton. Technical report, Ministry of Natural Resources., 1993. Gorrell Resource Investigations.

GRI. Preliminary evaluation of Hallville Quarry, Ontario. Technical report, 2017. Gorrell Resource Investigations.

A. Guerin, M. Jaboyedoff, B. Collins, M. Derron, G. Stock, B. Matasci, M. Boesiger, C. Lefeuvre, and Y. Podladchikov. Detection of rock bridges by infrared thermal imaging and modeling. *Scientific Reports*, 9(1):1–20, 2019.

J. Handin and L. Pattison. Experimental folding of rocks under confining pressure: Part II. Buckling of multilayered rock beams. *Bulletin of the Geological Society of America*, 87(7):1035–1048, 1976.

O. Heidbach, M. Rajabi, X. Cui, K. Fuchs, B. Müller, J. Reinecker, K. Reiter, M. Tingay, F. Wenzel, F. Xie, M. Ziegler, M. Zoback, and M. Zoback. The World Stress Map database release 2016: Crustal stress pattern across scales. *Tectonophysics*, 744:484–498, oct 2018.

R. Hobbs. Axisymmetric upheaval buckling of a heavy sheet. *Journal of Applied Mechanics*, 57(2)(June 1990):472–474., 1990.

R. E. Hobbs. Two-dimensional upheaval buckling of a heavy sheet. *Thin-Walled Structures*, 8(3):235–252, jan 1989.

E. Hoek and C. Martin. Fracture initiation and propagation in intact rock – A review. *Journal of Rock Mechanics and Geotechnical Engineering*, 6(4):287–300, aug 2014.

G. Holzhausen and A. Johnson. The concept of residual stress in rock. *Tectonophysics*, 58(3-4):237–267, 1979. Publisher: Elsevier.

S. Hsu, S. Chiang, and J. Lai. Failure mechanisms of tunnels in weak rock with interbedded structures. *International Journal of Rock Mechanics and Mining Sciences*, 41(SUPPL. 1):1–6, 2004.

X. Hu and D. Cruden. Buckling deformation in the Highwood Pass, Alberta, Canada. *Canadian Geotechnical Journal*, 30:276–286, 1993.

ISRM. Suggested Methods for Determining Compressive Strength and Deformability Suggested Methods for Determining the Uniaxial Compressive Strength and Deformability of Rock. *International Society for Rock Mechanics*, (December):0–3, 1977.

ISRM. *The ISRM suggested methods for rock characterization, testing and monitoring: 1974-2006.* Suggested Methods Prepared by the Commission on Testing Methods, International Society for Rock Mechanics (ISRM Blue Book). Springer, 2007.

Itasca. *UDEC — Universal Distinct Element Code. Version 6.* Itasca Consulting Group Inc., Minneapolis, Minnesota, 2014.

Itasca. *3DEC — Three-Dimensional Distinct Element Code. Version 5.2.* Itasca Consulting Group Inc., Minneapolis, Minnesota, 2016.

Itasca. *PFC — Particle Flow Code, Ver. 6.0.* Itasca Consulting Group Inc., Minneapolis, Minnesota, 2018.

P. Kaiser and S. Maloney. Review of Ground Stress Database for the Canadian Shield. Technical Report to Ontario Power Generation, Nuclear Waste Management Division 06819-REP-01300-10107-R00, MIRARCO Mining Innovation, 2005.

A. Karami and D. Stead. Asperity degradation and damage in the direct shear test: A hybrid FEM/DEM approach. *Rock Mechanics and Rock Engineering*, 41(2): 229–266, 2008.

E. Karampinos, J. Hadjigeorgiou, J. Hazzard, and P. Turcotte. Discrete element modelling of the buckling phenomenon in deep hard rock mines. *International Journal of Rock Mechanics and Mining Sciences*, 80:346–356, 2015.

P. F. Karrow. Bedrock stress release features on Manitoulin Island, Ontario. 47: 389–393, 1993.

V. Kazakidis. Confinement effects and energy balance analyses for buckling failure under eccentric loading conditions. *Rock Mechanics and Rock Engineering*, 35(2): 115–126, 2002.

F. H. Kulhawy. Stress deformation properties of rock and rock discontinuities. *Engineering Geology*, 9(4):327–350, 1975.

T. Lam, D. Martin, and D. McCreath. Characterising the geomechanics properties of the sedimentary rocks for the DGR excavations. In *Canadian Geotechnical Conference OttawaGeo2007*, pages 636–44, Ottawa, 2007.

A. LeRiche, K. Kalenchuk, and M. Diederichs. Estimation of in situ stress from borehole breakout for improved understanding of excavation overbreak in brittle-anisotropic rock, 2017.

B. Q. Li and H. H. Einstein. Comparison of Visual and Acoustic Emission Observations in a Four Point Bending Experiment on Barre Granite. *Rock Mechanics and Rock Engineering*, 50(9):2277–2296, 2017.

B. Liberty. Paleozoic geology of the Lake Simcoe area, Ontario. Technical Report Memoir 355, Department of Energy, Mines and Resources Canada Department of Energy, Mines and Resources Canada Department of Energy, Mines and Resources Canada, 1969.

B. Liberty. Paleozoic geology of Wolfe Island, Bath, Sydenham and Gananoque map areas, Ontario. Technical report, 1971.

Y. Lin, Y. Hong, S. Zheng, and Y. Zhang. Failure modes of openings in a steeply bedded rock mass. *Rock Mechanics and Rock Engineering*, 17:113–119, 1984.

K. Y. Lo. Regional distribution of in situ horizontal stresses in rocks of Southern Ontario. 15:371–381, 1978.

O. Mahabadi, A. Lisjak, L. He, B. Tatone, P. Kaifosh, and G. Grasselli. Development of a new fully-parallel finite-discrete element code: Irazu. volume 4, pages 2695–2703, 2016.

C. Martin and R. Christiansson. Estimating the potential for spalling around a deep nuclear waste repository in crystalline rock. *International Journal of Rock Mechanics and Mining Sciences*, 46(2):219–228, 2009.

C. D. Martin, R. S. Read, and J. B. Martino. Observations of brittle failure around a circular test tunnel. *International Journal of Rock Mechanics and Mining Sciences*, 34(7):1065–1073, oct 1997.

J. M. Mayer and D. Stead. Exploration into the causes of uncertainty in UDEC Grain Boundary Models. *Computers and Geotechnics*, 82:110–123, 2017.

E. L. McDowell, K. E. McKee, and E. Sevin. *Arching action theory of masonry walls*, volume 82. 1956.

C. Mitchell, S. Adhya, S. Bergström, M. Joy, and J. Delano. Discovery of the Ordovician Millbrig K-bentonite Bed in the Trenton Group of New York State: implications for regional correlation and sequence stratigraphy in eastern North America. *Palaeogeography, Palaeoclimatology, Palaeoecology*, 210(2):331–346, 2004.

NRC-NS. Wallace Quarries-Test Data. Technical report, National Research Council, Halifax, Nova Scotia, 1967.

A. Nusayr and P. R. Paslay. Buckling of an Infinite Sheet With a One- sided Constraint. (22):3–4, 1972.

M. Perras and M. Diederichs. Predicting excavation damage zone depths in brittle rocks. *Journal of Rock Mechanics and Geotechnical Engineering*, 8(1):60–74, 2016.

D. Potyondy and P. Cundall. A bonded-particle model for rock. *International Journal of Rock Mechanics and Mining Sciences*, 41(8 SPEC.ISS.):1329–1364, 2004.

J. Roorda. Buckles, bulges and blow-ups. *Applied solid mechanics*, 2:347–380., 1988.

J. Roorda. The mechanics of a pop-up: a stress relief phenomenon. *Canadian Geotechnical Journal*, 39(1):368–373, 1995.

J. Roorda, J. C. Thompson, and O. L. White. The analysis and prediction of lateral instability in highly stressed, near-surface rock strata. *Canadian Geotechnical Journal*, 19(4):451–462, 1982.

A. Rutty and A. Cruden. Geographie physique et Quaternaire. 47:379–388, 1993.

V. Saull and D. Williams. Evidence for Recent Deformation in the Montreal Area. *Canadian Journal of Earth Sciences*, (1973), 1974.

W. Savage. The development of residual stress in cooling rock bodies. *Geophysical Research Letters*, 5(8):633–636, 1978.

B. Singh and R. Goel. *Tunnelling in Weak Rocks*. Elsevier, Amsterdam, 2006.

A. Sofianos. Analysis and design of an underground hard rock voussoir beam roof. *International Journal of Rock Mechanics and Mining Sciences & Geomechanics Abstracts*, 33(2):153–166, 1996.

A. Starfield and P. Cundall. Towards a methodology for rock mechanics modelling. 25(3):99–106, 1988.

D. Stead, E. Eberhardt, and J. S. Coggan. Developments in the characterization of complex rock slope deformation and failure using numerical modelling techniques. *Engineering Geology*, 83(1):217–235, 2006.

R. Sterling. The Ultimate Load Behavior of Laterally Constrained Rock Beams, 1980.

R. Thomas, J. Wallach, R. McMillan, J. Bowlby, S. Frape, D. Keyes, and A. Mohajer. Recent Deformation in the Bottom Sediments of Western and Southeastern Lake Ontario and its Association with Major Structures and Seismicity. *Géographie physique et Quaternaire*, 47(3):325–335, nov 1993.

P. Tommasi, L. Verrucci, P. Campedel, L. Veronese, E. Pettinelli, and R. Ribacchi. Buckling of high natural slopes: The case of Lavini di Marco (Trento-Italy). *Engineering Geology*, 109(1-2):93–108, oct 2009.

C. Twidale and J. Bourne. On the origin of A-tents (pop-ups), sheet structures, and associated forms. *Progress in Physical Geography*, 33(2):147–162, 2009.

A. Vakili, M. Sandy, and J. Alercht. Interpretation of non-linear numerical models in geomechanics-a case study in the application of numerical modelling for raise bored shaft design in a highly stressed and foliated rock mass. In *The 6th International Conference and Exhibition on Mass Mining*, Sudbury, 2012.

J. Wallach and J. Chagnon. The occurrence of pop-ups in the Quebec City area. *Canadian Journal of Earth Sciences*, 27(5):698–701, 1990.

J. Wallach, K. Benn, and R. Rimando. Recent, tectonically induced, surficial stress-relief structures in the Ottawa Hull area, Canada -. 333:325–333, 1994.

J. L. Wallach, A. A. Mohajer, and G. H. McFall. Pop-ups as geological indicators of earthquake-prone areas in intraplate eastern North America. *Quaternary Proceedings*, (January 1993), 1993.

C. Y. Wang. On symmetric buckling of a finite flat-lying heavy sheet. *Journal of applied mechanics*, pages 8–12, 1984.

O. White, P. Karrow, and J. Macdonald. Residual stress relief phenomena in southern Ontario. In *9th Canadian Rock Mechanics Symposium*, pages 323–348, 1973.

O. L. White and D. J. Russell. High Horizontal Stresses in Southern Ontario - Their Orientation and Their Origin. In *IV Congress International Association of Engineering Geology*, volume v, 1982.

D. A. Williams and P. G. Telford. Paleozoic geology of the Ottawa area - Field Trip 8: Guidebook, 1986.

D. A. Williams, R. R. Wolf, and A. M. Rae. Paleozoic Geology of the Arnprior - Quyon Area, Southern Ontario, 1984.

H. Williams, D. Corkery, and E. Lorek. A study of joints and stress-release buckles in Palaeozoic rocks of the Niagara Peninsula, southern Ontario. *Canadian Journal of Earth Sciences*, 22(2):296–300, feb 1985.

A. Wilson. Geology of the Ottawa - St. Lawrence Lowland, Ontario and Quebec. Technical report, 1964.

S. Yong and S. Maloney. *An Update to the Canadian Shield Stress Database*. Number September. 2015.

M. Zoback, M. Zoback, J. Adams, M. Assumpção, S. Bell, E. Bergman, P. Blümling, N. Brereton, D. Denham, J. Ding, K. Fuchs, N. Gay, S. Gregersen, H. Gupta, A. Gvishiani, K. Jacob, R. Klein, P. Knoll, M. Magee, J. Mercier, B. Müller, C. Paquin, K. Rajendran, O. Stephansson, G. Suarez, M. Suter, A. Udias, Z. Xu, and M. Zhizhin. Global patterns of tectonic stress. *Nature*, 341(6240):291–298, 1989.

Appendices

Appendix A

Development of a Laboratory Testing Apparatus for Three-Hinge Buckling

M. Ghasemi, A.G. Corkum,

A.1   Abstract

The main objective of this research is to investigate the buckling failure mechanism in sedimentary laminated rocks. Near-surface buckling failure typically occurs in horizontally bedded sedimentary rocks in the presence of high horizontal in-situ stresses. This failure is commonly accompanied by a sudden energy release like rock bursting. Despite previous research, there remains many limitations to develop a standard design methodology for buckling failure. A new laboratory experimental testing procedure was developed to study the three-hinge buckling failure (THB) mechanism of rocks, including the design and fabrication of a new apparatus suited to reproduce the buckling failure at laboratory scale. THB tests were conducted to calibrate and troubleshoot the apparatus, and several modifications were implemented. Moreover,

a numerical model based on the two-dimensional discrete element method (DEM) was developed to provide insight into the internal mechanisms of failure of the laboratory experimental testing using the *UDEC* Voronoi tessellation technique. Preliminary modelling shows promise in capturing this complex brittle rock failure mechanism. Overall, this study helps us to reproduce the THB failure at laboratory scale and provides the opportunity of observing the buckling failure and obtaining invaluable information about its process.

A.2 Introduction

Buckling failure (pop up) is one of the main challenges in high-stressed horizontally bedded rocks. Near-surface buckling failure typically occurs in horizontally bedded sedimentary rocks with the presence of high horizontal in situ stresses. This failure is commonly accompanied by a sudden energy release like rock bursting. Adams (1982); Roorda et al. (1982); Wallach et al. (1993) reported the incident of buckling failure in Ontario, Quebec, and New York. In quarries, sometimes horizontal layers or rock mass with horizontal joints heave due to removing the overburden (Adams, 1982). Buckling failure may occur in the thin rock layers under high horizontal in situ stresses. Also, it can be followed by violent brittle failure (Singh and Goel, 2006).

Buckling failure may be divided into the two main modes:

- Flexural buckling (Euler method)

- Three hinge buckling (THB)

In recent years, several investigations of buckling failure in near-surface bedded

rocks, and slopes were carried out by various authors such as Cavers (1981); Roorda et al. (1982); Roorda (1995); White and Russell (1982); Corbin (1978); Goodman (1976).

One potential cause of buckling failure is the occurrence of THB in the horizontal slabs. In the natural or excavation induced instabilities, this type of buckling can occur in near-surface rock strata. In areas with high in-situ stresses, quarrying causes redistribution of stresses and increases horizontal stress; As a result, there is a severe upheaval of a quarry floor. For example, in 1969 in Missouri, a 1.2 m thick bed of proper Salem limestone buckled and upheaved almost 0.6 m and extending for a length of 90 m length. In Figure A.1, a detailed cross-section of a multi-layered "pop up" which occurred in a dolomitic limestone quarry is shown (Roorda, 1995).
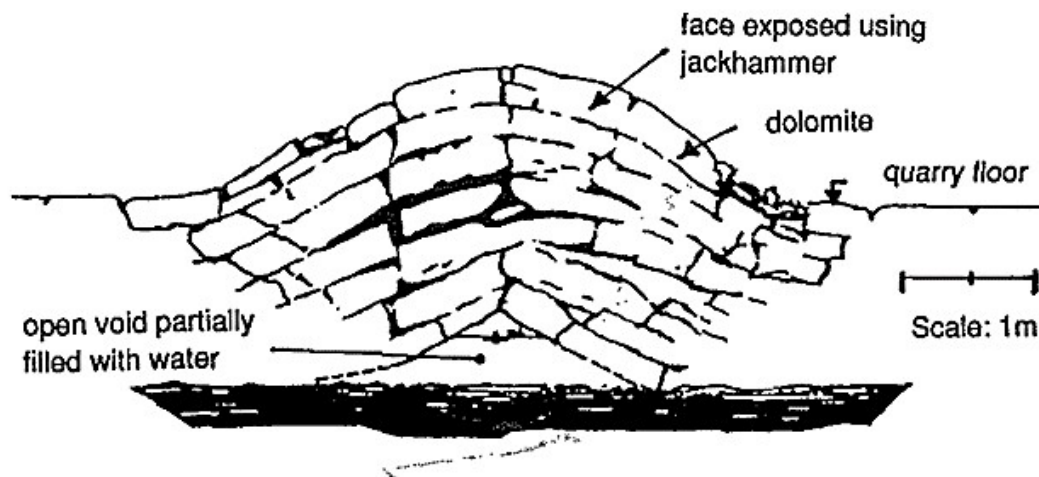

Figure A.1: Section through a multilayered pop up in a quarry floor (Roorda, 1995).

Frequently, most of the near- surface rock strata contain many vertical joints. When horizontal in-situ compressive stresses exist, joints are tightly closed, and this

stratum is like a continuous unjointed plate as visible in Figure A.1.

Roorda (1995) used the axis-symmetrical behavior of an infinite elastic plate lying on a horizontal substrate that uniformly compared in all directions to investigate the fundamental features of buckling mechanics. Based on this analysis, a minimum initial in-plane compressive stress exists in each buckling process. Moreover, a small trigger disturbance is always required for the plane and heavy plates. Diederichs and Kaiser (1999) worked on the Voussoir beam theory, specifically beam snap-through failure, which is common in large spans hard rocks. They proposed a design chart based on linear limitation for jointed rock beams, including the summarized relationship between span, thickness, and modulus.

Handin and Pattison (1976) studied the experimental folding of rock under confining pressure, including the buckling of multilayered rock beams. They highlighted some principal factors affecting buckling failure of multilayered rocks, such as the mechanical effect of layers, factors controlling fold shape, superposition of stresses. For instance, they found that the critical buckling stress is higher for thin-beam folds in single layers of limestone or sandstone than one with a three-layered specimen with the same thickness.

Previous studies (Karampinos et al., 2015; Mayer and Stead, 2017) demonstrated that the distinct element programs such as *UDEC* and *3DEC* have better performance in modeling buckling failure observed in the field. Discontinuum numerical modeling provides the ability to consider the role of fractures in the rock mass. Also, a buckling failure can be developed including rotation, fracture opening or detachment of rock

block. Although there are some uncertainties using GBM, using a realistic simulation helps to validate the rock behavior. Also, the analytical and physical models are complementary of a numerical model, which is necessary for a comprehensive study. Therefore, the experimental test implemented for simple THB was simulated using *UDEC* software.

Although a common test to evaluate the flexural properties of the materials is four-point bending test (ASTM C1609/C1609M-12, 12), to the best of authors' knowledge, no experimental test to study the THB with the required confinements (e.g. the axial load) is available in the literature. Buckling failure causes many economic and environmental problems. For instance, in limestone quarries and open pit mines, if "rock buffer" which prevents hydraulic connectivity is not thick enough, it may begin flooding; thus, impact on nearby wells, and cause damage in quarries due to buckling failure. Currently, evaluation of the rock buffer thickness is based on the past records.

Despite that fact that some research has been done, many challenges still stand to design a procedure for THB stability analysis. The most important one is the lack of a specific, accurate and cost-effective method to investigate this mechanism; therefore, presenting a quantitative way to understand the possible 'trigger' mechanisms (e.g. water pressure, unloading from quarry mining) that drives buckling failure is necessary.

A.3   Experimental Design Setup

A new experimental design setup was established in order to simulate a simple THB configuration in the laboratory. This new experimental method allows us to observe this type of failure at laboratory scale and give us a better understanding of its mechanism. The objective was to develop a test apparatus that could apply an axial load (analogous to the horizontal stress in situ) at the rock blocks while inducing a THB buckling 'trigger'. To begin, two blocks with total length (L) to the thickness (T) ratio of (X) was considered (Figure A.2) for a simple THB analysis. These blocks are placed above each other. Although THB usually occurs on horizontally bedded rocks in quarries, we placed blocks above each other because of the simplicity and practicality of the test with our existing load frame. A constant vertical load is applied on these blocks. This vertical load simulates the horizontal stress of the field. Then a lateral point load will be applied to both blocks in order to initiate buckling. This lateral load simulates the disturbance load as a 'trigger' that exists at quarries (e.g. aquifer pressure beneath quarry floor). Although the trigger mechanism used to induce buckling failure with this apparatus is purely artificial, and does not represent any real field condition, it is necessary to induce buckling in order to study the failure mechanism in the lab. An apparatus was built to provide these conditions at laboratory scale (Figure A.3). A particular challenge in the configuration of loading platens to give a realistic yet relatively easy to interpret loading condition.

To build this, an L shape steel plate ('L-plate') was used; the L shaped plate provides a horizontal base and vertical mounting surface. A pump attached to the
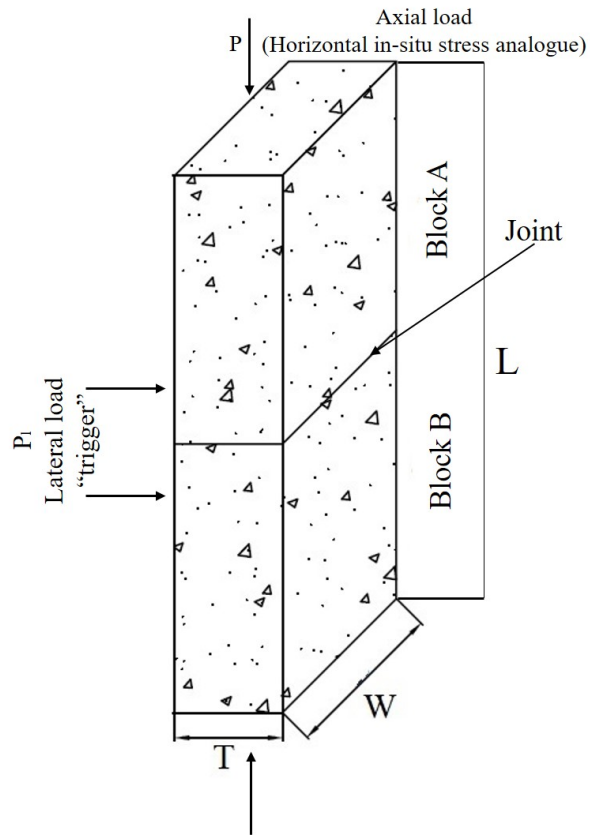
Figure A.2: Geometry of the blocks used for the simple THB buckling test.
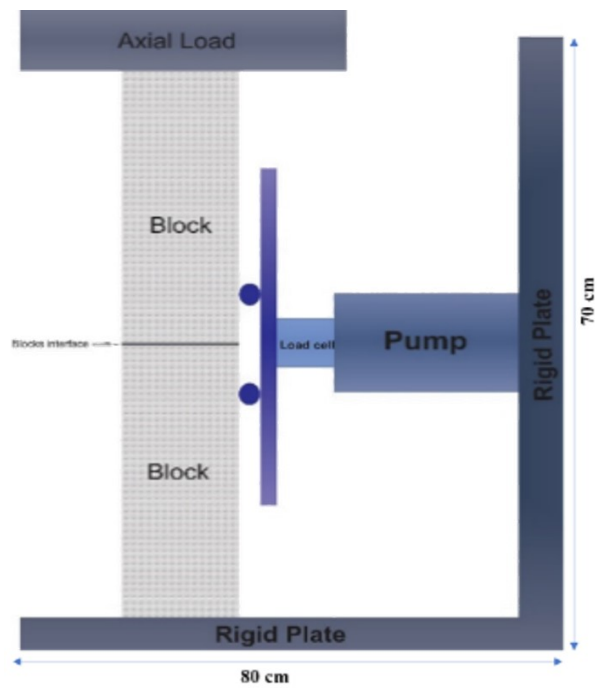

Figure A.3: The designed fixture used to implement the simple buckling failure.

vertical face of the L-plate, followed by a load cell to measure the lateral load. The load cell applied pressure to a loading plate through a hinge allowing motion in vertical axis. The loading plate applies equal point loading to each block via bars affixed to the loading plate. Two LVDTs were attached to the loading plate to measure the lateral displacement. Then, this apparatus was installed on an Instron load frame, which provides the vertical load for the experiment. Blocks were placed on a horizontal base of the L-plate, and two small fixed bars were placed in front of the blocks at top and bottom to prevent sliding of the blocks along the platens. A constant vertical load was applied to blocks after placing the samples through a spherical-seated upper platen and a flat plate lower platen. Then at desired set vertical pressure, steel shims were installed in the spherically-seated upper platen to make it a rigid platen for the buckling phase of the test. For the buckling phase, a lateral load was applied to the blocks. The lateral load was increased gradually until the buckling failure occurred.

One of the main features of this new apparatus is that everything is adjustable. Therefore, the THB tests can proceed with different conditions (e.g. rock block dimensions). Also, in next phase of our research program, we plan to replace the lateral load apparatus with an air bladder in order to directly simulate a constant pressure boundary to simulate field condition of pore pressure boundary.

A.4 Preliminary Tests

In order to preliminarily evaluate the test and apparatus, tests were conducted on concrete blocks. Specimen dimensions were 17 cm $\times$ 9 cm $\times$ 4 cm. They were

carefully prepared by grinding to achieve flat and level surfaces. The primary test was implemented on blocks with 10 and 15 MPa vertical pressure (Figure A.4). Figure A.5 shows that buckling failure occurs when the lateral load reaches to 16 kN, when the vertical load is 10 MPa, while the failure occurs at 15 kN lateral load when the vertical load is 15 MPa. The initial results show that increase in vertical load causes decreases in the maximum lateral load. Also, results show that the buckling failure occurred, when lateral displacement was about 12 mm when the vertical load was 15 MPa, while this amount was about 9 mm when the vertical load was 10 MPa. Therefore, with increase of vertical load the maximum lateral displacement (or 'Lateral displacement trigger') cause buckling, decreases.
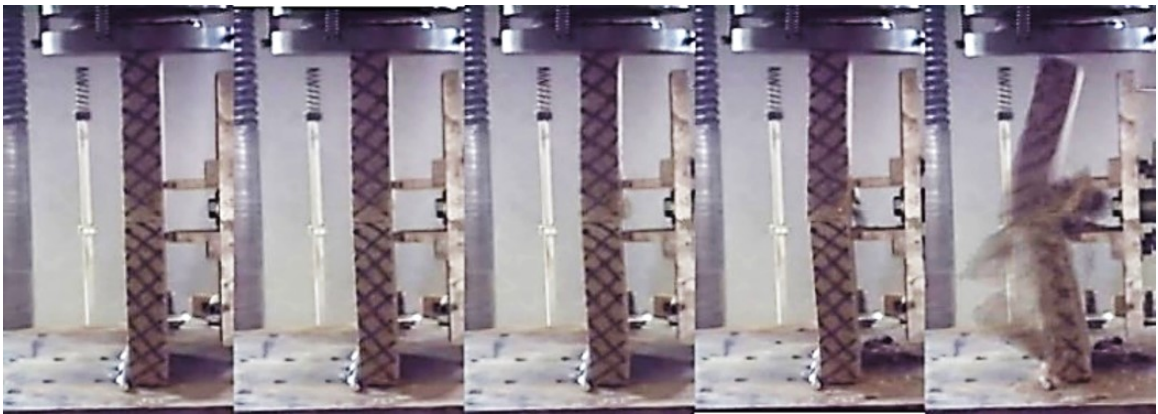

Figure A.4: Laboratory test of THB on concrete samples.

Figure A.6 shows that the test setup was consistent since we can see the vertical load is constant during increasing in lateral load.

Although the disturbance load type in fields and quarries are distributed, we have used equivalent lateral point load for initiating the buckling due to the simplicity of implementation. Therefore, 'equivalent lateral stress' was introduced to compare
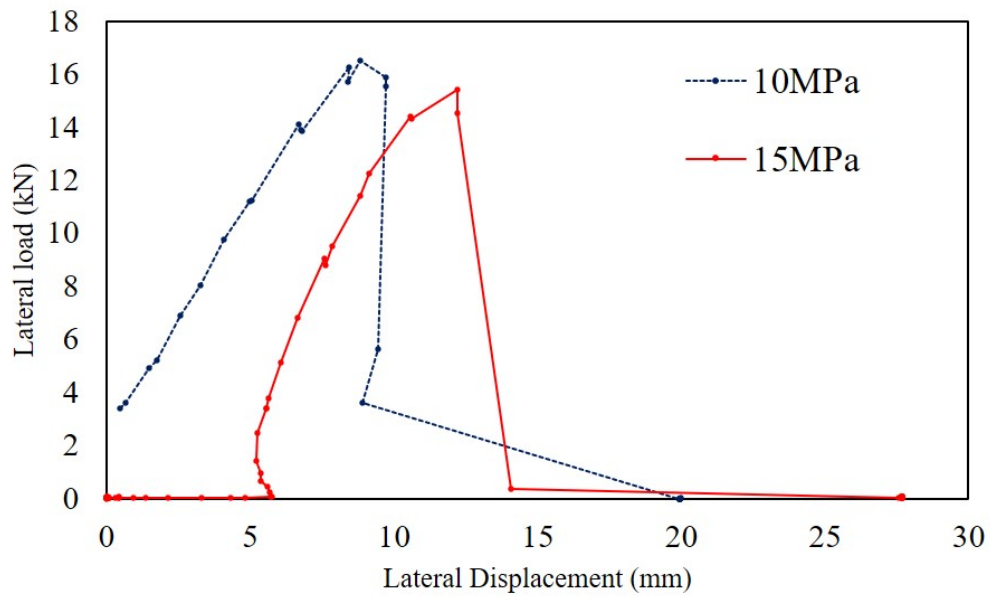
Figure A.5: Lateral load vs Lateral displacement for two values of confinement stresses.
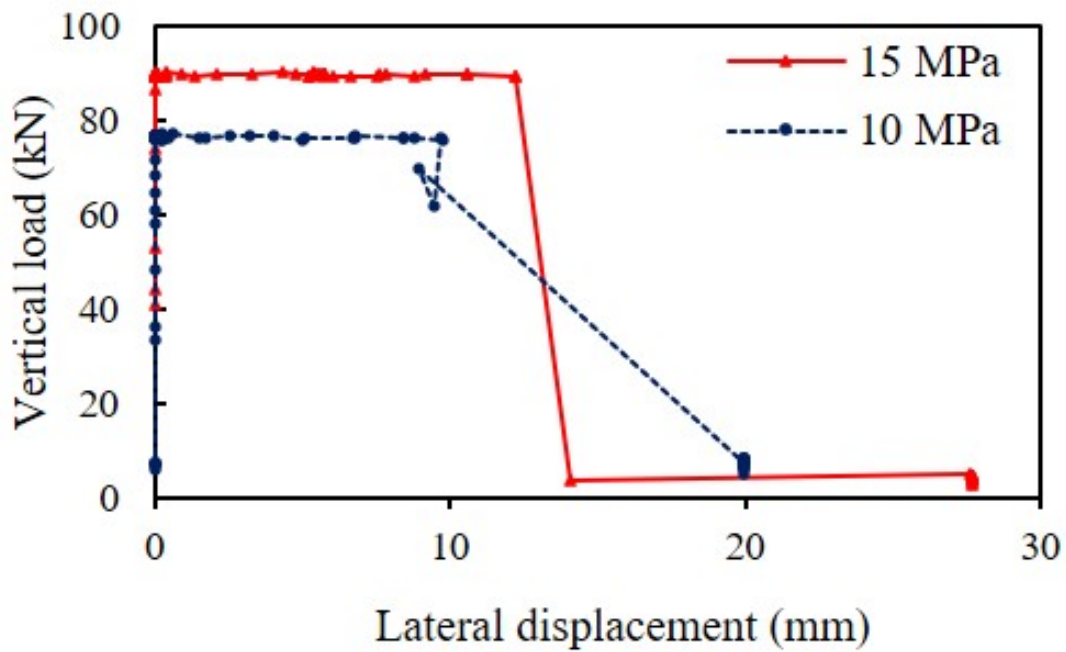

Figure A.6: Vertical load vs Lateral displacement.

this results with fields or numerical simulation results (Figure A.7). The equivalent lateral stress was calculated as the lateral point load divided by the sidelong areas of the two blocks. The apparatus was improved to increase its precision and stiffness of the device by adding shims to lock the spherical seating. The results of tests before and after improvement are compared in Figure A.8, and Figure A.9.
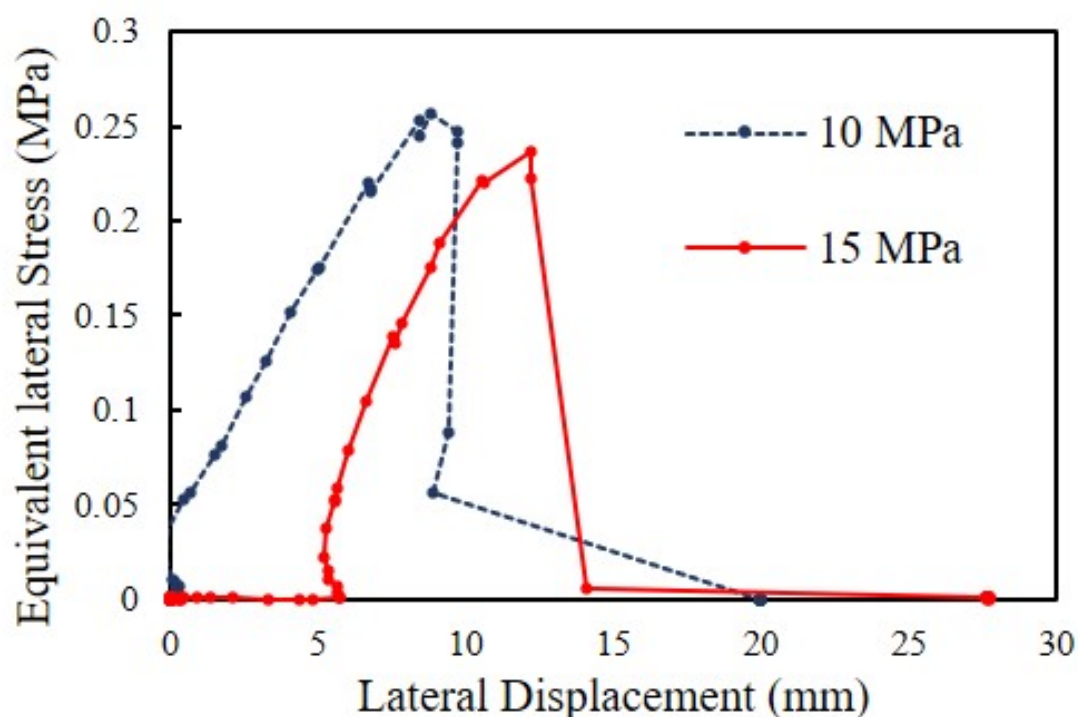

Figure A.7: Equivalent lateral stress vs Lateral displacement.

A.5 Preliminary Numerical Simulation

A preliminary numerical model was developed to gain insight into the mechanism. The ultimate goal of the program is to develop a calibrated model of the experiment. At this stage the model has not been suitably calibrated to the material used in the
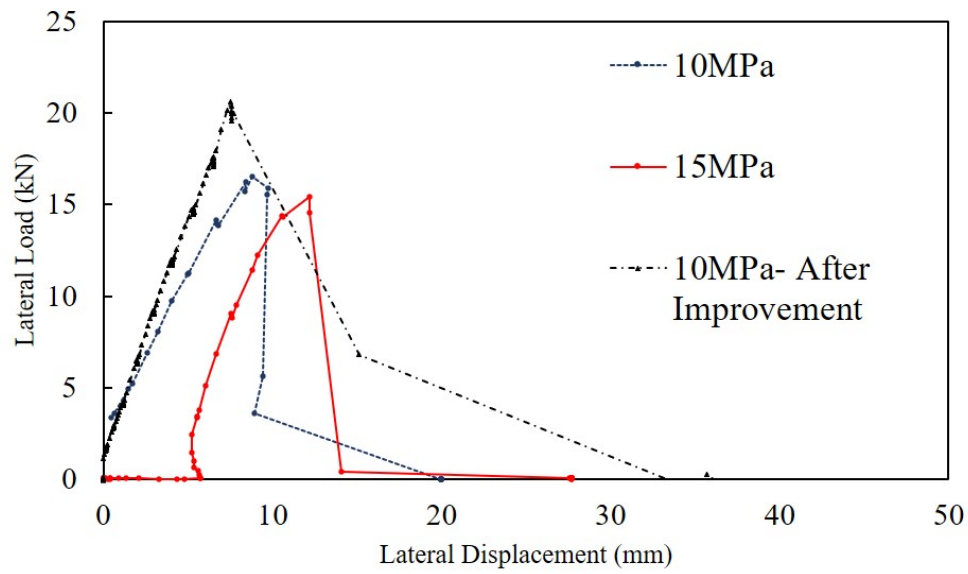
Figure A.8: Comparison between the experimental tests before and after improvement of the apparatus (Lateral load vs Lateral displacement).
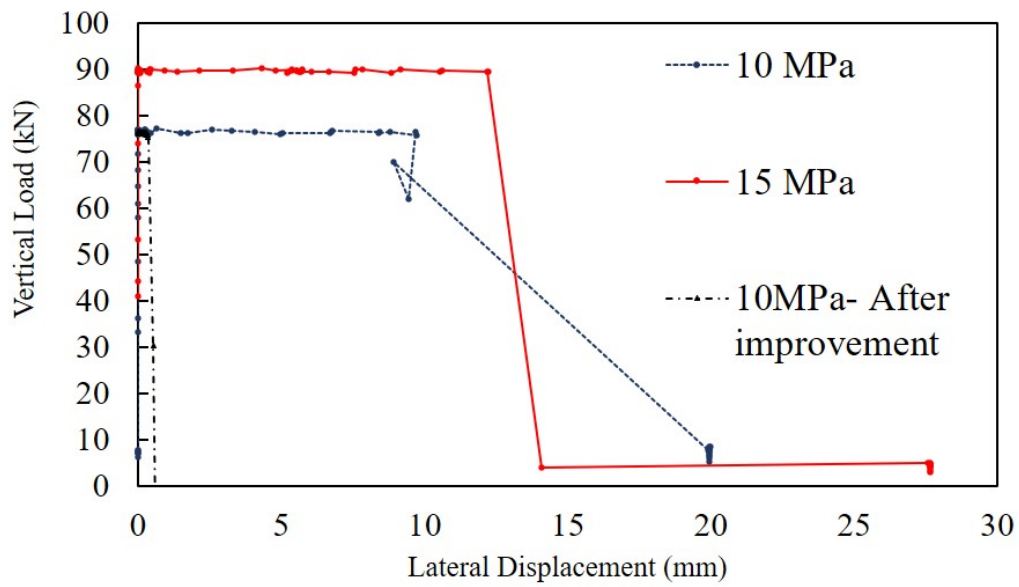

Figure A.9: Comparison between the experimental tests before and after improvement of the apparatus (Vertical load vs Lateral displacement).

preliminary experimental testing, but was used to provide insight into the failure mechanism of the experimental procedure. A calibrated model will be developed in future stages of the project.

To develop the numerical model, the two blocks were considered to be the same size and length to thickness ratio of experimental tests. Voronoi tessellation approach (Itasca, 2014) was used to simulate the micro-mechanical parameters of the blocks. Two rigid plates were considered at bottom and the top of blocks. These plates used to apply the vertical load to the blocks. Also, two small plates were included representing the bars that applied lateral point load.

At first stage, the boundary conditions were the same as the experimental model. Plates at the top and the bottom were fixed in the X direction. Also, the bottom plate was fixed in Y. Then, a constant vertical load was applied to the blocks. At the desired vertical load, two lateral point loads with constant displacement were applied to the blocks. These lateral loads represent the disturbance load required to initiate buckling (Figure A.10).

Conceptually, the results agreed with our preliminary experimental results since the buckling behavior was similar to our numerical model. The crushing zone in both the laboratory and the numerical tests were similar as shown in Figure A.11. Therefore, it shows that the experimental setup is well designed. However, stress and strain magnitudes from the uncalibrated model are not meaningful at this stage.
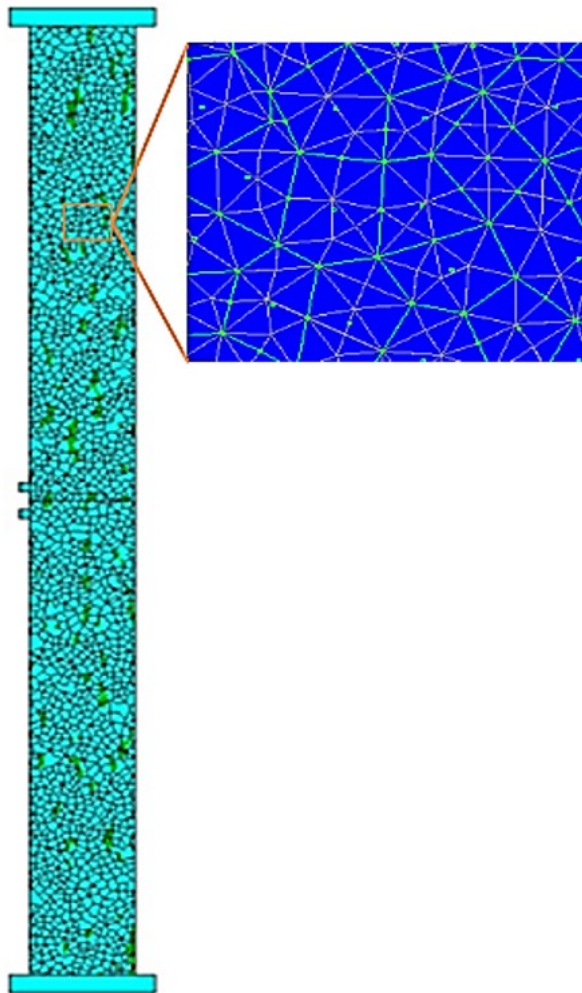
Figure A.10: Simulation of simple THB buckling failure (*UDEC* Voronoi tessellation).
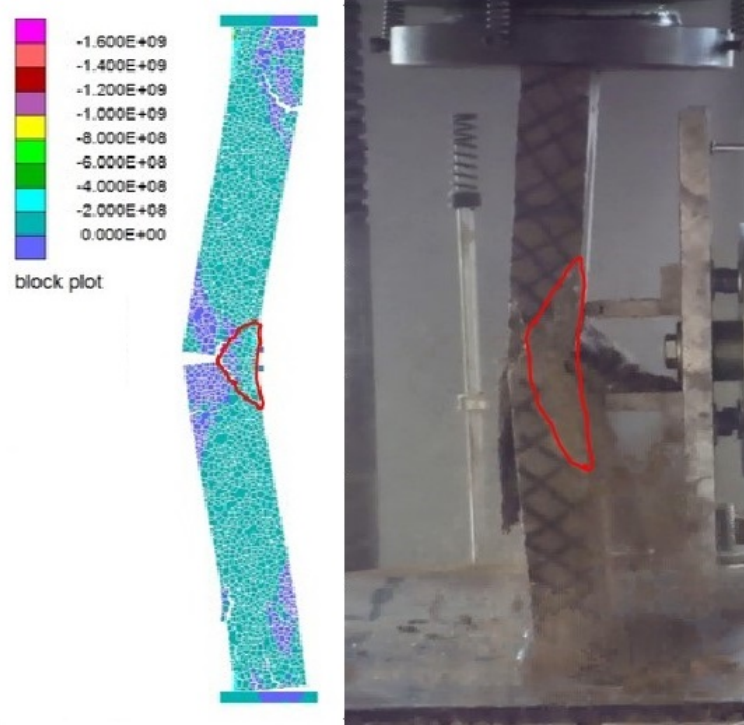
Figure A.11: Comparing the simulation and laboratory test result (*UDEC* Voronoi tessellation).

A.6   Conclusion

The THB failure mechanism is complex and requires more research gain suitable insight to support development a suitable analysis method for the failure mode. Development of a simple THB experimental laboratory test to observe the mechanism in controlled conditions has significant potential benefits. This study involved to development of an experimental test setup to capture simple THB behaviour at the laboratory scale. In addition to development of the test apparatus, the study also explored the use of the recently-developed Voronoi tessellation method in *UDEC* to capture the observed brittle fracture behaviour.

Preliminary results show that several factors have an impact on the THB mechanism, in particular, the impact of horizontal in situ stress, referred to as the clamping stress, which is represented by vertical stress in the test apparatus configuration. For instance, results show that, in the test apparatus, the maximum lateral load (or trigger load) changes with the application of different vertical loads. Future work will explore other factors such as geometry, rock type, stress condition, water pressure, and interaction of multiple blocks on THB failure.

Acknowledgement

Appendix B

Copyright Permissions

SPRINGER NATURE LICENSE
TERMS AND CONDITIONS

Dec 10, 2020

This Agreement between Mr. Mehdi Ghasemi Ghodrat ("You") and Springer Nature
("Springer Nature") consists of your license details and the terms and conditions provided by
Springer Nature and Copyright Clearance Center.

License Number	4965490556109
License date	Dec 10, 2020
Licensed Content Publisher	Springer Nature
Licensed Content Publication	Rock Mechanics and Rock Engineering
Licensed Content Title	A Three Hinge Buckling Laboratory Test
Licensed Content Author	M. Ghasemi et al
Licensed Content Date	May 28, 2020
Type of Use	Thesis/Dissertation
Requestor type	academic/university or research institute
Format	electronic

Portion	full article/chapter

Will you be translating?	no

Circulation/distribution	50000 or greater

Author of this Springer Nature content	yes

Title	Three Hinge Buckling Laboratory Experiment and Modelling Simulation

Institution name	Dalhousie University

Expected presentation date	Dec 2020

Requestor Location	Mr. Mehdi Ghasemi Ghodrat 1094 Wellington St 505 Halifax, NS B3H 2Z9 Canada Attn: Dalhousie University- Faculty of Graduate Studies

Total	0.00 CAD

Terms and Conditions

1. Grant of License

1. 1. The Licensor grants you a personal, non-exclusive, non-transferable, world-wide licence to reproduce the Licensed Material for the purpose specified in your order only. Licences are granted for the specific use requested in the order and for no other use, subject to the conditions below.

1. 2. The Licensor warrants that it has, to the best of its knowledge, the rights to license reuse of the Licensed Material. However, you should ensure that the material you are requesting is original to the Licensor and does not carry the copyright of another entity (as credited in the published version).

1. 3. If the credit line on any part of the material you have requested indicates that it was reprinted or adapted with permission from another source, then you should also seek permission from that source to reuse the material.

2. Scope of Licence

2. 1. You may only use the Licensed Content in the manner and to the extent permitted by these Ts&Cs and any applicable laws.

2. 2. A separate licence may be required for any additional use of the Licensed Material, e.g. where a licence has been purchased for print only use, separate permission must be obtained for electronic re-use. Similarly, a licence is only valid in the language selected and does not apply for editions in other languages unless additional translation rights have been granted separately in the licence. Any content owned by third parties are expressly excluded from the licence.

2. 3. Similarly, rights for additional components such as custom editions and derivatives require additional permission and may be subject to an additional fee. Please apply to Journalpermissions@springernature.com/bookpermissions@springernature.com for these rights.

2. 4. Where permission has been granted **free of charge** for material in print, permission may also be granted for any electronic version of that work, provided that the material is incidental to your work as a whole and that the electronic version is essentially equivalent to, or substitutes for, the print version.

2. 5. An alternative scope of licence may apply to signatories of the [STM Permissions Guidelines](#), as amended from time to time.

3. Duration of Licence

3. 1. A licence for is valid from the date of purchase ('Licence Date') at the end of the relevant period in the below table:

Scope of Licence	Duration of Licence
Post on a website	12 months
Presentations	12 months
Books and journals	Lifetime of the edition in the language purchased

4. Acknowledgement

4. 1. The Licensor's permission must be acknowledged next to the Licenced Material in print. In electronic form, this acknowledgement must be visible at the same time as the figures/tables/illustrations or abstract, and must be hyperlinked to the journal/book's homepage. Our required acknowledgement format is in the Appendix below.

5. Restrictions on use

5. 1. Use of the Licensed Material may be permitted for incidental promotional use and minor editing privileges e.g. minor adaptations of single figures, changes of format, colour and/or style where the adaptation is credited as set out in Appendix 1 below. Any other changes including but not limited to, cropping, adapting, omitting material that affect the meaning, intention or moral rights of the author are strictly prohibited.

5. 2. You must not use any Licensed Material as part of any design or trademark.

5. 3. Licensed Material may be used in Open Access Publications (OAP) before publication by Springer Nature, but any Licensed Material must be removed from OAP sites prior to final publication.

6. Ownership of Rights

6. 1. Licensed Material remains the property of either Licensor or the relevant third party and any rights not explicitly granted herein are expressly reserved.

7. Warranty

IN NO EVENT SHALL LICENSOR BE LIABLE TO YOU OR ANY OTHER PARTY OR

ANY OTHER PERSON OR FOR ANY SPECIAL, CONSEQUENTIAL, INCIDENTAL
OR INDIRECT DAMAGES, HOWEVER CAUSED, ARISING OUT OF OR IN
CONNECTION WITH THE DOWNLOADING, VIEWING OR USE OF THE
MATERIALS REGARDLESS OF THE FORM OF ACTION, WHETHER FOR BREACH
OF CONTRACT, BREACH OF WARRANTY, TORT, NEGLIGENCE, INFRINGEMENT
OR OTHERWISE (INCLUDING, WITHOUT LIMITATION, DAMAGES BASED ON
LOSS OF PROFITS, DATA, FILES, USE, BUSINESS OPPORTUNITY OR CLAIMS OF
THIRD PARTIES), AND
WHETHER OR NOT THE PARTY HAS BEEN ADVISED OF THE POSSIBILITY OF
SUCH DAMAGES. THIS LIMITATION SHALL APPLY NOTWITHSTANDING ANY
FAILURE OF ESSENTIAL PURPOSE OF ANY LIMITED REMEDY PROVIDED
HEREIN.

8. Limitations

8. 1. _BOOKS ONLY:_ Where **'reuse in a dissertation/thesis'** has been selected the
following terms apply: Print rights of the final author's accepted manuscript (for clarity,
NOT the published version) for up to 100 copies, electronic rights for use only on a
personal website or institutional repository as defined by the Sherpa guideline
(www.sherpa.ac.uk/romeo/).

9. Termination and Cancellation

9. 1. Licences will expire after the period shown in Clause 3 (above).

9. 2. Licensee reserves the right to terminate the Licence in the event that payment is not
received in full or if there has been a breach of this agreement by you.

Appendix 1 — Acknowledgements:

For Journal Content:
Reprinted by permission from [**the Licensor**]: [**Journal Publisher** (e.g.
Nature/Springer/Palgrave)] [**JOURNAL NAME**] [**REFERENCE CITATION**
(Article name, Author(s) Name), [**COPYRIGHT**] (year of publication)

For **Advance Online Publication papers:**
Reprinted by permission from [**the Licensor**]: [**Journal Publisher** (e.g.
Nature/Springer/Palgrave)] [**JOURNAL NAME**] [**REFERENCE CITATION**
(Article name, Author(s) Name), [**COPYRIGHT**] (year of publication), advance
online publication, day month year (doi: 10.1038/sj.[JOURNAL ACRONYM].)

For Adaptations/Translations:
Adapted/Translated by permission from [**the Licensor**]: [**Journal Publisher** (e.g.
Nature/Springer/Palgrave)] [**JOURNAL NAME**] [**REFERENCE CITATION**
(Article name, Author(s) Name), [**COPYRIGHT**] (year of publication)

**Note: For any republication from the British Journal of Cancer, the following
credit line style applies:**

Reprinted/adapted/translated by permission from [**the Licensor**]: on behalf of Cancer
Research UK: : [**Journal Publisher** (e.g. Nature/Springer/Palgrave)] [**JOURNAL
NAME**] [**REFERENCE CITATION** (Article name, Author(s) Name),
[**COPYRIGHT**] (year of publication)

For **Advance Online Publication** papers:
Reprinted by permission from The [**the Licensor**]: on behalf of Cancer Research UK:
[**Journal Publisher** (e.g. Nature/Springer/Palgrave)] [**JOURNAL NAME**]
[**REFERENCE CITATION** (Article name, Author(s) Name), [**COPYRIGHT**] (year
of publication), advance online publication, day month year (doi: 10.1038/sj.
[JOURNAL ACRONYM])

For Book content:
Reprinted/adapted by permission from [**the Licensor**]: [**Book Publisher** (e.g.
Palgrave Macmillan, Springer etc) [**Book Title**] by [**Book author**(s)]
[**COPYRIGHT**] (year of publication)

Other Conditions:

Version 1.2

**Questions? customercare@copyright.com or +1-855-239-3415 (toll free in the US) or
+1-978-646-2777.**